

*IN SITU* ATOMIC FORCE MICROSCOPY OF GROWING CRYSTALS  
REVEALS FUNDAMENTAL MECHANISMS OF CRYSTAL GROWTH AND  
INCORPORATION OF ADDITIVES

A Dissertation Presented to the Faculty

of Cornell University

In Partial Fulfillment of the Requirements for the Degree of

Doctor of Philosophy

By

Coit Taylor Hendley IV

August 2017

© 2017 Coit Taylor Hendley IV

*IN SITU* ATOMIC FORCE MICROSCOPY OF GROWING CRYSTALS  
REVEALS FUNDAMENTAL MECHANISMS OF CRYSTAL GROWTH AND  
INCORPORATION OF ADDITIVES

By Coit Taylor Hendley IV, Ph.D.

Cornell University, 2017

Calcite, the most thermodynamically stable form of calcium carbonate ( $\text{CaCO}_3$ ), is commonly found in nature and functions as a structural component for a variety of organisms including mollusks, sea urchins, and algae. In particular, the organisms often utilize single crystals that have significantly increased hardness, modulus, and toughness when compared to a geologic sample of calcite. The increased mechanical properties are of evolutionary benefit to the organism and arise due to additives which control the crystal formation and are incorporated within the single crystalline structures. These additives include magnesium substitutions, small molecules and amino acids, and nanometer scale globules of protein. Though the smaller scale additives are now relatively well understood, the interaction mechanisms between the nanoparticle scale organic and the crystal remain unknown. A more complete understanding of such particle-crystal interactions could lead to “design rules” which can optimize the incorporation of nanoparticles into single crystals. This work uses *in situ* AFM performed on growing calcite in the presence of nanoparticles with tunable surface chemistry and reveals three types of nanoparticle-crystal interactions: attachment-detachment, attachment-incorporation, and attachment-hovering, where the nanoparticle hovers on the surface as growth proceeds unaffected.

Additionally, the particle surface chemistry determines whether the interactions are driven by the charge corona on the particle (a particle driven regime) or by local behavior at the crystal surface (a surface driven regime). Further, this work demonstrates that the distribution of particles in an ensemble is divided between the three types of interactions in an equilibrium which can be affected by both surface chemistry and the growth conditions. Together, we now have a more complete picture of how nanoparticles can interact with a growing crystal surface.

## BIOGRAPHICAL SKETCH

Coit Taylor Hendley IV was born in 1990 to Coit T. Hendley III and Mary Hendley in Silver Spring Maryland. He was raised in Upper Marlboro Maryland and grew up with a love for the outdoors, sports, and learning. These pursuits inevitably lead to childhood dreams of digging up fossils or ancient cities.

Those dreams led to a love of science, and high school at the science and technology program at Eleanor Roosevelt in Greenbelt, MD, where his father taught AP chemistry and a research course about water quality and conservation. The senior year of the science and tech program required a research project with a small thesis-style paper and a poster presentation judged by local scientists.

After graduating in 2008, Coit entered the Bachelor's program in the Materials Science Department at the University of Maryland, College Park. He then received the SMART Scholarship from the Department of Defense, which led to an internship involving Energetics Development at the Naval Surface Warfare Center at Indian Head, Maryland. Following his graduation in 2012, he briefly worked for the Navy before going on leave in order to complete his doctoral work at Cornell University.

Once at Cornell he quickly joined Professor Lara Estroff's group after becoming inspired by their work striving to understand the beautiful complexity found in biominerals. After completing his defense he will return to work for the Navy at Indian Head, Maryland in their Research Department which specializes in the synthesis, analysis, and detection of Energetic materials.

## ACKNOWLEDGEMENTS

My success in this graduation program would have been impossible without the many who have helped support me, knowingly or not. My time at Cornell has been wonderful and I wouldn't change anything.

First thanks go to my advisor, Professor Lara Estroff. Without her remarkable passion for research I would be a lesser student and person than I am today. She has been the best mentor and advisor I could have asked for throughout.

Next, all of the members of the Estroff group during my time at Cornell who were always willing to help provide advice or support whenever it was needed. We made ourselves better together. Also thanks to my undergrads Rachel Connelly and Jeremy Gershonowitz who helped in my work and helped me learn how to teach.

Without my collaborators Dr. Lee Fielding and Dr. Lizzy Jones with the Armes group, it would not have been possible to complete this work. They were always responsive and thorough in any requests for samples or information.

My practical education about AFM and crystal growth began during my stay with the group of Dr. James DeYoreo at DOE where I first learned how to grow crystals in a microscope. In particular I want to thank Dr. Paul Smeets who helped train me. Also thanks to Dr. Yi-Yeoun Kim and all the members of the Meldrum group for their help with calcite growth.

Many thanks to the Wiesner group and in particular Dr. Kwan Tan, who helped me get the fluid AFM system up and running. Also thanks to the facility managers at CCMR for their expertise and advice.

Thank you to Dr. Darrell Schlom and Dr. Lena Kourkoutis for serving on my committee and helping me become a better scientist through their teaching and advice.

Finally, nothing I have accomplished would have been possible without the love and support of my parents and family.

## TABLE OF CONTENTS

Abstract.....	v
Biographical Sketch.....	vi
Acknowledgements.....	vii
List of Figures.....	xvi
List of Abbreviations.....	xxxiii
<b>PREFACE</b> .....	xxxiv
References.....	xxxvii
<b>CHAPTER 1: MICROSCOPY TECHNIQUES FOR INVESTIGATING THE CONTROL OF ORGANIC CONSTITUENTS ON BIOMINERALIZATION....</b>	<b>1</b>
1.1 Introduction.....	1
1.2 Visualizing matrix assembly and mineral formation.....	4
<i>1.2.1 What mechanisms and energetic factors control nucleation and     growth?</i> .....	4
<i>1.2.2 In situ Atomic Force Microscopy (AFM): Real-time imaging of     assembly processes on surfaces</i> .....	4
<i>1.2.3 Cryogenic Electron Microscopy (cryoEM) and tomography: High-     resolution, three-dimensional (3D) imaging of hydrated samples</i> .....	10

1.2.4 <i>In situ Transmission Electron Microscopy (TEM): direct observation of nucleation in bulk solutions and within organic matrices</i> .....	12
1.3 Macromolecular inclusions in biominerals and bioinspired materials.....	16
1.3.1 <i>How are large additives incorporated into crystalline lattices?</i> .....	16
1.3.2 <i>Electron Tomography: 3D structural information</i> .....	17
1.3.3 <i>Atom Probe Tomography (APT): Spatially-resolved chemical information at the nanoscale</i> .....	19
1.3.4 <i>X-ray spectroscopy: Mapping amorphous to crystalline transformations</i> .....	22
1.3.5 <i>Vibrational spectromicroscopy: Chemically rich 3D maps of tissue composition</i> .....	23
1.4 Conclusions.....	24
References.....	27
<b>CHAPTER 2: MECHANISITC INSIGHTS INTO NANOPARTICLE- CRYSTAL INTERACTIONS REVEALED VIA <i>IN SITU</i> ATOMIC FORCE MICROSCOPY (AFM)</b> .....	36
2.1 Abstract.....	36
2.2 Introduction.....	37
2.3 Results.....	41
2.3.1 <i>Experimental design</i> .....	41

2.3.2 Nanoparticle Characterization.....	43
2.3.3 Calcite Growth <i>ex situ</i> .....	45
2.3.4 <i>In situ</i> AFM.....	47
2.3.5 Nanoparticle-crystal interactions.....	51
2.4 Discussion.....	54
2.4.1 Charge corona effect on particles in solution.....	55
2.4.2 A model for nanoparticles interacting with a growing crystal.....	56
2.4.3 Initial binding process: importance of the charge corona.....	59
2.4.4 Particles binding later hover: effect of free polymer in solution.....	62
2.5 Conclusions.....	63
2.6 Materials and Methods.....	64
2.6.1 Particle synthesis.....	64
2.6.2 Dynamic light scattering and zeta potential.....	64
2.6.3 Transmission Electron Microscopy (TEM).....	64
2.6.4 <i>Ex situ</i> “bulk” calcite growth.....	65
2.6.5 <i>In situ</i> AFM experiments.....	65
2.6.6 AFM image analysis.....	66
2.7 Acknowledgements.....	67

2.8 Supporting Information.....	67
2.8.1 <i>Tip effects</i> .....	67
References.....	76
<b>CHAPTER 3: TUNING PARTICLE-SUBSTRATE INTERACTIONS WITH SOLUTION CHEMISTRY.....</b>	<b>80</b>
3.1 Abstract.....	80
3.2 Introduction.....	81
3.2.1 <i>Polyelectrolyte nanoparticles in solution</i> .....	83
3.3 Results and Discussion.....	86
3.3.1 <i>Nanoparticle structuring in solution</i> .....	86
3.3.2 <i>Divalent cations increase surface interactions</i> .....	87
3.3.3 <i>Polyelectrolyte particle-surface interactions depend on particle structure</i> .....	91
3.3.4 <i>Background electrolyte reveals a second interaction regime</i> .....	93
3.3.5 <i>Non-polyelectrolyte-surface interactions depend on hydration layer structure</i> .....	96
3.3.6 <i>Particle binding permanency</i> .....	98
3.4 Conclusions.....	102
3.5 Materials and Methods.....	103

3.5.1 Nanoparticle Synthesis.....	103
3.5.2 Dynamic light scattering and zeta potential.....	103
3.5.3 In situ AFM of calcite growth.....	104
3.5.4 AFM image analysis.....	104
3.6 Acknowledgements.....	105
3.7 Supplementary.....	106
References.....	111
<b>CHAPTER 4: A SURVERY OF HILLOCK-HILLOCK INTERACTIONS USING <i>IN SITU</i> ATOMIC FORCE MICROSCOPY (AFM): FRAMEWORK FOR LINKING NANOSCALE TO MACROSCALE GROWTH.....</b>	<b>114</b>
4.1 Introduction.....	114
4.2 Results and Discussion: Categorizing Hillock-Hillock Interactions.....	119
4.2.1 Burgers vector length (“Single” or “Double” Hillock) and Step Annihilation.....	119
4.2.2 Relative Height.....	121
4.2.3 Step edge curvature and Hillock Spacing.....	123
4.2.4 Additives and Multiple Hillocks.....	125
4.2.5 Open Questions.....	128
4.3 Conclusions.....	129
4.4 Methods.....	130

4.4.1 <i>In situ AFM</i> .....	130
4.4.2 <i>Image Processing and Analysis</i> .....	130
References.....	132
<b>CHAPTER 5: CONCLUSIONS</b> .....	<b>136</b>

## LIST OF FIGURES

**Figure 1.1**.....7

*In situ* AFM can be used to investigate matrix self-assembly and mineralization.

(A)–(F) Self-assembly of Type I collagen on mica into an ordered array with periodicity of 67 nm found in natural collagen. Times (min) are: (A) 12.9, (B) 25.8, (C) 43.0, (D) 55.9, (E) 60.2, and (F) 77.4. (G)–(I) Architecture of collagen on mica at pH 4.0 for  $K^+$  concentrations (mMol) of (G) 100 (H) 200 (I) 300. (J)–(L) Nucleation of calcium phosphate on collagen at a solute concentration above the ACP solubility limit. (J) ACP at 24 min then transforms to octacalcium phosphate at 64 min (K) and then HA at 98 min (L). Time 0 corresponds to the moment solution was injected into the atomic force microscopy fluid cell. Insets show transmission electron microscopy images collected on samples taken from the three stages of development. (M) Dependence of nucleation rate on time at six different supersaturations  $\sigma_i$ . Details of the supersaturation values can be found in Reference 12. Analysis of the data gives interfacial energies  $\alpha_i$  of  $\alpha_{ACP} = 40 \text{ mJ} \cdot \text{m}^{-2}$  and  $\alpha_{HA} = 90 \text{ mJ} \cdot \text{m}^{-2}$ . (N) Relationship between growth rate and particle height on surface of collagen with  $\sigma_{HA} = 3.31$ ,  $\sigma_{OCP} = 1.71$ ,  $\sigma_{ACP} = -0.02$ . A critical size of 0.7 nm is determined from the zero crossing of the average growth rate (dashed line) All scale bars are 200 nm except in (I) where it is 500 nm in the main image only. (A-F) adapted and reprinted from Ref. 9 with permission from Elsevier copyright 2006. (G-L) reprinted with permission from Macmillan Publishers Ltd Ref. 12 copyright 2013.

**Figure 1.2**.....11

(A, B) Cryogenic electron microscopy yields insights into the mineralization of hydrated samples. (A) CryoTEM of a collagen fibril (from horse tendon) with amorphous calcium phosphate (ACP) particles collecting near the hole regions of the collagen (white arrows) after mineralization for 24 hrs in buffered  $\text{CaCl}_2$ ,  $\text{KPO}_4$ , and 10  $\mu\text{g/mL}$  of pAsp. (B) Tomographic reconstruction of the fibril after the apatite has been fully crystallized (72 hrs in buffered solution) reveals platelets (colored red) of mineral within the fibril itself. (C)–(E) Electron microscopy and tomography reveal details of incorporated macromolecular additives. (C) ADF-scanning transmission electron microscopy (STEM) of a focused ion beam section of a calcite crystal (scanning electron microscopy, inset) grown in a 1 w/v% agarose gel. Despite well-developed rhombohedral crystal, agarose gel fibers are clearly visible (darker contrast) randomly distributed within the thin section. (D) Selected-area electron diffraction of the area imaged in (C) demonstrating that the gel-grown crystal diffracts electrons as a single crystal. (E) ADF-STEM tomographic reconstruction of an area similar to (C) which emphasizes the network of agarose fibers incorporated within the crystal. (A and B) Adapted and reprinted by permission from Macmillan Publishers Ltd: Ref. 34 copyright 2010. (C and D) adapted from Ref. 63 with permission from AAAS copyright 2009.

**Figure 1.3**.....14

*In situ* liquid phase transmission electron microscopy (TEM) enables observation of nucleation and phase evolution for both mineral and organic components. Schematic of (A) TEM liquid cell holder and (B) liquid cell. (C) Globules (gray) formed through  $\text{Ca}^{2+}$  counter-ion condensation on polystyrene sulfonate (PSS), some containing newly formed amorphous calcium carbonate (ACC) particles (black). (D) Zeta potential showing shift to more positive values due to  $\text{Ca}^{2+}$  binding to PSS to form globules (red—pure  $\text{CaCl}_2$  solution, blue— $\text{CaCl}_2$  solution containing PSS). (E) Growth rates of vaterite particles (orange, green, blue) formed in the absence of PSS and ACC particles (black and red) within Ca-PSS globules. (F) Time series showing ACC nucleation and growth within a globule. In absence of PSS, vaterite forms randomly (not shown). Scale bars: (C) 50 nm, (F) 20 nm. Adapted and reprinted (C-F) by permission from reference 43 Macmillan Publishers Ltd: copyright 2015. Also adapted and reprinted (A and B) from reference 42 with permission from AAAS copyright 2014.

**Figure 1.4**.....21

(A) Schematic of an atom probe tomography experiment in which the sample is ablated by a laser (forming ions) onto a mass spectrometer to determine the type of atoms within the removed section. (B) Tomographic reconstruction of an elephant dentin sample shows the isosurface for the organic fragment number density (blue surface is the threshold for dense organic) revealing fibers aligned along the  $z$  axis. (C) and (D) Selected sections from the reconstruction in (B) with

mass density for organic fragments (C) and Na<sup>+</sup> (D) locations shown. The highest density regions for each are often, but not exclusively, the same, which implies that something in the organic macromolecules may bind the ions. Scale for (C) and (D) are the same as (B) *x-y* plane. Adapted and reprinted with permission from Ref. 70, copyright 2012.

**Scheme 2.1**.....43

Summary of the three types of diblock copolymer nanoparticles used in this study.

(A) Non-ionic poly(glycerol monomethacrylate)-stabilized poly(benzyl methacrylate) nanoparticles (Ph-PGMA<sub>63</sub>-PBzMA<sub>100</sub>); (B) Poly(glycerol monomethacrylate)-stabilized poly(benzyl methacrylate) nanoparticles with a single carboxylic acid group located at the end of each PGMA stabilizer chain (HOOC-PGMA<sub>71</sub>-PBzMA<sub>100</sub>); (C) Anionic poly(methacrylic acid)-stabilized poly(benzyl methacrylate) nanoparticles (PMAA<sub>85</sub>-PBzMA<sub>100</sub>).

**Figure 2.1**.....41

Zeta potential (red) and DLS diameter (blue) measurements versus pH for both PMAA-PBzMA (filled circles) and HOOC-PGMA-PBzMA (open squares) nanoparticles. Measurements were conducted in the presence of 1 mM KCl and titrated from basic to acidic pH using HCl.

**Figure 2.1**.....43

Representative scanning electron microscopy (SEM) images of calcite grown ex situ at 20 °C with the three types of nanoparticles used in this study (see main text

for further details). (A) Control calcite crystal prepared in the absence of any nanoparticles. (B) Representative crystals grown in the presence of non-ionic Ph-PGMA-PBzMA nanoparticles. (C) Representative crystal grown in the presence of anionic HOOC-PGMA-PBzMA nanoparticles. (D) Representative crystal grown in the presence of PMAA-PBzMA nanoparticles. In each case the ammonia diffusion method was utilized at pH 8 using 5 mM CaCl<sub>2</sub> and a copolymer nanoparticle concentration of 0.75 wt%.

**Figure 2.2**.....45

Representative scanning electron microscopy (SEM) images of calcite grown ex situ at 20 °C with the three types of nanoparticles used in this study (see main text for further details). (A) Control calcite crystal prepared in the absence of any nanoparticles. (B) Representative crystals grown in the presence of non-ionic Ph-PGMA-PBzMA nanoparticles. (C) Representative crystal grown in the presence of anionic HOOC-PGMA-PBzMA nanoparticles. (D) Representative crystal grown in the presence of PMAA-PBzMA nanoparticles. In each case the ammonia diffusion method was utilized at pH 8 using 5 mM CaCl<sub>2</sub> and a copolymer nanoparticle concentration of 0.75 wt%.

**Figure 2.3**.....48

Time-resolved in situ AFM studies of calcite growth in the presence of three types of sterically-stabilized diblock copolymer nanoparticles ( $\sigma = 1.15$ , nanoparticle concentration = .00075% wt). Zero time ( $t = 0$ ) refers to when the nanoparticle-containing growth solution is first added to the AFM cell. A-C: growth in the

presence of non-ionic Ph-PGMA-PBzMA nanoparticles. D-F: growth in the presence of weakly anionic HOOC-PGMA-PBzMA nanoparticles. G-I: growth in the presence of strongly anionic PMAA-PBzMA nanoparticles. The (+) and (-) define the obtuse and acute facets of the growing calcite hillock, respectively. Movies S1-S3 available online depict a more complete series of images. Images are deflection (color scale  $\pm 20$  mV) taken in contact mode.

**Figure 2.4**.....51

High resolution in situ AFM images of the highly anionic PMAA-PBzMA nanoparticles interacting with a growing calcite face at  $\sigma = 1.15$ . The height measurements in the bottom right are from line scan measurements of the highlighted nanoparticles. Over time, three types of behavior can be observed, although the highlighted nanoparticles start at similar relative height. The orange nanoparticle attaches between the first and second image, then detaches between the third and fourth image. There is a gradual reduction in the height of the green nanoparticle until it is apparently incorporated within the crystal. The blue nanoparticle “hovers” on the surface, staying attached but not becoming incorporated within the crystal. This Figure is also available as Movie S4.

**Figure 2.5**.....54

Comparison of the three modes of interaction of HOOC-PGMA-PBzMA and PMAA-PBzMA nanoparticles with calcite as determined by in situ AFM studies. (A) Histograms showing the relative proportion of each nanoparticle population to exhibit either detachment, hovering or incorporation. (n=50 for PMAA-PBzMA

and n=27 for HOOC-PGMA) (B) Histograms showing the number of nanoparticles each of the three types of behavior for PMAA-PBzMA nanoparticles over time. The image number refers to the last image obtained before a significant (>10%) height reduction is observed. A comparable histogram obtained for HOOC-PGMA-PBzMA nanoparticles is shown in Fig. S7 (albeit for fewer nanoparticles). See Methods section for further details on image analysis and nanoparticle selection.

**Scheme 2.2**.....58

Schematic representation of the possible modes of interaction of two types of anionic nanoparticles interacting with a growing calcite surface. On contact with the surface, the nanoparticles first undergo fast diffusion to become bound at a step edge. Subsequent relaxation of the copolymer chains determines to what extent the growth species ( $\text{Ca}^{2+}$  and  $\text{CO}_3^{2-}$  ions) can access binding sites on the step edge. Hence the nanoparticle either (I) detaches or (II) continues to interact with the surface by “hovering”. For the highly anionic PMAA-PBzMA nanoparticles, the copolymer chains can either (IIB) remain rigid (slow relaxation) to allow access of growth ions to the step edge or (IIA) relax quickly, thus blocking growth species. For the HOOC-PGMA stabilizer chains, faster relaxation (II) blocks growth ions from diffusing to the step edge. When such mass transport is blocked, the pinned nanoparticle becomes occluded as the step grows around it.

**Figure 2.6(S1)**.....69

Tapping mode AFM images, line scans and transmission electron micrographs (TEM) of (A, C) PMAA-PBzMA and (B, D) HOOC-PGMA-PBzMA nanoparticles. AFM images of the nanoparticles absorbed onto poly(lysine)-treated mica were obtained in deionized water. TEM images were obtained by drying a dilute dispersion of nanoparticles onto a carbon-coated TEM grid before staining with uranyl formate. According to TEM (17.1 nm average) and AFM studies (15.2 nm average), the PMAA-PBzMA (A, C) and HOOC-PGMA-PBzMA (B, D) nanoparticles are very similar in size (~12 nm).

**Figure 2.7(S2)**.....70

A typical *in situ* AFM image used to track nanoparticle interactions (PMAA-PBzMA) with the surface of a calcite crystal. Yellow circles highlight the nanoparticles which meet the requirements for further tracking and analysis. Nanoparticles indicated by pink circles do not qualify for tracking because they have already begun to be incorporated. Each nanoparticle indicated by a yellow circle has had its height tracked and recorded and is included in the larger data set.

**Figure 2.8(S3)**.....71

Time series of *in situ* AFM images during calcite step growth in the presence of uncharged Ph-PGMA-PBzMA nanoparticles. Inset (A) shows a control hillock before addition of these nanoparticles. The steps clearly move unhindered with no nanoparticle attachment despite their presence in solution near the crystal surface (as indicated by the greater noise and streaking in images).

**Figure 2.9(S4)**.....72

Relative nanoparticle height over time for a single *in situ* AFM image series of HOOC-PGMA-PBzMA nanoparticles on the surface of a calcite crystal. Each line corresponds to an individual nanoparticle tracked across multiple AFM images. Three types of nanoparticle behavior were observed; (i) immediate detachment from the surface within one image (orange lines, n = 17), (ii) hovering on the surface before either detachment or incorporation (blue lines, n = 6), and (iii) incorporation directly into the crystal (green lines, n = 27). The distribution of hovering nanoparticles between later detachment and incorporation is likely to be strongly affected by the AFM tip and is therefore not studied in further detail. Nanoparticles that are directly incorporated into the calcite appear to do so at similar rates.

**Figure 2.10(S5)**.....73

Relative nanoparticle height over time for the PMAA-PBzMA nanoparticles. Each line corresponds to an individual nanoparticle tracked across multiple AFM images. The color coding by behavior type is the same to that in Figure S4: orange represents nanoparticle detachment (n = 7), blue represents nanoparticle hovering (n = 17), and green corresponds to immediate nanoparticle incorporation into the crystal (n = 26). Incorporation appears to occur at similar rates for all nanoparticles.

**Figure 2.11(S6)**.....74

*In situ* AFM images showing the effect of the AFM tip on PMAA-PBzMA nanoparticles on the surface of calcite. Similar observations were also made for HOOC-PGMA-PBzMA nanoparticles (not shown). The lower magnification image obtained at 186 seconds reveals the region where the sample was imaged. There are clearly some tip artifacts, but these will be identical for all samples analyzed and the most likely effect is to remove some of the “hovering” nanoparticles, thus preventing further binding and incorporation.

**Figure 2.12(S7)**.....75

Histogram showing the number of nanoparticles that either detach, hover or incorporate for HOOC-PGMA-PBzMA nanoparticles over time. The image number refers to the last image obtained before a significant (> 10%) height reduction is observed. Note the similarity to the histogram shown in Figure 5B of the main manuscript.

**Scheme 3.1**.....84

Experimental Design. We use two different types of polymeric nanoparticles to evaluate the importance of solution conditions like supersaturation and ionic strength. Here we show a control growth hillock on calcite (A) from which we subsequently choose a growth condition and nanoparticle (B). Then we observe the effects on the hillock and track the nanoparticles over time as growth proceeds (C).

**Figure 3.1**.....86

Z-average diameter and zeta potential measurements as a function of calcium chloride concentration for both nanoparticle types used in this study. pH = 8 set using KOH, CaCl<sub>2</sub> diluted from 1 M stock solution (CaCl<sub>2</sub>·2H<sub>2</sub>O, Sigma Aldrich).

**Figure 3.2**.....87

Representative AFM images (at t~10 min after adding nanoparticles) from experiments spanning supersaturation. Qualitatively supersaturation has a major impact on the particle-crystal interaction. An increase in supersaturation brought by increasing [Ca<sup>2+</sup>] and [CO<sub>3</sub><sup>2-</sup>] in solution greatly enhances the attachment of both types of particles to the surface. In particular, for the PMAA-PBzMA particles, a film of particles forms on the surface at the highest sigma. Particle concentration is 0.00075% wt.  $\sigma=0.76$  corresponds to 1.4 mM CaCl<sub>2</sub> and  $\sigma=1.54$  is [CaCl<sub>2</sub>] =2.2 mM. The [NaCl] is adjusted to keep the ionic strength (IS) constant at 35 mM.

**Figure 3.3**.....90

Area coverage measured by ImageJ at three different supersaturations, and constant IS=35. Both particle types increase in coverage with increasing supersaturation. From  $\sigma=1.15$  to  $\sigma=1.54$  the PMAA attachment increases significantly and disproportionately. Data are the mean of measurements across five images from t~10 to t~15 min after particle injection. Error bars are one standard deviation above and below the mean

**Figure 3.4**.....91

Structural changes in the charge corona of a polyelectrolyte nanoparticle with pH and cation concentration such as the PMAA-PBzMA nanoparticles used in this study. Chains are extended by osmotic pressure and coulombic repulsion at the pH of calcite growth (pH 8) but are collapsed if there is sufficient concentration of cations to satisfy the negative charges on the chains.

**Figure 3.5**.....93

Representative AFM images (at t~10 min) after introduction of 0.00075 % wt particles. Effect of varying ionic strength by changing [NaCl] in the growth solution. The increase in the number of HOOC-PGMA-PBzMA particles (yellow arrows, top right) which attach to the crystal surface is notable. The PMAA particles appear to attach readily at both ionic strengths (yellow arrows, bottom).  $\sigma=1.15$  corresponds to  $[Ca^{2+}] = 1.8$  mM. The ionic strength is varied by changing [NaCl].

**Figure 3.6**.....95

Area coverage measured by ImageJ at three different ionic strengths, and constant  $\sigma=1.15$ . There is no apparent change for the PMAA-PBzMA nanoparticles while no binding increases to ~1% coverage for HOOC-PGMA-PBzMA nanoparticles. Data are the mean of measurements across five images from t~10 to t~15 min after particle injection. Error bars are one standard deviation above and below the mean.

**Figure 3.7**.....96

The interaction between HOOC-PGMA-PBzMA particles and calcite is determined by the local crystal surface environment. Calcite structure is adapted from Margraff, Reeder, 1985 (AMSCD).

**Figure 3.8**.....98

Growth and recovery of a hillock as PMAA-PBzMA nanoparticles round the hillock and form a bound film (t=0 min to t=47 min) and then are gradually removed via incorporation near the hillock peak once a control growth solution is added (t=47 min to t=63 min). Growth at  $\sigma=1.54$  (2.2 mM  $\text{Ca}^{2+}$ ) and .00075% wt nanoparticles.

**Figure 3.9**.....100

A film is formed on the crystal surface after the particles are added (t=0). Subsequently, growth apparently proceeds along the hillock peak and ridges while particles are present (t=36 min) and accelerates under control growth conditions (t=36 min to t=60 min). The original hillock recovers, maintaining its rhombohedral morphology in a hopper-like region (t=76 min to t=95 min). Growth proceeds rapidly upon hillock recovery (t=60 min to t=95 min). The 3D images at bottom visualize the apparently rapid vertical growth upon hillock recovery from 60 to 95 min. Growth at  $\sigma=1.54$  (2.2 mM  $\text{Ca}^{2+}$ ) and .00075% wt nanoparticles.

**Figure 3.10**.....102

When on a terrace or bound to a step edge, the polymer nanoparticle locally blocks growth unit access, preventing growth. However, in an area of locally high curvature such as a peak or ridge, the stabilizer chains are more permeable and growth units can access the kink sites.

**Figure 3.11(S1)**.....106

Diameter and zeta potential of PMAA-PBzMA nanoparticles with increasing [NaCl] measured at pH 8 (set using KOH). There is a limited effect on the PMAA-PBzMA diameter. NaCl was diluted from 1 M stock solution (NaCl 100% ACS Reagent, JT Baker).

**Figure 3.12(S2)**.....107

A time series for PMAA-PBzMA particles at the highest supersaturation ( $\sigma=1.54$ ). The particles attach densely and eventually form a film on the surface.

**Figure 3.13(S3)**.....107

The polymer film formed at high supersaturation ( $\sigma=1.54$ ) by the PMAA-PBzMA particles is unaffected by the tip. At lower supersaturations the tip.

**Figure 3.14(S4)**.....108

Visualization of particle analysis procedure. See Methods for details. A deflection image is set to 20mV scale, then the image is thresholded to ensure only particles are selected. Finally the thresholded area is measured.

**Figure 3.15(S5)**.....108

Ex situ growth with PMAA-PBzMA particles at initial calcium concentrations of: (A) 1 mM, (B) 2 mM, (C) 5 mM, (D) 10 mM and control growth without particles at (E) 1 mM, (F) 5 mM, (G) 10 mM. The crystals grown at higher  $\sigma$  and with the nanoparticles appear to have fewer single crystals and more polycrystals and non-calcite polymorphs of  $\text{CaCO}_3$  (XRD Fig. S7). The particle concentration is 0.75 % wt.

**Figure 3.16(S6)**.....109

XRD patterns corresponding to samples of Figure S6. We observe an increase in polycrystals of calcite and vaterite at higher  $\sigma$  and when polyelectrolyte nanoparticles are present. *Ex situ* growth was performed using the ammonium diffusion method with  $[\text{CaCl}_2]$  as listed in Figure S4 and particle concentration 0.75% wt.

**Figure 3.17(S7)**.....110

(A inset) control calcite growth at 5 mM  $[\text{Ca}^{2+}]$ . (A-C) calcite growth with increasing  $[\text{Na}^+]$  of (A) 5 mM, (B) 100 mM, (C) 500 mM. (D-F) calcite growth in the presence of 0.75% wt of HOOC-PGMA-PBzMA nanoparticles at  $[\text{Na}^+]$  of (D) 5mM, (E) 100 mM and (F) 500 mM. Increased rounding and roughening of single crystal edges and facets in the presence of nanoparticles indicates increased interaction, as predicted by the *in situ* experiments.

**Figure 4.1**.....116

Generation of a new step edge from a dislocation source once the edge length  $L$  exceeds the critical length  $L_c$  required for propagation (A and B). The rhombohedral symmetry of calcite results in anisotropy on terraces and two distinct step edges (C and D). From “Teng H.H., Dove P.M., Orme C.A., De Yoreo J.J., “Thermodynamics of Calcite Growth: Baseline for Understanding Biomineral Formation,” *Science*, 1998, 282, 5389.” Reprinted with permission from AAAS.

**Figure 4.2**.....118

The empirical connection between individual nanoscale growth hillocks and bulk crystal morphology. (A) A control growth calcite crystal and hillock with no additive present. (B) Calcite grown in the presence of  $Mg^{2+}$ . SEM reprinted with permission from Han and Aizenberg.<sup>38</sup> (C) Calcite growth with the amino acid D-Aspartic acid. Reprinted with permission from Orme et. al.<sup>13</sup> (D) Calcite growth with the protein AP8 extracted from the nacreous layer of the mollusk abalone. Reprinted with permission from Fu et. al.<sup>39</sup> Figure reprinted with permission from “De Yoreo J.J., Dove P.M., Shaping Crystals with Biomolecules, *Science*, 2004, 306, 5700, 1302-1302.”<sup>17</sup>

**Figure 4.3**.....119

A “double” hillock generating two unit high edges intersects the steps from a “single” Burgers vector source. The double high steps (blue lines) neatly

annihilate two single high steps each (blue circle), as expected from classical theory. Growth at  $\sigma=1.15$ ,  $[Ca^{2+}] = 1.8$  mM.

**Figure 4.4**.....121

Images and corresponding relative height over time for two different hillock pairs. A and B exhibit a surprising instability after ~25 min, where one hillock suddenly accelerates in growth relative to the other, beginning an overgrowth process. C and D demonstrate the expected classical behavior of the two hillocks growing in parallel over time. C and D were imaged over a shorter time, so could enter the unstable growth state later. Growth at  $\sigma=1.15$ ,  $[Ca^{2+}] = 1.8$  mM.

**Figure 4.5**.....124

Curvature varies depending on the type of steps interacting and apparently on the hillock offset/separation. A: two hillocks nearly perfectly aligned have very little curvature between their step edges. B: A larger offset between the hillock peaks leads to different step edges interacting. Even when an acute and obtuse edge directly intersect (red), a single sharp corner remains, indicating a single kink site. C: It appears that only the acute-acute interactions (blue) generate kink sites and have a reduced curvature. Non acute-acute interactions (red) retain high curvature and a limited number of kink sites. Growth at  $\sigma=1.15$ ,  $[Ca^{2+}] = 1.8$  mM.

**Figure 4.6**.....127

Two calcite growth experiments illustrating unusual growth behavior with Glycine. (A, B) Two modified hillocks overlap one another. In B, a small remnant of the overlapped hillock appears to protrude from the larger hillock (red arrow).

(C, D) Hillocks appear to nucleate mid-growth (blue), revealing additional complexity. The horizontal lines in C and D are 10s of nm scale surface defects.

Growth at  $\sigma=1.15$ ,  $[\text{Ca}^{2+}] = 1.8 \text{ mM}$ ,  $[\text{Gly}] = 1.8 \text{ mM}$ .

## LIST OF ABBREVIATIONS

ACC	Amorphous Calcium Carbonate
ACP	Amorphous Calcium Phosphate
AFM	Atomic Force Microscopy
APT	Atom Probe Tomography
Asp	Aspartic Acid
CaCO <sub>3</sub>	Calcium Carbonate
CaCl <sub>2</sub>	Calcium Chloride
Cryo-EM	Cryogenic Electron Microscopy
DI water	Deionized water
EM	Electron Microscopy
Gly	Glycine
HA	Hydroxyapatite
NaCl	Sodium Chloride
SEM	Scanning Electron Microscopy
TEM	Transmission Electron Microscopy
XRD	X Ray Diffraction

## PREFACE

Naturally formed biominerals are stronger and harder than their geologic equivalents. The evolutionary advantage provided by the improved mechanical properties comes from precise control of the crystal growth that results in the finished mineral. Organisms achieve such control by using large quantities of additives including substituted atoms, small molecules (amino acids), larger polymeric organics (like peptides), and proteins.<sup>1,2</sup> The additives also become incorporated within the crystal and inhibit dislocation motion, leading to the mechanical improvements in the bulk crystal.<sup>3-5</sup> Together, additives help to shape and structure the crystals to the organism's needs. For example, in the mollusk *Atrina Rigida* Calcium Carbonate is structured in two layers, one with prisms of single crystalline Calcite (the most stable polymorph) and the other with tablets of Aragonite (the least stable polymorph), both with hardness which is up to 3000x greater than their geologic equivalents.<sup>3,4,6</sup> Such powerful control of crystallization is highly desirable for a huge variety of fields, from materials for clean energy to synthesis of new pharmaceuticals. To fully take advantage of crystallization controls requires in depth understanding of the mechanisms which determine the additive-crystal interactions. At the bulk crystal scale, it is relatively straightforward to grow crystals with additives of interest and examine their morphology to see how the growth is affected. There is a significant body of literature describing such studies for calcite with molecular scale additives.<sup>4,7-10</sup> In particular, Wegner and coworkers were the first to demonstrate synthetic incorporation of nanoparticles into an inorganic single crystal.<sup>11,12</sup> They controlled

the surface chemistry of latex nanoparticles to facilitate incorporation into both zinc oxide and calcite. In the calcite case, a thicker corona with a high density of negatively charged acid groups best facilitated incorporation. Then the Meldrum and Armes groups began designing polymer based nanoparticles to more closely mimic the calcite single crystals observed in nature.<sup>9</sup> It became clear that simply a dense network of negatively charged groups is insufficient to facilitate incorporation and in fact, fully acidic stabilizer chains are required.<sup>13-15</sup> Such ex situ studies have provided a structure for “design rules” to guide synthesis for facilitating incorporation. To fully understand how the additives interact with a growing crystal, however, requires nanoscale studies of growing crystal surfaces in which we directly observe the interaction. Here too there is a body of literature on atomic and molecular scale additives utilized in situ Atomic Force Microscopy (AFM). Orme and De Yoreo first demonstrated the effects of amino acids on growing calcite and proposed an energetic explanation for the observed modification on growth hillocks.<sup>10</sup> Subsequently, in situ studies of additive-crystal interactions have been performed on crystal systems such as calcium oxalate, l-cysteine, zeolites, and hematin.<sup>16-23</sup> Detailed studies of molecular scale additives have only recently been completed however, and as such even larger scale organics have only begun to be studied. Cho and coworkers recently observed the direct incorporation of micellar polymeric micelles into a calcite single crystal.<sup>24</sup> They propose a size dependent incorporation mechanism where a cavity is formed in the crystal to accommodate the nanoparticle and the size of the cavity scales with the size of the nanoparticle. This thesis builds on their work and uses in situ

AFM to probe the ensemble behavior of particle population as their surface chemistry varies. There are two regimes of interaction depending on the stabilizer chains of the nanoparticle. If the particle is stabilized by long, acidic, negatively charged polymer chains the particle can access polyelectrolyte behavior. Polyelectrolyte particles swell with increasing pH and are collapsed by cations in solution. Such behavior makes their interaction with the crystal highly dependent on the chain conformation, and their interactions are particle driven. Once on the surface, they can access a “hovering” behavior when the stabilizer chains are extended, and they remain bound to the surface as growth proceeds underneath the particle. If a nanoparticle’s stabilizer chains are not polyelectrolytes, the particle-surface interaction is surface driven, and more sensitive to conditions in solution. Further, classic studies of additive-crystal interactions focus on single growth hillocks, where the progression from the morphology of a single growth hillock is relatively easily compared to the morphology of a bulk grown calcite crystal. However, for a more macroscale growing crystal, it is highly likely there will be multiple hillocks on the surface, and the interactions between hillocks leading to the final morphology is no longer trivial. This work has characterized a variety of hillock-hillock interactions and presents a framework for evaluating hillock-hillock pairs which lead to the development of the macroscale crystal morphology. In situ AFM has proven to be an extremely valuable tool for studying crystal growth, and this work helps complete the library of work focused on additive-crystal interactions as well as understanding the link from nanoscale to macroscale.

## REFERENCES

- (1) Lowenstam, H. .; Weiner, S. *On Biomineralization*; Oxford University Press Inc., 1989.
- (2) Addadi, L.; Weiner, S. *Phys. Scr.* 2014, 89 (9), 98003.
- (3) Kunitake, M. E.; Mangano, L. M.; Peloquin, J. M.; Baker, S. P.; Estroff, L. A. *Acta Biomater.* 2013, 9 (2), 5353.
- (4) Kim, Y.-Y.; Carloni, J. D.; Demarchi, B.; Sparks, D.; Reid, D. G.; Kunitake, M. E.; Tang, C. C.; Duer, M. J.; Freeman, C. L.; Pokroy, B.; Penkman, K.; Harding, J. H.; Estroff, L. A.; Baker, S. P.; Meldrum, F. C. *Nat. Mater.* 2016, 15 (8), 903.
- (5) Ma, Y.; Aichmayer, B.; Paris, O.; Fratzl, P.; Meibom, A.; Metzler, R. A.; Politi, Y.; Addadi, L.; Gilbert, P. U. P. A.; Weiner, S. *Proc. Natl. Acad. Sci. U. S. A.* 2009, 106 (15), 6048.
- (6) Li, H.; Xin, H. L.; Kunitake, M. E.; Keene, E. C.; Muller, D. A.; Estroff, L. A. *Adv. Funct. Mater.* 2011, 21 (11), 2028.
- (7) Muñoz-Espí, R.; Qi, Y.; Lieberwirth, I.; Gómez, C. M.; Wegner, G. *Chem. - A Eur. J.* 2006, 12 (1), 118.
- (8) Wegner, G.; Demir, M. M.; Faatz, M.; Gorna, K.; Munoz-Espi, R.; Guillemet, B.; Gröhn, F. *Macromol. Res.* 2007, 15 (2), 95.
- (9) Kim, Y.-Y.; Ganesan, K.; Yang, P.; Kulak, A. N.; Borukhin, S.; Pechook, S.; Ribeiro, L.; Kröger, R.; Eichhorn, S. J.; Armes, S. P.; Pokroy, B.; Meldrum, F. C. *Nat. Mater.* 2011, 10 (11), 890.

- (10) Orme, C. A.; Noy, A.; Wierzbicki, A.; McBride, M. T.; Grantham, M.; Teng, H. H.; Dove, P. M.; DeYoreo, J. J. *Nature* 2001, 411 (6839), 775.
- (11) Muñoz-Espí, R.; Qi, Y.; Lieberwirth, I.; Gómez, C. M.; Wegner, G.; Muñoz-espí, R.; Qi, Y.; Lieberwirth, I.; Gómez, C. M.; Wegner, G.; Muñoz-Espí, R.; Qi, Y.; Lieberwirth, I.; Gómez, C. M.; Wegner, G. *Chem. - A Eur. J.* 2006, 12 (1), 118.
- (12) Rafael Muñoz-Espí; Amreesh Chandra; Wegner, G.; *Crystal Growth and Design*, 2007, 7,9, 1584.
- (13) Ning, Y.; Fielding, L. A.; Doncom, K. E. B.; Penfold, N. J. W.; Kulak, A. N.; Matsuoka, H.; Armes, S. P. *ACS Macro Lett.* 2016, 5 (3), 311.
- (14) Ning, Y.; Fielding, L. A.; Andrews, T. S.; Growney, D. J.; Armes, S. P.; *Nanoscale* 2015, 7 (15), 6691.
- (15) Kim, Y.-Y.; Semsarilar, M.; Carloni, J. D.; Cho, K. R.; Kulak, A. N.; Polishchuk, I.; Hendley, C. T.; Smeets, P. J. M.; Fielding, L. A.; Pokroy, B.; Tang, C. C.; Estroff, L. A.; Baker, S. P.; Armes, S. P.; Meldrum, F. C. *Adv. Funct. Mater.* 2016, 26 (9), 1382.
- (16) Wesson, J. A.; Ward, M. D. *Elements* 2007, 3 (6).
- (17) Rimer, J. D.; An, Z.; Zhu, Z.; Lee, M. H.; Goldfarb, D. S.; Wesson, J. A.; Ward, M. D. *Science* 2010, 330 (6002), 337.
- (18) Poloni, L. N.; Ward, M. D. *Chem. Mater.* 2014, 26 (1), 477.
- (19) Lupulescu, A. I.; Rimer, J. D. *Science* 2014, 344 (6185), 729.
- (20) Olafson, K. N.; Ketchum, M. A.; Rimer, J. D.; Vekilov, P. G. *Proc. Natl. Acad. Sci. U. S. A.* 2015, 112 (16), 1501023112.

- (21) Qiu, S. R.; Wierzbicki, A.; Orme, C. A.; Cody, A. M.; Hoyer, J. R.; Nancollas, G. H.; Zepeda, S.; De Yoreo, J. J. *Proc. Natl. Acad. Sci. U. S. A.* 2004, 101 (7), 1811.
- (22) Weaver, M. L.; Qiu, S. R.; Friddle, R. W.; Casey, W. H.; De Yoreo, J. J. *Cryst. Growth Des.* 2010, 10 (7), 2954.
- (23) Qiu, S. R.; Orme, C. A. 2008, No. Figure 1, 4784.
- (24) Cho, K.R.; Kim, Y.-Y.; Yang, P.; Cai, W.; Pan, H.; Kulak, A. N.; Lau, J. L.; Kulshreshtha, P.; Armes, S. P.; Meldrum, F. C.; De Yoreo, J. J. *Nat. Commun.* 2016, 7, 10187.

## CHAPTER 1

# MICROSCOPY TECHNIQUES FOR INVESTIGATING THE CONTROL OF ORGANIC CONSTITUENTS ON BIOMINERALIZATION\*

### *1.1 Introduction*

One of the universal characteristics of biomineralizing systems is that macromolecular constituents, such as proteins and polysaccharides, are found in close association with the mineral constituents.<sup>1,2</sup> Some of these organic components are water soluble, but others assemble to create an insoluble scaffold within which the minerals form. This intimate relationship between the matrix and mineral, along with the unusual morphologies of biominerals and the common occurrence of metastable mineral phases, suggests that the organic matrix actively controls mineral nucleation and growth. Moreover, significant quantities of the organic matrix are typically occluded within the resulting hierarchically-structured tissues (discussed further in this issue by Schenk and Kim).<sup>3</sup> This composite architecture endows biominerals with remarkable mechanical properties and, as a result, during the past few decades, biomineral systems have inspired developments in materials synthesis of new composite materials.<sup>4,5</sup> However, truly emulating biological processes for novel

---

\* Reproduced with permission from Hendley IV, C.T., Tao J., Kunitake J.A.M.R., DeYoreo J.J., Estroff L.A., "Microscopy techniques for investigating the control of organic constituents on biomineralization", MRS Bulletin, 2015, 40, 6, 480-489, Cambridge Publishing Inc.

material creation has yet to be fully realized, because both the mechanisms by which the macromolecular matrix assembles and mineralizes and the principles underlying the structure-function relationships of mineralized tissues are poorly understood. Recent advances in the application of microscopy techniques to define both the processes of matrix assembly and mineralization and the hierarchical distribution of matrix and mineral are beginning to fill the gaps in our understanding of both formation and properties. Here we review some of these advances, using examples from biological as well as bio-inspired systems to illustrate the insights they have enabled. **Table 1.1** provides a summary of the microscopy techniques discussed, including their benefits and limitations within the scope of analyzing biominerals and bio-inspired systems.

**Table 1.1** Summary of techniques used to characterize biomineralization and bioinspired synthesis presented in this chapter with a brief review of their advantages/disadvantages.

Table I. Summary of discussed techniques.			
Technique	Benefits	Limitations	References
AFM (atomic force microscopy)	<ul style="list-style-type: none"> <li>• Direct visualization of nuclei formation and growth</li> <li>• Direct visualization of incorporation processes</li> <li>• Atomic-scale resolution possible</li> </ul>	<ul style="list-style-type: none"> <li>Specialized setup and difficult experiments</li> <li>Limited range of supersaturations</li> <li>Comparison to bulk studies</li> </ul>	<ul style="list-style-type: none"> <li>Reviews: 7, 8, 21</li> <li>Key studies: 6, 9–18, 20</li> </ul>
Cryo-EM (cryogenic electron microscopy)	<ul style="list-style-type: none"> <li>• Maintains hydrated environment during imaging</li> <li>• “Snapshots” of dynamic processes</li> <li>• Can be combined with tomography for 3D imaging</li> </ul>	<ul style="list-style-type: none"> <li>Specialized sample preparation</li> <li>Limited sample size</li> <li>Beam sensitivity</li> </ul>	<ul style="list-style-type: none"> <li>Reviews: 26</li> <li>Key studies: 27–35</li> </ul>
Liquid cell transmission electron microscopy	<ul style="list-style-type: none"> <li>• Real-time visualization of nucleation and growth in liquid environment</li> <li>• Possibility to simultaneously image organic and inorganic material</li> </ul>	<ul style="list-style-type: none"> <li>Emerging technology</li> <li>Very small reaction volumes</li> <li>Mixing/trigger of nucleation</li> <li>Beam artifacts</li> </ul>	<ul style="list-style-type: none"> <li>Reviews: 37, 38, 40</li> <li>Key studies: 36, 39, 41–45</li> </ul>
Electron tomography	<ul style="list-style-type: none"> <li>• Direct visualization of organics within inorganic crystals</li> <li>• Crystallography</li> <li>• 3D images</li> </ul>	<ul style="list-style-type: none"> <li>Electron transparent sample</li> <li>Beam damage</li> <li>Difficult analysis of 3D data sets</li> <li>High vacuum</li> </ul>	<ul style="list-style-type: none"> <li>Reviews: 49, 55, 56</li> <li>Key studies: 59–63</li> </ul>
Atom probe tomography	<ul style="list-style-type: none"> <li>• Spatially resolved chemical information</li> <li>• 3D images</li> </ul>	<ul style="list-style-type: none"> <li>Specialized sample preparation and data analysis</li> </ul>	<ul style="list-style-type: none"> <li>Reviews: 65–68</li> <li>Key studies: 69–71</li> </ul>
X-ray spectromicroscopy	<ul style="list-style-type: none"> <li>• Crystalline and amorphous material</li> <li>• Some chemical mapping ability</li> <li>• Bulk samples</li> </ul>	<ul style="list-style-type: none"> <li>Requires synchrotron source</li> <li>Variable sensitivity to surface preparation</li> </ul>	<ul style="list-style-type: none"> <li>Reviews: 31, 72, 78</li> <li>Key studies: 74, 76, 77, 79, 81–84</li> </ul>
Vibrational spectromicroscopy	<ul style="list-style-type: none"> <li>• Chemically rich information about organic and inorganic components</li> <li>• Confocal capabilities</li> <li>• Correlation with other techniques</li> <li>• Hydrated samples (only for Raman)</li> </ul>	<ul style="list-style-type: none"> <li>Auto-fluorescence of some tissues</li> <li>Resolution limited to 1 <math>\mu\text{m}</math></li> <li>For infrared, thin, transparent samples</li> </ul>	<ul style="list-style-type: none"> <li>Reviews: 85, 86</li> <li>Key studies: 88–95</li> </ul>

## 1.2 Visualizing matrix assembly and mineral formation

### 1.2.1 What mechanisms and energetic factors control nucleation and growth?

In recent years, investigations of both matrix assembly and mineralization have been performed to better understand the *in vivo* mechanisms that control these processes. *In situ* methods have been particularly important, because dynamic behavior occurs in response to differences in energy states and the barriers that separate those states; thus, such studies provide an opportunity to probe the energy landscape across which matrix assembly and mineralization take place. For both processes, the important length scales are from the molecular scale to tens of nanometers. Consequently, atomic force microscopy (AFM) and transmission electron microscopy (TEM) have been the most significant techniques used, though the information gained is typically augmented with other types of data, both *in situ* and *ex situ*.

### 1.2.2 *In situ AFM: Real-time imaging of assembly processes on surfaces*

AFM is a type of scanning probe microscopy that uses a sharp tip on the end of a cantilever to sense changes in sample topography. When the tip is brought to within the range of the interatomic potential between the tip and surface, variations in the potential with position lead to vertical deflections of the cantilever. Thus the topography of the surface can be mapped by measuring the deflection of cantilever as the tip is raster-scanned over surface. Typically, this deflection is measured by reflecting a laser from the top of the cantilever onto a photodiode array, giving a vertical resolution of less than an Angstrom.

AFM can be applied to both organic matrices and mineral surfaces exposed to fluid, which is either static or flowing.<sup>6-8</sup> Consequently, it enables direct observations

of matrix assembly on substrates,<sup>9-11</sup> mineral nucleation on organic matrices,<sup>12, 13</sup> and post-nucleation growth and interaction with organic constituents.<sup>7, 14-18</sup> These measurements can be complemented by a number of other techniques to obtain a comprehensive picture of chemical interactions, energetic drivers, and mechanisms of formation. The first, cryogenic electron microscopy (cryoEM), is a form of transmission electron microscopy (TEM) in which a sample of solution is frozen so rapidly in liquid N<sub>2</sub> or liquid ethane that it forms a thin layer of vitrified water. Cryo-EM enables the observation of specimens in their native environment without any staining or fixation, thus providing high-resolution structural information. The second, *in situ* dynamic force spectroscopy (DFS) is a special application of AFM that records the force required to break the bond between a functionalized AFM tip and a surface. When this rupture force is measured as a function of the bond extension rate, the resulting relationship provides characteristic parameters of the intermolecular and mineral-matrix bonds such as the binding free energy per molecule. Vibrational and electronic spectroscopy can be used to reveal the functional groups responsible for the observed changes in free energies and barriers, and molecular simulations can be employed to test proposed mechanisms and determine underlying structural reasons for the dominant interactions.

AFM has been used to investigate assembly of protein matrices by introducing aqueous solutions of protein into a sample chamber referred to as a fluid cell, which contains substrates that promote assembly.<sup>9, 10</sup> *In vivo*, collagen molecules, which form the organic matrix of bone, align and intertwine to form microfibrils containing “hole zones,” where there are gaps between the N- and C-termini of successive collagen

molecules.<sup>19</sup> Observations of collagen assembly on mica revealed formation of ordered fibrils via two distinct steps that resulted in the same periodicity observed in collagen fibrils formed *in vivo* (**Figure 1.1A–F**).<sup>9</sup> First, three single strand collagen molecules associate with one another to form 1.5 nm-high triple-helices called topocollagen molecules. These then assembled into ordered, 3 nm-high microfibrils, which formed the building blocks of the larger scale fibrils. Other studies recorded development of alternative architectures that depended strongly on the choice of pH and salt concentration (Figure 1.1G–I). For example, while the ordered structure seen in Figure 1.1A–F is obtained at pH 9.0 for K<sup>+</sup> concentrations of 200 mM and above, at pH 4.0 the architecture evolves from a monolayer of randomly oriented molecules to a monolayer of co-aligned molecules to 3D bundles of co-aligned molecules as the K<sup>+</sup> concentration is increased from 100 to 300 mM.<sup>11</sup> Comparing the *in situ* results with coarse-grained molecular models of assembly provided insights into the energetic underpinnings of collagen architecture.<sup>11</sup> Predictions based on variations of the relative strengths of the inter-collagen and collagen-substrate binding through a periodic set of strong and weak inter-collagen binding sites gave the observed evolution in collagen architecture.

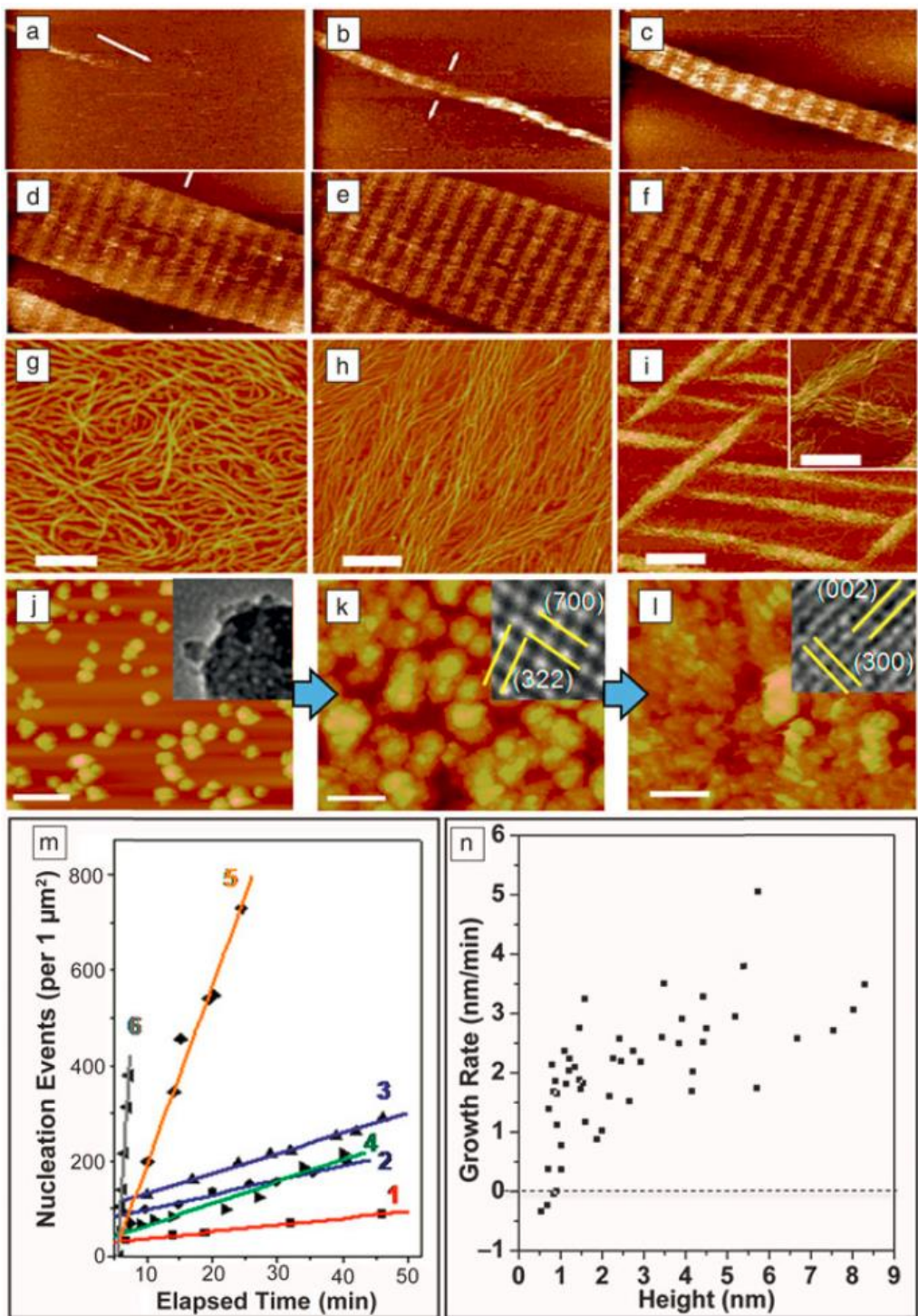


**Figure 1.1** *In situ* AFM can be used to investigate matrix self-assembly and mineralization. (A)–(F) Self-assembly of Type I collagen on mica into an ordered array with periodicity of 67 nm found in natural collagen. Times (min) are: (A) 12.9, (B) 25.8, (C) 43.0, (D) 55.9, (E) 60.2, and (F) 77.4. (G)–(I) Architecture of collagen on mica at pH 4.0 for  $K^+$  concentrations (mMol) of (G) 100 (H) 200 (I) 300. (J)–(L) Nucleation of calcium phosphate on collagen at a solute concentration above the ACP solubility limit. (J) ACP at 24 min then transforms to octacalcium phosphate at 64 min (K) and then HA at 98 min (L). Time 0 corresponds to the moment solution was injected into the atomic force microscopy fluid cell. Insets show transmission electron microscopy images collected on samples taken from the three stages of development. (M) Dependence of nucleation rate on time at six different supersaturations  $\sigma_i$ . Details of the supersaturation values can be found in Reference 12. Analysis of the data gives interfacial energies  $\alpha_i$  of  $\alpha_{ACP} = 40 \text{ mJ} \cdot \text{m}^{-2}$  and  $\alpha_{HA} = 90 \text{ mJ} \cdot \text{m}^{-2}$ . (N) Relationship between growth rate and particle height on surface of collagen with  $\sigma_{HA} = 3.31$ ,  $\sigma_{OCP} = 1.71$ ,  $\sigma_{ACP} = -0.02$ . A critical size of 0.7 nm is determined from the zero crossing of the average growth rate (dashed line) All scale bars are 200 nm except in (I) where it is 500 nm in the main image only. (A-F) adapted and reprinted from Ref. 9 with permission from Elsevier copyright 2006. (G-L) reprinted with permission from Macmillan Publishers Ltd Ref. 12 copyright 2013.

Mineral nucleation on organic matrices can also be visualized by AFM.<sup>12, 13</sup> Organic matrices are first assembled on flat substrates. Aqueous solutions of the mineral phase are then passed through the fluid cell and formation of mineral nuclei is observed (Figure 1.1J–L). If the nucleation process is arrested by switching from flow of reagents to a liquid in which the mineral has no solubility, such as alcohol, the sample can be collected and analyzed by TEM or Raman spectroscopy to determine the mineral phase at a single point in time.<sup>12</sup> The use of DFS to measure the binding energy of the protein to single crystal substrates of the mineral allows one to correlate the interfacial energy with matrix-mineral binding free energy.<sup>13, 20, 21</sup>

In bone, nonstoichiometric hydroxyapatite ( $\text{Ca}_{10}(\text{PO}_4)_6(\text{OH})_2$ ; HA) crystals form within a highly organized matrix of collagen.<sup>22</sup> There is an ongoing debate regarding the nucleating potential of collagen fibrils in the absence of any other proteins.<sup>23–25</sup> Recently, AFM measurements of heterogeneous calcium phosphate nucleation rates on collagen showed that solutions stable for days in the absence of collagen produced nuclei in hours or less on collagen matrices.<sup>12</sup> At supersaturations below the solubility limit of amorphous calcium phosphate (ACP), HA formed directly, but when the concentration was raised to slightly above the solubility limit of ACP, the amorphous phase formed first (Figure 1J) before transforming to octacalcium phosphate ( $\text{Ca}_8\text{H}_2(\text{PO}_4)_6 \cdot 5\text{H}_2\text{O}$ ; OCP) (Figure 1.1K) and, finally, HA (Figure 1.1L). Analysis of nucleation rates (Figure 1.1M) gave interfacial energies two to three times less than those estimated for homogeneous nucleation and barriers that were smaller by more than an order of magnitude. Analysis of the size distribution of particles that, on average, grew versus those that dissolved (Figure 1.1N), provided an

estimate of the critical nucleus size. However, neither the change from HA nucleation to ACP nucleation nor the small values of critical size could be understood within classical nucleation theory. Comparison to cryoEM and titration analyses revealed a formation pathway involving assembly of multi-ion complexes, which offered a rationale for the unexpected formation of ACP precursor particles and the low value of the critical size.

### *1.2.3 Cryo-EM and tomography: high-resolution, three-dimensional imaging of hydrated samples*

CryoEM techniques<sup>26</sup> can provide insights into tissue structures at close to native state.<sup>27, 28</sup> They can also be used to provide quasi-time resolved studies of nucleation and growth processes.<sup>29–33</sup> These studies can complement *in situ* AFM studies, and provide a more detailed picture of mineralization occurring *within* an organic matrix. For example, cryoEM studies of synthetic intrafibrillar HA formation in collagen fibrils revealed the early stages of infiltration of ACP particles at the hole zones in the fibrils (**Figure 1.2A,B**).<sup>34</sup> CryoEM tomography of the fully mineralized fibrils revealed embedded nm-thick plate-shaped HA crystals with their *c*-axis parallel to the fibril axis. Similar cryoEM approaches have been taken to study other composite systems such as calcium carbonate nucleation under Langmuir–Blodgett monolayers.<sup>29, 35</sup> In these studies, amorphous calcium carbonate (ACC) forms and then transforms to either calcite (in the absence of the monolayer) or vaterite and then calcite (with the monolayer present) by dissolution/reprecipitation.<sup>29</sup>

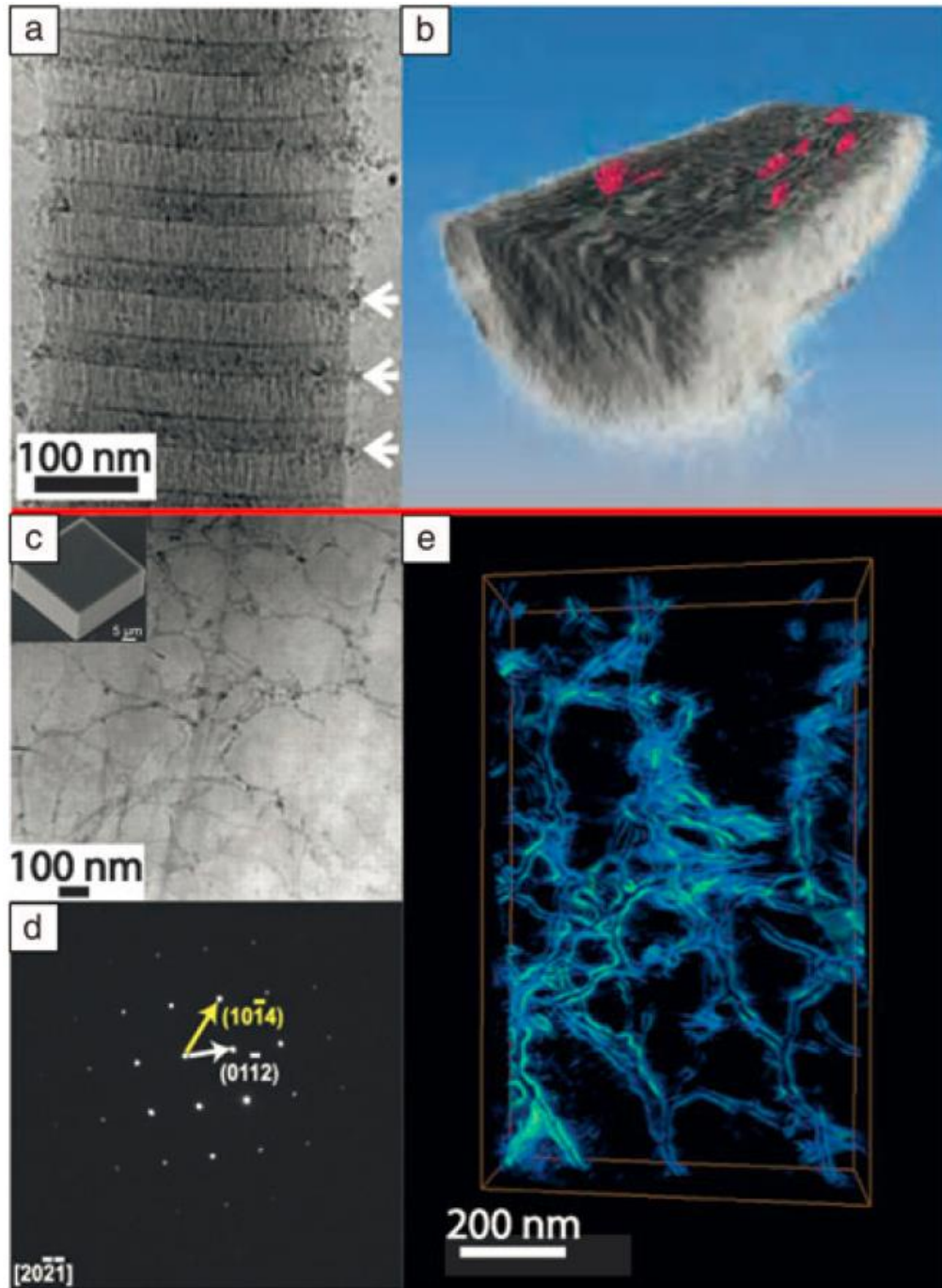


**Figure 1.2** (A, B) Cryogenic electron microscopy yields insights into the mineralization of hydrated samples. (A) CryoTEM of a collagen fibril (from horse tendon) with amorphous calcium phosphate (ACP) particles collecting near the hole regions of the collagen (white arrows) after mineralization for 24 hrs in buffered

CaCl<sub>2</sub>, KPO<sub>4</sub>, and 10 µg/mL of pAsp. (B) Tomographic reconstruction of the fibril after the apatite has been fully crystallized (72 hrs in buffered solution) reveals platelets (colored red) of mineral within the fibril itself. (C)–(E) Electron microscopy and tomography reveal details of incorporated macromolecular additives. (C) ADF-scanning transmission electron microscopy (STEM) of a focused ion beam section of a calcite crystal (scanning electron microscopy, inset) grown in a 1 w/v% agarose gel. Despite well-developed rhombohedral crystal, agarose gel fibers are clearly visible (darker contrast) randomly distributed within the thin section. (D) Selected-area electron diffraction of the area imaged in (C) demonstrating that the gel-grown crystal diffracts electrons as a single crystal. (E) ADF-STEM tomographic reconstruction of an area similar to (C) which emphasizes the network of agarose fibers incorporated within the crystal. (A and B) Adapted and reprinted by permission from Macmillan Publishers Ltd: Ref. 34 copyright 2010. (C and D) adapted from Ref. 63 with permission from AAAS copyright 2009.

#### *1.2.4 In situ TEM: direct observation of nucleation in bulk solutions and within organic matrices*

When nucleation occurs in bulk solution or within a biomimetic matrix, AFM cannot be used to observe the nucleation process. *In situ* liquid phase TEM provides a novel technique in these instances.<sup>36–41</sup> A sealed liquid cell on a specialized TEM holder (**Figure 1.3A,B**) allows for mixing reagents at the entrance to the cell and flow of the mixture through the cell.<sup>42</sup> Alternatively, the cell can be filled with one reagent through one of the two flow lines, and the second reagent can be introduced by

gaseous diffusion through the second line.<sup>43</sup> To observe nucleation within a macromolecular matrix, the macromolecules are added to one of the two reagents and transferred into the cell prior to introduction of the second reagent. The appearance of mineral nuclei and the spatial relationship to an organic matrix can then be observed by TEM imaging. Electron diffraction is used to determine the phase of the mineral and its evolution. Low-dose methods, beam shuttering, and examination of regions not previously exposed to the beam are required to separate electron beam effects from intrinsic phenomena.<sup>44, 45</sup> Liquid phase TEM was used to observe calcium carbonate ( $\text{CaCO}_3$ ) nucleation both in organic-free solutions<sup>42</sup> and in the presence of an organic matrix.<sup>43</sup> Results on pure solutions produced by mixing of two aqueous reagents demonstrated that multiple nucleation pathways can be simultaneously operative, including formation both directly from solution and indirectly through transformation of initially formed amorphous or crystalline precursors.<sup>42</sup> When crystalline phases formed as secondary phases through transformation of primary ACC, the secondary nuclei appeared at the surface of the ACC particles and remained in direct contact until the ACC was consumed. When ACC dissolution was induced, the observed behavior suggested ACC comprises a spectrum of structures ranging from dense liquids to solids.

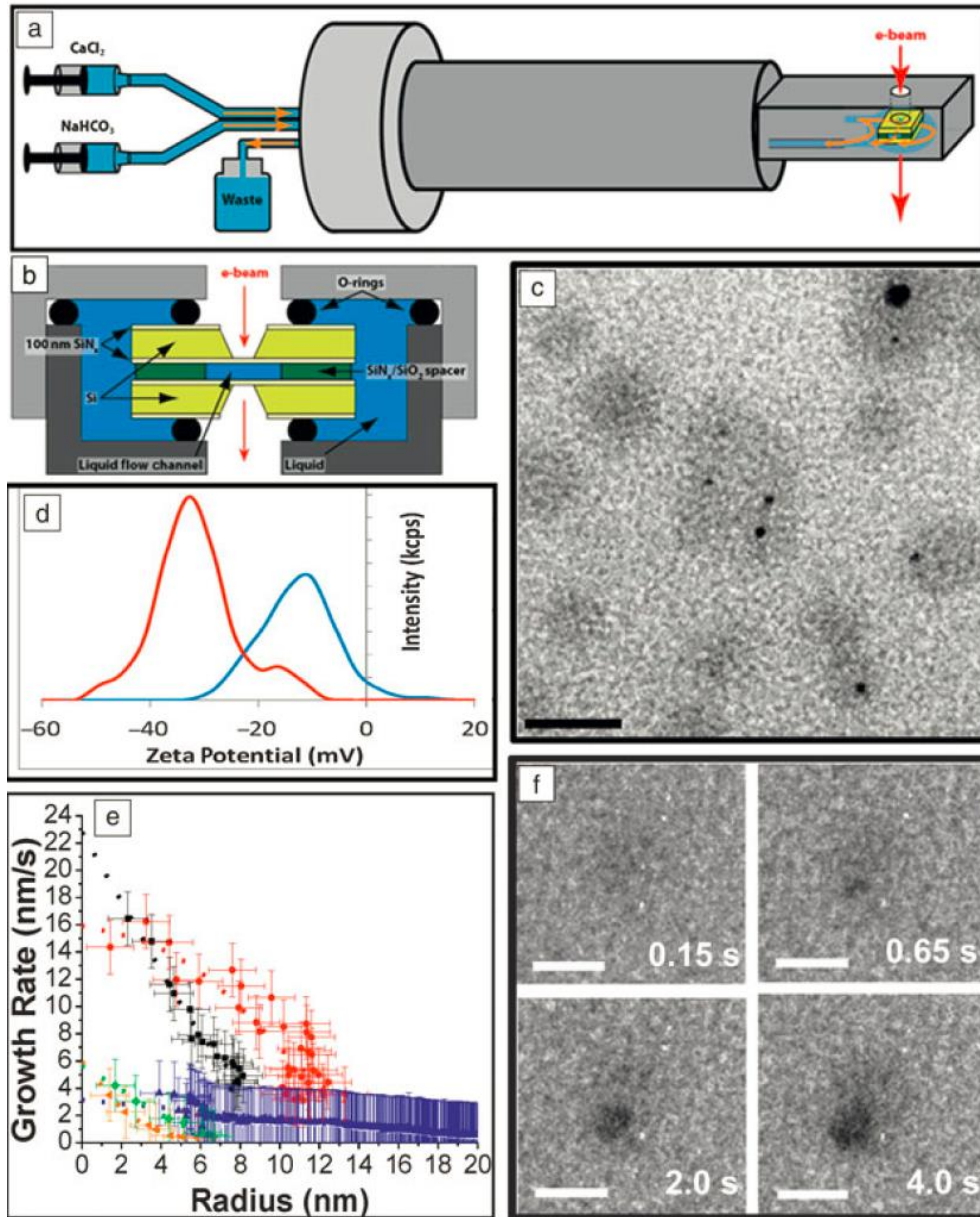


**Figure 1.3** *In situ* liquid phase transmission electron microscopy (TEM) enables observation of nucleation and phase evolution for both mineral and organic components. Schematic of (A) TEM liquid cell holder and (B) liquid cell. (C) Globules (gray) formed through  $\text{Ca}^{2+}$  counter-ion condensation on polystyrene sulfonate (PSS), some containing newly formed amorphous calcium carbonate (ACC)

particles (black). (D) Zeta potential showing shift to more positive values due to  $\text{Ca}^{2+}$  binding to PSS to form globules (red—pure  $\text{CaCl}_2$  solution, blue— $\text{CaCl}_2$  solution containing PSS). (E) Growth rates of vaterite particles (orange, green, blue) formed in the absence of PSS and ACC particles (black and red) within Ca-PSS globules. (F) Time series showing ACC nucleation and growth within a globule. In absence of PSS, vaterite forms randomly (not shown). Scale bars: (C) 50 nm, (F) 20 nm. Adapted and reprinted (C-F) by permission from reference 43 Macmillan Publishers Ltd: copyright 2015. Also adapted and reprinted (A and B) from reference 42 with permission from AAAS copyright 2014.

To investigate the role of macromolecular matrices in directing mineralization, liquid phase TEM was also used to observe the nucleation and growth of  $\text{CaCO}_3$  in the presence of poly(styrene sulfonate) (PSS).<sup>43</sup> This acidic macromolecule was chosen to mimic the polysaccharides believed important in the formation of certain marine biominerals.<sup>46–48</sup> In the PSS-free system, the configuration used for these experiments led to random nucleation with vaterite, a metastable  $\text{CaCO}_3$  polymorph, being the dominant phase. When PSS was first introduced in the  $\text{CaCl}_2$  reagent, calcium binding to the polymer resulted in formation of Ca-PSS globules with an average diameter of approximately 10 nm (Figure 1.3C). These observations were complemented by titration calorimetry, which showed that more than 50% of the  $\text{Ca}^{2+}$  ions were complexed by PSS, zeta potential measurements (Figure 1.3D), and *in situ* Fourier transform infrared spectroscopy (FTIR), which demonstrated that the  $\text{Ca}^{2+}$  ions bound to the sulfate groups. Upon introduction of carbonate, ACC particles nucleated first but only formed within the globules (Figure 1.3C–F). Vaterite appeared at much later

times but only formed outside of the globules. Both phases grew at diffusion-limited rates (Figure 1.3E), from which the supersaturation at the time of nucleation could be determined. The findings demonstrated that ion binding can play a significant role in directing nucleation, independent of any control over interfacial free-energy, and that the acidic polymers redirect the nucleation pathway to ACC formation.

### ***1.3 Macromolecular inclusions in biominerals and bioinspired materials***

#### ***1.3.1 How are large additives incorporated into crystalline lattices?***

Understanding the internal structure of biominerals, and the interactions between biomacromolecules and growing inorganic crystals, is of great interest for developing bio-inspired synthetic materials with improved property profiles, as discussed in more detail in the article by Schenck and Kim in this issue. One outstanding challenge is the compositional and structural characterization of hierarchically-structured, hydrated, biomineralized tissues, which typically have significant quantities of nonperiodically arranged organics occluded within crystalline matrices. While *in situ* techniques provide insights into the very early stages of crystal nucleation and growth, due to sample size limitations of AFM fluid cells and *in situ* TEM, the final product cannot be structurally characterized. Additionally, for biological tissues, we often only have the final mineral product since we currently cannot image the formation processes *in vivo*.

Fortunately, in recent years, advanced characterization techniques have provided unprecedented resolution of the internal structure of biominerals and unique insights into the mechanisms of formation of these structures. The most useful

techniques enable simultaneous imaging of the organic and inorganic components, with nanometer-scale resolution, and when possible, chemically rich information.

### *1.3.2 Electron tomography: 3D structural information*

Electron microscopy, in particular scanning TEM (STEM), is particularly well-suited to simultaneously imaging organic and inorganic components with nanometer-scale resolution.<sup>49</sup> In addition, local crystallographic information can be obtained by selected-area electron diffraction (SAED), and where possible, high-resolution lattice imaging can provide additional insight into crystal structure.<sup>50</sup> Immunogold labeling can be used in conjugation with TEM to visualize the locations of specific proteins within a tissue sample.<sup>51-54</sup> Briefly, small (<10 nm) gold nanoparticles are functionalized with antibodies and allowed to bind to target proteins within tissue thin sections. The high electron density of the gold nanoparticles facilitates imaging by TEM.

More recently, electron tomography, in which a series of images of the sample are taken at varying tilt angles with respect to the electron beam and reconstructed into a 3D image of the sample,<sup>55, 56</sup> has emerged as a technique for obtaining additional spatial information about the distribution of organic inclusions within biominerals. Energy dispersive spectroscopy (EDS) and electron energy-loss spectroscopy (EELS) can provide additional chemical information about the samples, but both techniques require high accelerating voltages. One of the main challenges in performing these types of experiments on biomineralized tissues is that samples must be electron transparent, which often requires thinning of samples via focused ion beam (FIB)

milling. As alternatives to FIB, other techniques can be used to obtain ultrathin sections such as cutting with a (cryo)ultramicrotome or wedge polishing hard tissue samples.<sup>20, 57</sup> Additionally, beam damage can be a problem for samples with high organic content as it can introduce imaging artifacts such as amorphization of crystalline regions, crystallization of amorphous regions, and destruction of organic regions.

Mollusk shells are a model biomineral that have been extensively studied due to their dramatically higher hardness and fracture toughness as compared to geologic minerals.<sup>58</sup> Electron microscopy and tomography have revealed details regarding the incorporation of biomacromolecules within the CaCO<sub>3</sub> single crystals that make up both the prismatic (calcitic) and nacreous (aragonitic) layers.<sup>59–61</sup> In all of these studies, a common picture emerges of single-crystal components (from SAED) with nanoscale inclusions, which are often arranged along preferred crystallographic orientations (from electron tomography). In another study, a combination of annular dark field STEM, electron tomography, SAED, and EELS were used to analyze the remarkably structured calcite building blocks of coccolithophores (single-celled algae).<sup>62</sup>

Inspired by biominerals such as mollusk shells, there have been several recent studies on the incorporation of nanoscale aggregates of organic macromolecules into synthetic single crystals of calcite (see Schenck and Kim article for additional discussion).<sup>63, 64</sup> The internal structure of calcite crystals grown within an agarose gel was revealed by electron tomography (Figure 1.2C–E). Similar to biogenic crystals,

the presence of the nanoscale gel fibers within the crystal did not appear to disrupt the local crystalline structure. Even more interestingly, the cavities in which the fibers were encased appeared to be faceted and contained high-energy homocharged {012} facets as well as the expected {104} cleavage planes.

These studies reveal the power of electron tomography for revealing the internal structure of biominerals and bio-inspired crystals. What these static techniques cannot capture, however, are the mechanisms by which the organic macromolecules become trapped within the crystals without significantly disrupting the lattice. Future studies will aim to apply AFM, cryoEM and/or liquid cell TEM to visualize the growth of crystals in the presence of these nanoscale additives.

### *1.3.3 Atom probe tomography: spatially resolved chemical information at the nanoscale*

Atom probe tomography offers both 3D imaging and chemical composition measurements at the atomic scale (around 0.1-0.3 nm resolution in depth and 0.3-0.5 nm laterally).<sup>65, 66</sup> This technique is currently the only way to chemically map inclusions in biominerals, in detail, at the nanoscale. Using FIB and nanomanipulators, needle-shaped samples are milled and mounted to a Si post array. Then a pulsed ultraviolet laser sequentially triggers field evaporation of single atoms or small clusters from the surface of the tip. The resulting ions are projected onto a position sensitive detector (PSD) and their time-of-flight, and thus chemical identity, is determined. The detector simultaneously measures 1) the time between the laser flash and the arrival on the PSD to determine the mass over charge ratio of the ions and 2)

the X-Y position and the order of arrival of the ions on the PSD to reconstruct the original position of the atoms in the sample. By repeating this operation, the atoms are progressively removed from the sample, and a 3D image of the material can be reconstructed at the atomic scale (**Figure 1.4A**). The small size of the sample, however, limits the overall image size and since the ejected organic fragments tend to be larger than single ions, the resolution of their location is slightly reduced. Though this technique was originally developed for studies of metals and semiconductors, recent advancements have made studies of composite and biological materials possible<sup>66–68</sup> and, despite challenges, the results reported so far are groundbreaking.

The first pioneering application of APT to the study of biomineral composites was to the tooth of a chiton, a small marine mollusk whose teeth are designed to scrape algae off of rocks.<sup>69</sup> Their teeth have a hard magnetite exterior and several organic-inorganic interfaces that are of interest. The APT revealed a 2–4 nm boundary-like region where the organic and inorganic materials are interspersed. The authors speculate that this interphase likely improves adhesion between the chemically disparate regions. A similar approach has been applied to dentin from elephant teeth.<sup>70</sup> APT revealed long organic fibers running parallel to the tooth direction with cross-sectional dimensions on the order of the width of a collagen microfibril (**Figure 1.4B**). They also found that the fibers have locally increased concentrations of  $\text{Mg}^{2+}$  and  $\text{Na}^+$  ions (**Figure 1.4C–D**) and theorize that the exterior of the fibers may be coated with noncollagenous proteins, which selectively bind ions and may aid in mineralization. In other work, details of the chemical composition and spatial heterogeneity of rodent enamel have been elucidated using APT.<sup>71</sup> The unique chemical insights from APT

allow for conclusions to be drawn about mechanisms of biomineral formation and function based on spatially resolved chemical information.

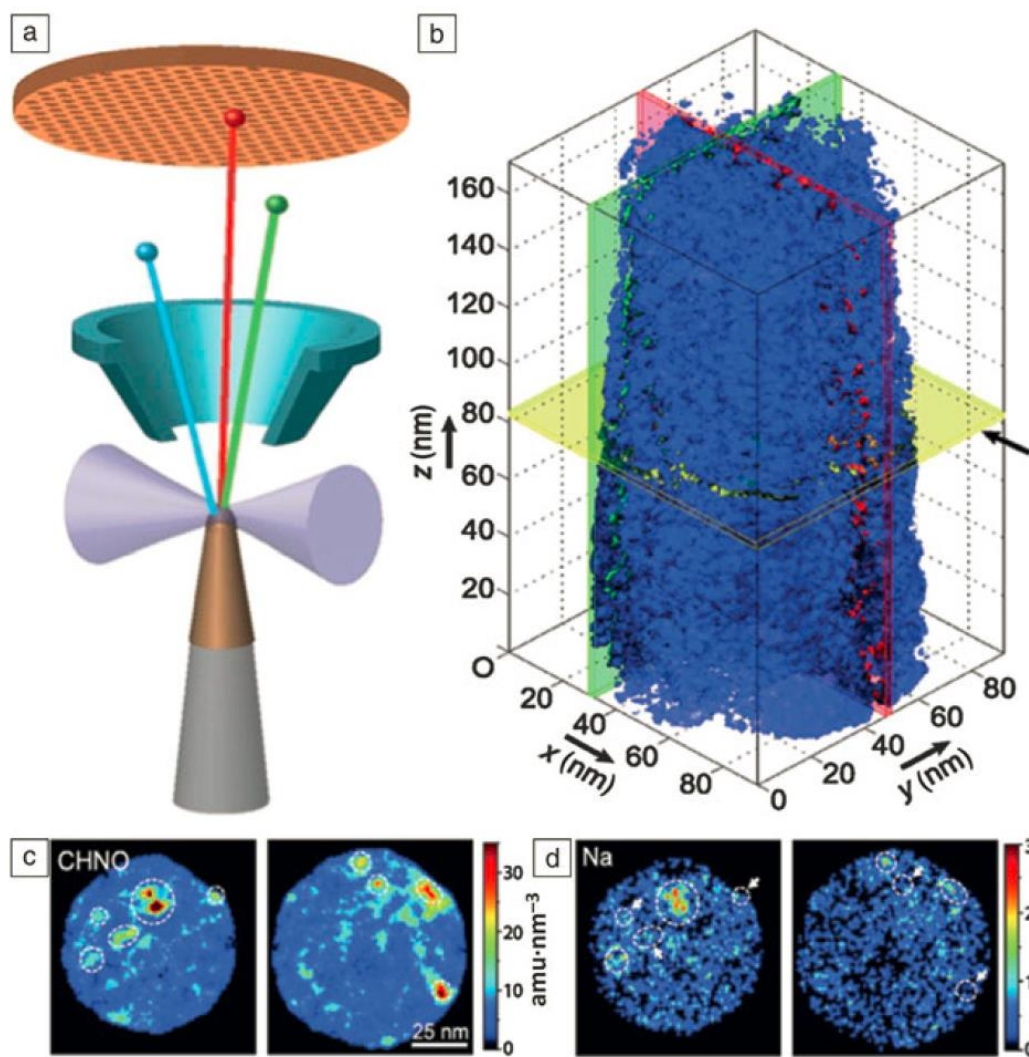


**Figure 1.4** (A) Schematic of an atom probe tomography experiment in which the sample is ablated by a laser (forming ions) onto a mass spectrometer to determine the type of atoms within the removed section. (B) Tomographic reconstruction of an elephant dentin sample shows the isosurface for the organic fragment number density (blue surface is the threshold for dense organic) revealing fibers aligned along the z

axis. (C) and (D) Selected sections from the reconstruction in (B) with mass density for organic fragments (C) and Na<sup>+</sup> (D) locations shown. The highest density regions for each are often, but not exclusively, the same, which implies that something in the organic macromolecules may bind the ions. Scale for (C) and (D) are the same as (B) *x*-*y* plane. Adapted and reprinted with permission from Ref. 70, copyright 2012.

#### *1.3.4 X-ray spectroscopy: mapping amorphous to crystalline transformations*

X-ray spectroscopy techniques, including x-ray absorption fine structure (EXAFS) and x-ray absorption near-edge spectroscopy (XANES), coupled with x-ray photoelectron emission microscopy (X-PEEM), have yielded many insights into the structures of biominerals.<sup>72-79</sup> Sample preparation is relatively minimal compared to other techniques (typically embedding in resin and polishing), but some of the techniques are surface-sensitive (depending on the wavelength of x-rays used), requiring additional attention to avoid artifacts from surface-layers left by polishing.

EXAFS spectra contain information about local structure and therefore can distinguish between amorphous and crystalline phases. X-PEEM studies have provided a detailed picture of the amorphous to crystalline transformation in a variety of biomineralized tissues. The use of amorphous precursors in biomineralization has attracted much attention as a synthetic route to morphologically complex single crystals.<sup>80</sup> For example, a recent study of larval sea urchin spicules, mineralized skeletal components, revealed that ACC nanoparticles unexpectedly persisted despite crystallization of the surrounding material.<sup>81</sup> To-date, most studies have focused on characterizing the inorganic component of biominerals, however, the organic

component can also be probed by looking at the carbon K-edge in the EXAFS spectra, as shown in several recent studies.<sup>82-84</sup>

### *1.3.5 Vibrational spectromicroscopy: chemically rich 3D maps of tissue composition*

Vibrational (Raman and infrared) spectromicroscopy can non-destructively provide spatially-resolved (0.5-1  $\mu\text{m}$ ) compositional information about the organic and inorganic components of biominerals.<sup>85, 86</sup> These techniques consist of a spectrometer coupled to a standard or confocal optical microscope, with the excitation source (laser or IR) focused on the sample through an objective lens. Two-dimensional images, with a spectrum at each pixel, are generated by raster-scanning the stage under the excitation source over a selected area.

Confocal Raman microscopy was recently used to analyze stomatopod raptorial appendages, which are used by the organism to “club” or “spear” prey (depending on the species) at very high velocities.<sup>87,88</sup> In this study, the authors constructed compositional gradient maps which revealed a transition from ACC to amorphous calcium phosphate at the bulk-impact interface, and finally, to highly crystalline sulfate-containing fluorapatite (FAP) along the actual impact surface.<sup>77</sup> Importantly, the sensitivity of the Raman technique allowed discernment of FAP from apatite, which could not be done on the basis of standard x-ray diffraction alone.

Confocal Raman spectromicroscopy can also be used to characterize compositional changes within 3D structures.<sup>89-92</sup> In addition to 2D and 3D compositional maps, polarized Raman microspectroscopy can provide quantification of molecular and crystallographic orientation. For example, Masic et al. were able to

observe multiscale orientational changes in rat tail tendon (Type I) collagen under stress.<sup>93</sup> Finally, one of the most promising applications of Raman is *in vivo* imaging, and the capability to couple Raman microscopes with other techniques, such as fluorescence microscopy. For example, bone formation in zebrafish larvae was recently observed *in vivo*.<sup>94, 95</sup> Anesthetized fish were analyzed under a water-immersion objective using a fluorescence-enabled modified Raman setup. Spectra were acquired along growing bones in the fin rays and showed a clear transition from little or no calcium phosphate to a predominance of calcium phosphate, correlated with calcein fluorescence (a calcium-binding marker). Furthermore, the mineral peaks suggested that octacalcium phosphate (OCP), or an OCP-like intermediate phase, may be present, a finding previously undocumented *in vivo*.

#### ***1.4 Conclusions***

The development and application of advanced microscopy and spectroscopy techniques, some of which can be performed *in situ*, have been essential for understanding the structure and formation of biominerals and bio-inspired materials. The information provided by these techniques about the chemistry, crystallography, phase distribution, structure, energetics, and kinetics of these materials forms the basis for an increasingly diverse understanding of the fundamental mechanisms by which natural systems can create structures. Yet we are only beginning to effectively mimic these processes synthetically. Fully understanding incorporated organic materials and the role they play in composite crystals will lead to further developments at the leading edge of characterization and synthesis.

Numerous recent advances in AFM imaging promise to provide new insights into biomineralization processes. High speed imaging<sup>96-98</sup> with image collection times below 100 ms should enable researchers to probe the conformational fluctuations and transformations that control the emergence of order during the assembly of an organic matrix. Frequency Modulated AFM (FM-AFM)<sup>99-101</sup> is capable of both imaging the structure of the near-surface water layers at solid interfaces in solutions and measuring the small attractive forces barriers between the tip and sample during the approach to the surface. These capabilities will lead to new insights into the role of solvation forces and solvent-mediated matrix-mineral interactions in directing biomineral formation.

Several of the other techniques described in this review, such as liquid phase TEM, are still in their infancy. Development of liquid cells for TEM instrumented for pH measurement, heating and cooling, and quantitative mixing will enable a wider range of experiments with well-defined solution saturation states. Solution supersaturation is a critical parameter to quantify in order for the resulting data regarding nucleation and growth modes to be interpreted in terms of theoretical predictions or compared to computer simulations. These and other developments will further enhance the applicability of liquid phase TEM for studying crystallization and matrix assembly.

New techniques, beyond those described here, are also emerging that have the potential to provide even more detailed spatial and temporal resolution of biomineralization processes in hydrated (fluid) environments. For example, the recent

implementation of scanning transmission x-ray microscopy end stations on synchrotron sources with resolution down to 10–20 nm<sup>102</sup> has enabled elemental mapping of hybrid organic/inorganic structures in fluid.<sup>103, 104</sup> Another development is a new type of scanning electron microscope (e.g., airSEM<sup>TM</sup>) in which fully-hydrated and uncoated samples can be imaged in air, allowing *in situ* observation of processes, such as calcium transport, in living organisms.<sup>95, 105</sup> The airSEM<sup>TM</sup> enables correlative imaging of tissues under ambient conditions by light and fluorescence microscopy and electron microscopy with elemental analysis by EDS.<sup>94, 106</sup> Finally, new sample preparation techniques such as cryo-FIB, in which cryogenically frozen samples are thinned by a focused ion beam will enhance our ability to prepare electron-transparent samples of biological samples under near-native conditions.<sup>107</sup>

The future holds the promise of integrating several of these techniques to allow for correlative imaging and, for example, link structural and compositional variations to changes in properties, such as elastic moduli or hardness. Ultimately, the knowledge gained through such studies will enable materials scientists to reproduce the remarkable properties of biominerals through bio-inspired approaches to materials synthesis.

## REFERENCES

1. H. Lowenstam, S. Weiner, *On Biomineralization* (Oxford University Press Inc., 1989).
2. P. M. Dove, J. J. De Yoreo, S. Weiner, *Biomineralization* (Mineral Society of America) (Washington, DC, 2003).
3. E. Asenath-Smith, H. Li, E. C. Keene, Z. W. Seh, L. A. Estroff, *Adv. Funct. Mater.* 22, 2891 (2012).
4. F. Nudelman, N. A. J. M. Sommerdijk, *Angew. Chemie - Int. Ed.* 51, 6582 (2012).
5. A. Arakaki, K. Shimizu, M. Oda, T. Sakamoto, T. Nishimura, T. Kato, *Org. Biomol. Chem.* 13, 974 (2014).
6. C. M. Franz, D. J. Muller, *Methods Mol. Biol.* 736, 97 (2011).
7. J. J. De Yoreo, *AIP Conference Proceedings*, 916, 416 (2007).
8. L. N. Rashkovich, J. J. Yoreo, C. A. Orme, A. A. Chernov, *Crystallogr. Reports.* 51, 1063 (2006).
9. D. A. Cisneros, C. Hung, C. M. Franz, D. J. Muller, *J. Struct. Biol.* 154, 232 (2006).
10. S. Chung, S.-H. Shin, C. R. Bertozzi, J. J. De Yoreo, *Proc. Natl. Acad. Sci. U. S. A.* 107, 16536 (2010).
11. B. Narayanan, G. H. Gilmer, J. Tao, J. J. De Yoreo, C. V Ciobanu, *Langmuir.* 30, 1343 (2014).

12. W. J. E. M. Habraken, J. Tao, L. J. Brylka, H. Friedrich, L. Bertinetti, A. S. Schenk, A. Verch, V. Dmitrovic, P. H. H. Bomans, P. M. Frederik, J. Laven, P. van der Schoot, B. Aichmayer, G. de With, J. J. DeYoreo, N. A. J. M. Sommerdijk, *Nat. Commun.* 4, 1507 (2013).
13. L. M. Hamm, A. J. Giuffre, N. Han, J. Tao, D. Wang, J. J. De Yoreo, P. M. Dove, *Proc. Natl. Acad. Sci. U. S. A.* 111, 1304 (2014).
14. J. D. Rimer, Z. A. N., Z. Zhu, M. H. Lee, D. S. Goldfarb, J. A. Wesson, M. D. Ward, *Science*. 330, 337 (2010).
15. C. A. Orme, A. Noy, A. Wierzbicki, M. T. McBride, M. Grantham, H. H. Teng, P. M. Dove, J. J. DeYoreo, *Nature*. 411, 775 (2001).
16. K. N. Olafson, M. A. Ketchum, J. D. Rimer, P. G. Vekilov, *Proc. Natl. Acad. Sci. U. S. A.*, doi: 10.1073/pnas.1501023112 (2015).
17. J. J. De Yoreo, L. A. Zepeda-Ruiz, R. W. Friddle, S. R. Qiu, L. E. Wasylenki, A. A. Chernov, G. H. Gilmer, P. M. Dove, *Cryst. Growth Des.* 9, 5135 (2009).
18. R. W. Friddle, M. L. Weaver, S. R. Qiu, A. Wierzbicki, W. H. Casey, J. J. De Yoreo, *Proc. Natl. Acad. Sci. U. S. A.* 107, 11 (2010).
19. J. P. R. O. Orgel, T. C. Irving, A. Miller, T. J. Wess, *Proc. Natl. Acad. Sci. U. S. A.* 103, 9001 (2006).
20. J. Tao, K. C. Battle, H. Pan, E. A. Salter, Y.-C. Chien, A. Wierzbicki, J. J. De Yoreo, *Proc. Natl. Acad. Sci. U. S. A.* 112, 326 (2014).
21. J. J. De Yoreo, S. Chung, R. W. Friddle, *Adv. Funct. Mater.* 23, 2525 (2013).
22. S. Weiner, H. D. Wagner, *Annu. Rev. Mater. Sci.* 28, 271 (1998).

23. W. J. Landis, F. H. Silver, *Cells. Tissues. Organs.* 189, 20 (2009).
24. Y. Wang, T. Azaïs, M. Robin, A. Vallée, C. Catania, P. Legriel, G. Pehau-  
Arnaudet, F. Babonneau, M.-M. Giraud-Guille, N. Nassif, *Nat. Mater.* 11, 724 (2012).
25. M. J. Olszta, X. Cheng, S. S. Jee, R. Kumar, Y.-Y. Kim, M. J. Kaufman, E. P.  
Douglas, L. B. Gower, *Mater. Sci. Eng. Res.* 58, 77 (2007).
26. F. Nudelman, G. de With, N. A. J. M. Sommerdijk, *Soft Matter.* 7, 17 (2011).
27. B. D. Quan, E. D. Sone, *Methods Enzymol.* 532, 189 (2013).
28. E. D. Sone, S. Weiner, L. Addadi, *J. Struct. Biol.* 158, 428 (2007).
29. B. P. Pichon, P. H. H. Bomans, P. M. Frederik, N. A. J. M. Sommerdijk, *J.*  
*Am. Chem. Soc.* 130, 4034 (2008).
30. C. C. M. C. Carcouët, M. W. P. van de Put, B. Mezari, P. C. M. M. Magusin, J.  
Laven, P. H. H. Bomans, H. Friedrich, A. C. C. Esteves, N. A. J. M. Sommerdijk, R.  
A. T. M. van Benthem, G. de With, *Nano Lett.* 14, 1433 (2014).
31. C. Frandsen, B. A. Legg, L. R. Comolli, H. Zhang, B. Gilbert, E. Johnson, J. F.  
Banfield, *CrystEngComm.* 16, 1451 (2014).
32. P.-A. Fang, J. F. Conway, H. C. Margolis, J. P. Simmer, E. Beniash, *Proc.*  
*Natl. Acad. Sci. U. S. A.* 108, 14097 (2011).
33. P.-A. Fang, H. C. Margolis, J. F. Conway, J. P. Simmer, E. Beniash, *J. Struct.*  
*Biol.* 183, 250 (2013).
34. F. Nudelman, K. Pieterse, A. George, P. H. H. Bomans, H. Friedrich, L. J.  
Brylka, P. A. J. Hilbers, G. de With, N. A. J. M. Sommerdijk, *Nat. Mater.* 9, 1004  
(2010).

35. E. M. Pouget, P. H. H. Bomans, J. A. C. M. Goos, P. M. Frederik, G. de With, N. A. J. M. Sommerdijk, *Science*. 323, 1455 (2009).
36. M. J. Williamson, R. M. Tromp, P. M. Vereecken, R. Hull, F. M. Ross, *Nat. Mater.* 2, 532 (2003).
37. C.-M. Wang, H.-G. Liao, F. M. Ross, *MRS Bull.* 40, 46 (2015).
38. H. Zheng, Y. S. Meng, Y. Zhu, *MRS Bull.* 40, 12 (2015).
39. E. A. Sutter, P. W. Sutter, *J. Am. Chem. Soc.* 136, 16865 (2014).
40. D. Li, M. H. Nielsen, J. J. De Yoreo, *Methods Enzymol.* 532, 147 (2013).
41. M. H. Nielsen, D. Li, H. Zhang, S. Aloni, T. Y.-J. Han, C. Frandsen, J. Seto, J. F. Banfield, H. Cölfen, J. J. De Yoreo, *Microsc. Microanal.* 20, 1 (2014).
42. M. H. Nielsen, S. Aloni, J. J. De Yoreo, *Science*. 345, 1158 (2014).
43. P. J. M. Smeets, K. R. Cho, R. G. E. Kempen, N. A. J. M. Sommerdijk, J. J. De Yoreo, *Nat. Mater.* 14, 394 (2015).
44. T. J. Woehl, J. E. Evans, I. Arslan, W. D. Ristenpart, N. D. Browning, *ACS Nano*. 6, 8599 (2012).
45. H. Zhang, J. J. De Yoreo, J. F. Banfield, *ACS Nano*. 8, 6526 (2014).
46. L. Addadi, J. Moradian, E. Shay, N. G. Maroudas, S. Weiner, *Proc. Natl. Acad. Sci.* 84, 2732 (1987).
47. M. E. Marsh, *Protoplasma*. 177, 108 (1994).
48. A. S. Schenk, I. Zlotnikov, B. Pokroy, N. Gierlinger, A. Masic, P. Zaslansky, A. N. Fitch, O. Paris, T. H. Metzger, H. Cölfen, P. Fratzl, B. Aichmayer, *Adv. Funct. Mater.* 22, 4668 (2012).

49. A. A. Sousa, R. D. Leapman, *Ultramicroscopy*. 123, 38 (2012).
50. L. Kabalah-Amitai, B. Mayzel, Y. Kauffmann, A. N. Fitch, L. Bloch, P. U. P. A. Gilbert, B. Pokroy, *Science*. 340, 454 (2013).
51. A. Osuna-Mascaró, T. Cruz-Bustos, S. Benhamada, N. Guichard, B. Marie, L. Plasseraud, M. Corneillat, G. Alcaraz, A. Checa, F. Marin, *Comp. Biochem. Physiol. B. Biochem. Mol. Biol.* 168, 76 (2014).
52. T. Mass, J. L. Drake, E. C. Peters, W. Jiang, P. G. Falkowski, *Proc. Natl. Acad. Sci. U. S. A.* 111, 12728 (2014).
53. L. Ameye, R. Hermann, C. Killian, F. Wilt, P. Dubois, *J. Histochem. Cytochem.* 47, 1189 (1999).
54. J. Seto, Y. Zhang, P. Hamilton, F. Wilt, *J. Struct. Biol.* 148, 123 (2004).
55. P. A. Midgley, M. Weyland, *Ultramicroscopy*. 96, 413 (2003).
56. R. Leary, P. Midgley, J. Thomas, *Accounts Chem. Res.* 45 (2012).
57. P. M. Voyles, J. L. Grazul, D. A. Muller, *Ultramicroscopy*. 96, 251 (2003).
58. M. E. Kunitake, L. M. Mangano, J. M. Peloquin, S. P. Baker, L. A. Estroff, *Acta Biomater.* 9, 5353 (2013).
59. H. Li, H. L. Xin, M. E. Kunitake, E. C. Keene, D. a. Muller, L. A. Estroff, *Adv. Funct. Mater.* 21, 2028 (2011).
60. K. Gries, R. Kröger, C. Kübel, M. Fritz, A. Rosenauer, *Acta Biomater.* 5, 3038 (2009).
61. T. Okumura, M. Suzuki, H. Nagasawa, T. Kogure, *J. Cryst. Growth.* 381, 114 (2013).

62. R. van de Locht, T. J. A. T. Slater, R. van de Locht, T. J. A. T. Slater, A. Verch, J. R. Young, S. J. Haigh, R. Kröger, *Cryst. Growth Des.*, 140320115609006 (2014).
63. H. Li, H. L. Xin, D. A. Muller, L. A. Estroff, *Science*. 326, 1244 (2009).
64. Y.-Y. Kim, K. Ganesan, P. Yang, A. N. Kulak, S. Borukhin, S. Pechook, L. Ribeiro, R. Kröger, S. J. Eichhorn, S. P. Armes, B. Pokroy, F. C. Meldrum, *Nat. Mater.* 10, 890 (2011).
65. D. N. Seidman, *Annu. Rev. Mater. Res.* 37, 127 (2007).
66. M. K. Miller, R. G. Forbes, *Mater. Charact.* 60, 461 (2009).
67. T. F. Kelly, O. Nishikawa, J. A. Panitz, T. J. Prosa, *MRS Bull.* 34, 744 (2009).
68. E. A. Marquis, M. Bachhav, Y. Chen, Y. Dong, L. M. Gordon, A. McFarland, *Curr. Opin. Solid State Mater. Sci.* 17, 217 (2013).
69. L. M. Gordon, D. Joester, *Nature*. 469, 194 (2011).
70. L. Gordon, L. Tran, D. Joester, *ACS Nano*, 10667 (2012).
71. L. M. Gordon, M. J. Cohen, K. W. MacRenaris, J. D. Pasteris, T. Seda, D. Joester, *Science*. 347, 746 (2015).
72. N. Tamura, P. U. P. A. Gilbert, *Methods Enzymol.* 532, 501 (2013).
73. C. Gilow, E. Zolotoyabko, O. Paris, P. Fratzl, B. Aichmayer, *Cryst. Growth Des.* 11, 2054 (2011).
74. E. Beniash, R. A. Metzler, R. S. K. Lam, P. U. P. A. Gilbert, *J. Struct. Biol.* 166, 133 (2009).

75. S. Weiner, J. Mahamid, Y. Politi, Y. Ma, L. Addadi, *Front. Mater. Sci. China*. 3, 104 (2009).
76. Y. Levi-Kalisman, S. Raz, S. Weiner, L. Addadi, I. Sagi, *J. Chem. Soc. Dalt. Trans.*, 3977 (2000).
77. J. Mahamid, B. Aichmayer, E. Shimoni, R. Ziblat, C. Li, S. Siegel, O. Paris, P. Fratzl, S. Weiner, L. Addadi, *Proc. Natl. Acad. Sci. U. S. A.* 107, 6316 (2010).
78. P. U. P. A. Gilbert, *J. Electron Spectros. Relat. Phenomena*. 185, 395 (2012).
79. Y. Ma, B. Aichmayer, O. Paris, P. Fratzl, A. Meibom, R. A. Metzler, Y. Politi, L. Addadi, P. U. P. A. Gilbert, S. Weiner, *Proc. Natl. Acad. Sci. U. S. A.* 106, 6048 (2009).
80. S. Weiner, L. Addadi, *Annu. Rev. Mater. Res.* 41, 21 (2011).
81. Y. U. T. Gong, C. E. Killian, I. C. Olson, N. P. Appathurai, A. L. Amasino, M. C. Martin, L. J. Holt, F. H. Wilt, P. U. P. A. Gilbert, *Proc. Natl. Acad. Sci. U. S. A.* 109, 6088 (2012).
82. R. A. Metzler, G. A. Tribello, M. Parrinello, P. U. P. A. Gilbert, *J. Am. Chem. Soc.* 132, 11585 (2010).
83. R. A. Metzler, J. S. Evans, C. E. Killian, D. Zhou, T. H. Churchill, N. P. Appathurai, S. N. Coppersmith, P. U. P. A. Gilbert, *J. Am. Chem. Soc.* 132, 6329 (2010).
84. R. S. K. Lam, R. A. Metzler, P. U. P. A. Gilbert, E. Beniash, *ACS Chem. Biol.* 7, 476 (2012).
85. S. Gamsjaeger, R. Mendelsohn, A. L. Boskey, S. Gourion-Arsiquaud, K. Klaushofer, E. P. Paschalis, *Curr. Osteoporos. Rep.* 12, 454 (2014).

86. A. C. S. Talari, Z. Movasaghi, S. Rehman, I. U.R. Rehman, *Appl. Spectrosc. Rev.* 50, 46 (2014).
87. J. C. Weaver, G. W. Milliron, A. Miserez, K. Evans-Lutterodt, S. Herrera, I. Gallana, W. J. Mershon, B. Swanson, P. Zavattieri, E. DiMasi, D. Kisailus, *Science*. 336, 1275 (2012).
88. S. Amini, A. Masic, L. Bertinetti, J. S. Teguh, J. S. Herrin, X. Zhu, H. Su, A. Miserez, *Nat. Commun.* 5, 3187 (2014).
89. K. Lee, W. Wagermaier, A. Masic, K. P. Kommareddy, M. Bennet, I. Manjubala, S.-W. Lee, S. B. Park, H. Cölfen, P. Fratzl, *Nat. Commun.* 3, 725 (2012).
90. S. H. K. Eder, A. M. Gigler, M. Hanzlik, M. Winklhofer, *PLoS One*. 9, e107356 (2014).
91. S. Omelon, J. Georgiou, F. Variola, M. N. Dean, *Acta Biomater.* 10, 3899 (2014).
92. A. A. Lloyd, Z. X. Wang, E. Donnelly, *J. Biomech. Eng.* 137, 010801 (2015).
93. A. Masic, L. Bertinetti, R. Schuetz, L. Galvis, N. Timofeeva, J. W. C. Dunlop, J. Seto, M. A. Hartmann, P. Fratzl, *Biomacromolecules*. 12, 3989 (2011).
94. M. Bennet, A. Akiva, D. Faivre, G. Malkinson, K. Yaniv, S. Abdelilah-Seyfried, P. Fratzl, A. Masic, *Biophys. J.* 106, L17 (2014).
95. A. Akiva, G. Malkinson, A. Masic, M. Kerschnitzki, M. Bennet, P. Fratzl, L. Addadi, S. Weiner, K. Yaniv, *Bone*. 75, 192 (2015).
96. T. Ando, N. Kodera, Y. Naito, T. Kinoshita, K. Furuta, Y. Y. Toyoshima, *ChemPhysChem*. 4, 1196 (2003).

97. M. Shibata, H. Yamashita, T. Uchihashi, H. Kandori, T. Ando, *Nat. Nanotechnol.* 5, 208 (2010).
98. N. Kodera, D. Yamamoto, R. Ishikawa, T. Ando, *Nature.* 468, 72 (2010).
99. T. Fukuma, S. P. Jarvis, *Rev. Sci. Instrum.* 77, 043701 (2006).
100. J. I. Kilpatrick, S.-H. Loh, S. P. Jarvis, *J. Am. Chem. Soc.* 135, 2628 (2013).
101. T. Fukuma, M. J. Higgins, S. P. Jarvis, *Biophys. J.* 92, 3603 (2007).
102. M. Obst, G. Schmid, in *Electron Microscopy: Methods and Protocols, Methods in Molecular Biology*, J. Kuo, Ed. (SPRINGER, 233 SPRING ST, NEW YORK, NY 10013 USA, New York, vol 1117., 2014).
103. J. Cosmidis, K. Benzerara, N. Nassif, T. Tyliczszak, J. Cosmidis, K. Benzerara, N. Nassif, T. Tyliczszak, F. B. Char, *Acta Biomater.* 12, 260 (2015).
104. Y. Li, F. El Gabaly, T. R. Ferguson, R. B. Smith, N. C. Bartelt, J. D. Sugar, K. R. Fenton, D. A. Cogswell, A. L. D. Kilcoyne, T. Tyliczszak, M. Z. Bazant, W. C. Chueh, *Nat. Mater.* 13, 1149 (2014).
105. N. Vidavsky, S. Addadi, J. Mahamid, E. Shimoni, D. Ben-Ezra, M. Shpigel, S. Weiner, L. Addadi, *Proc. Natl. Acad. Sci. U. S. A.* 111, 39 (2014).
106. I. Solomonov, D. Talmi-Frank, Y. Milstein, S. Addadi, A. Aleshin, I. Sagi, *Sci. Rep.* 4, 5987 (2014).
107. A. Rigort, F. J. B. Bäuerlein, E. Villa, M. Eibauer, T. Laugks, W. Baumeister, J. M. Plitzko, *Proc. Natl. Acad. Sci. U. S. A.* 109, 4449 (2012).

## CHAPTER 2

### MECHANISTIC INSIGHTS INTO NANOPARTICLE-CRYSTAL INTERACTIONS REVEALED VIA *IN SITU* ATOMIC FORCE MICROSCOPY (AFM)

Coit T. Hendley IV<sup>1</sup>, Lee A. Fielding<sup>2</sup>, Elizabeth R. Jones<sup>3</sup>, Anthony Ryan<sup>3</sup>, Steven P. Armes<sup>3</sup>, Lara Estroff<sup>1,4\*</sup>

<sup>1</sup>Department of Materials Science and Engineering, Cornell University, Ithaca, NY  
14853, USA.

<sup>2</sup>The School of Materials, University of Manchester, Oxford Road, Manchester, M13  
9PL, UK

<sup>3</sup>Department of Chemistry, University of Sheffield, Brook Hill, Sheffield, Yorkshire,  
S3 7HF, UK.

<sup>4</sup>Kavli Institute, Cornell University, Ithaca, NY 14853, USA.

#### **2.1 Abstract**

In recent years, it has become clear that single crystals can form composite structures with occluded additive materials. In the calcite model system, we have yet to fully understand the interactions at the organic-inorganic interface which is usually formed in these composites. We utilize *in situ* Atomic Force Microscopy (AFM) to visualize polymer nanoparticles with tunable surface chemistry as they interact with a growing calcite surface. Our results reveal three possible particle surface interactions:

attachment-detachment, attachment-incorporation, and attachment-hovering, where the particle remains on the surface while growth proceeds underneath. We also show that an ensemble of particles of a given surface chemistry is divided between these three interactions in an equilibrium. Further, the particle distribution within the equilibrium is dependent on surface chemistry. This work provides a framework for understanding how nanoparticles can interact with growing crystals.

## **2.2 Introduction**

Biom mineralization provides countless examples of the complexity that is accessible by manipulating crystallization via atomic substitution, or by using additives such as small molecules or proteins.<sup>1-3</sup> The structural diversity among biominerals is in part due to naturally-occurring macromolecular additives, which affect the nucleation and growth of the crystals and can become incorporated.<sup>2,4</sup> The mechanisms by which atomic substitutions and small molecules interact with the growing crystal are relatively well understood.<sup>5-11</sup> Incorporation of larger organic additives has been studied previously *ex situ* and more recently with *in situ* Atomic Force Microscopy (AFM) using peptides, proteins, and synthetic anionic block copolymer nanoparticles.<sup>12-16</sup> In particular, *in situ* studies have demonstrated that additive-crystal interactions with multivalent additives are complex, requiring a multistep process through a weak and strong binding state.<sup>17,18</sup> Thus a better understanding of the mechanisms of additive-crystal interactions is required to guide the rational synthesis of nanoscale additives designed to incorporate into single crystals. In this study, *in situ* AFM is used to analyze the surface interactions between

block copolymer nanoparticles (>10 nm diameter) and growing calcite ( $\text{CaCO}_3$ ) crystals.

One key aspect of additive-crystal interactions is that the occlusion mechanism depends on the additive size. Single atoms, small molecules (e.g., amino acids) and proteins are all found within calcitic biominerals and affect crystal growth differently.<sup>5,7,19,20</sup> For example,  $\text{Mg}^{2+}$  is readily incorporated into calcite by substituting for  $\text{Ca}^{2+}$  cations in the crystal structure.<sup>7,21</sup> In the case of amino acids the interaction with calcite is more complex, with chemical functionality determining the preference for binding to crystal surfaces at a growing step edge.<sup>6</sup> For example, glycine and aspartic acid preferentially bind to acute step edges of calcite growth hillocks.<sup>6</sup> Additionally, molecules that cannot easily fit into the crystal structure must be accommodated by larger vacancies within the crystal.<sup>5</sup> For larger molecules, i.e. peptides or polymers, length scales become important because the number of potential bonding units in a chain impacts the ability of such macromolecules to adsorb at a step edge. For example, a study using synthetic peptides showed that their potency of inhibition increases significantly for longer chains.<sup>22</sup> The dynamics of binding and crystal growth are even more complex for synthetic polymers; some longer chains can actually *enhance* crystal growth rates when present at very low concentration.<sup>22</sup> At the largest length scale, globular proteins and nanoparticles interact with a much larger surface area of the crystal, and as such the surface chemistry of such additives is expected to play a critical role in determining its mechanism of interaction with a growing crystal. For nanoparticles, very little is known about the design rules for

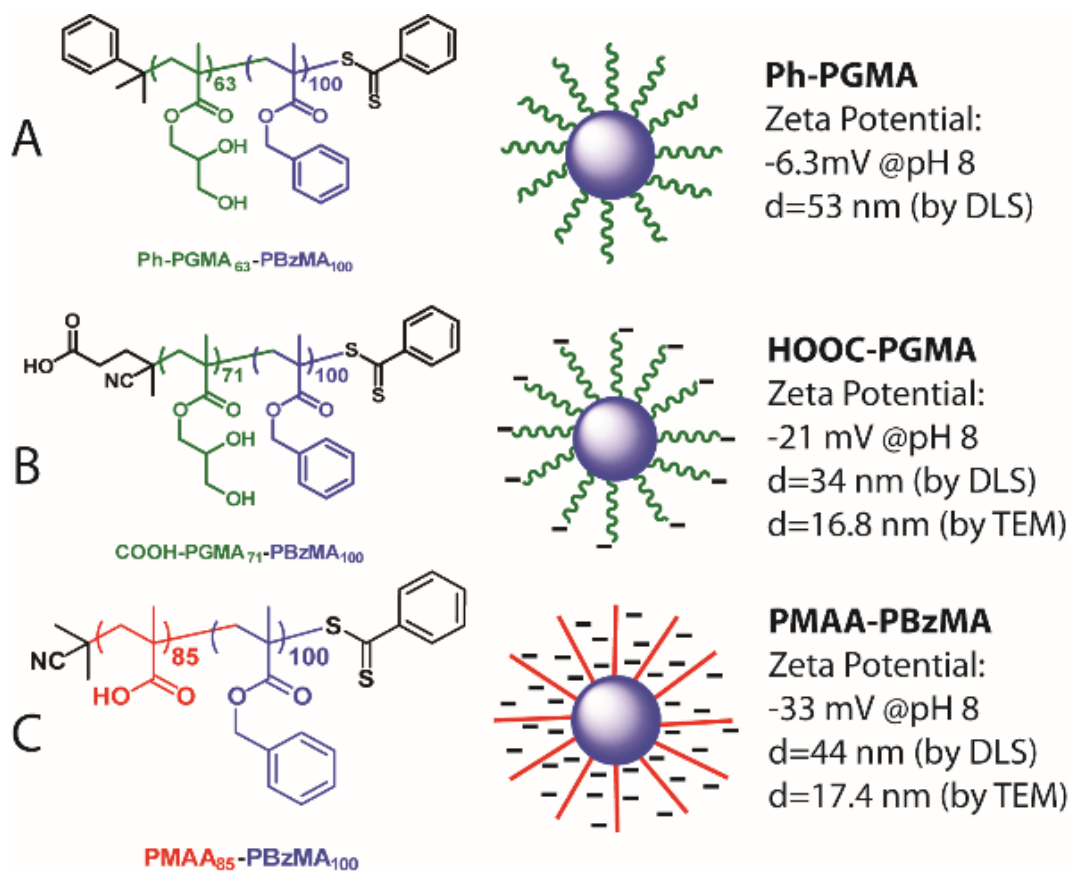
efficient occlusion other than the importance of anionic character and chemical functionality of the stabilizer chains.<sup>23-25</sup>

Based on extensive research over the past twenty years, the key factor driving nanoparticle incorporation into calcite is the surface chemistry and charge density of the anionic steric stabilizer chains. Particle incorporation was first demonstrated by Wegner and co-workers, who developed various anionic latexes that become occluded within calcite and ZnO single crystals.<sup>26,27</sup> More recently, Meldrum and co-workers demonstrated that surface-carboxylated polystyrene latexes could also be incorporated into calcite.<sup>24</sup> However, *isolated* anionic carboxylate groups were insufficient to ensure efficient occlusion: instead, polycarboxylated stabilizer chains were required, which suggests cooperativity is important for binding to the calcite lattice.<sup>24</sup> The same team, working closely with various other groups, subsequently showed that micellar diblock copolymer nanoparticles of ~15 nm diameter comprising an anionic poly(2-(succinyloxy)propyl methacrylate) (PSPMA) stabilizer block could also be incorporated into calcite crystals.<sup>25,28</sup> Recent progress has been made towards an empirical understanding of “design rules” for optimizing organic nanoparticle incorporation into calcite.<sup>23</sup> In particular, it appears that the relative surface density of anionic stabilizer chains can determine whether or not nanoparticle occlusion is observed.<sup>29</sup> Nevertheless, more detailed understanding of the nanoparticle occlusion mechanism(s) should inform the rational design of next-generation nanoparticles. In this context, direct observation of the nanoparticle-crystal interaction mechanism requires an *in situ* technique like AFM.

A recent *in situ* AFM study by De Yoreo and co-workers revealed the mechanisms by which individual carboxylated PSPMA-PDPA block copolymer micellar nanoparticles are incorporated into calcite.<sup>13</sup> A series of experiments demonstrated that these anionic copolymer nanoparticles strongly interact with calcite growth hillocks, binding to step edges, and quickly become engulfed under calcite growth conditions. Moreover, the occlusion mechanism appears to differ depending on the nanoparticle dimensions.<sup>13</sup> Particles of ~3 nm diameter are incorporated as spheres within the crystal lattice, but larger particles of ~15 nm diameter are compressed into an cylindrical shape, apparently leaving a small void between each particle and the nanoscale cavity that contains it within the crystal.<sup>13</sup> To understand the surface adsorption behavior of these anionic particles requires observing the particle-crystal interaction with a growth hillock “paused” at equilibrium. Such experiments demonstrated that the nanoparticles attach almost exclusively to step edges once they are bound to the calcite surface, implying either highly specific adsorption or rapid surface diffusion to these features.<sup>13</sup> Despite these useful mechanistic insights, the role of the anionic corona in influencing the mechanisms of nanoparticle-crystal surface interaction remains unknown. Exploring this aspect of nanoparticle occlusion within calcite is the primary objective of the present study.

## 2.3 Results

### 2.3.1 Experimental Design



**Scheme 2.1** Summary of the three types of diblock copolymer nanoparticles used in this study. (A) Non-ionic poly(glycerol monomethacrylate)-stabilized poly(benzyl methacrylate) nanoparticles (Ph-PGMA<sub>63</sub>-PBzMA<sub>100</sub>); (B) Poly(glycerol monomethacrylate)-stabilized poly(benzyl methacrylate) nanoparticles with a single carboxylic acid group located at the end of each PGMA stabilizer chain (HOOC-PGMA<sub>71</sub>-PBzMA<sub>100</sub>); (C) Anionic poly(methacrylic acid)-stabilized poly(benzyl methacrylate) nanoparticles (PMAA<sub>85</sub>-PBzMA<sub>100</sub>).

To effectively probe the mechanism(s) of nanoparticle-crystal interactions requires a series of nanoparticles with tunable surface chemistry. Polymerization-induced self-assembly (PISA)<sup>30,31</sup> via reversible addition-fragmentation chain transfer (RAFT) emulsion polymerization enables the synthesis of bespoke sterically-stabilized diblock copolymer nanoparticles with identical hydrophobic cores but different surface chemistries conferred by the hydrophilic stabilizer chains.<sup>23,32</sup> Moreover, the core-forming block can be selected to be optimal for the experiment. For example, an *in situ* AFM growth experiment works best with relatively hard, nonfilm-forming nanoparticles, which minimizes tip effects and also nanoparticle deformation after adsorption. Similar nanoparticles have been previously utilized for the study of occlusion within calcite<sup>23,25,28,29,33</sup> and zinc oxide<sup>34</sup>: nanoparticles with relatively long carboxylated stabilizer chains that are negatively charged under the growth conditions (~pH 8) are most readily incorporated. Given such a library of *ex situ* results, we expected that only nanoparticles with similar stabilizer chemistry would exhibit high levels of incorporation. The specific diblock copolymer nanoparticles utilized in this study comprise poly(benzyl methacrylate) (PBzMA) cores and either an ‘uncharged’ poly(glycerol methacrylate) (Ph-PGMA), ‘singly-charged’ poly(glycerol methacrylate) (HOOC-PGMA) or ‘anionic’ poly(methacrylic acid) (PMAA) corona (Scheme 1). Only the latter PMAA-based nanoparticles led to extensive incorporation into calcite. The single terminal anionic charge was imparted to HOOC-PGMA stabilizer chains by selecting an appropriate RAFT chain transfer agent (CTA) containing a carboxylic acid group. We targeted a mean degree of polymerization of 100 for the hydrophobic core-forming PBzMA block to minimize the effects of

nanoparticle size and deformation during calcite occlusion. As a result, these copolymer nanoparticles are relatively robust compared to the anionic copolymers with poly(2-hydroxypropyl methacrylate) cores used in previous studies<sup>13,25,28</sup> and are subsequently less susceptible to AFM tip artifacts. To examine the effect of systematically increasing the anionic character of the charge corona, we grew calcite in the presence of each type of nanoparticle both in the bulk (*ex situ*) and also using *in situ* AFM. The combination of *ex situ* and *in situ* experiments allows us to make direct comparisons between the three types of stabilizer block at different length scales.

### 2.3.2 Nanoparticle Characterization

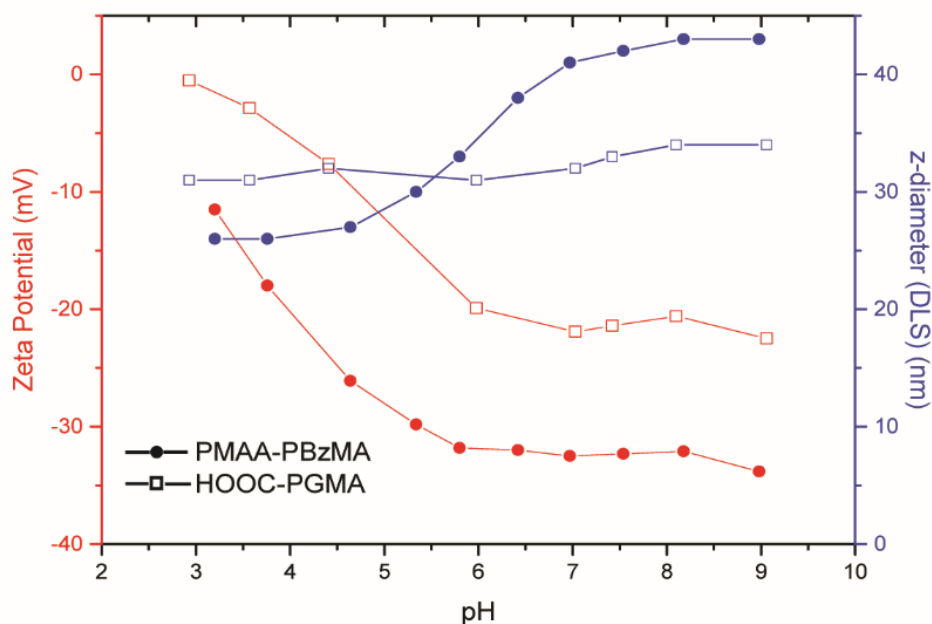


**Figure 2.1** Zeta potential (red) and DLS diameter (blue) measurements versus pH for both PMAA-PBzMA (filled circles) and HOOC-PGMA-PBzMA (open squares)

nanoparticles. Measurements were conducted in the presence of 1 mM KCl and titrated from basic to acidic pH using HCl.

Prior to any detailed AFM study of nanoparticle-calcite interactions, we examined the nanoparticles themselves. First, the zeta potential and z-average diameter were each determined as a function of pH (Figure 1). The zeta potential measured at pH 8 (the pH used for calcite growth) for all three nanoparticle types is listed in Scheme 1. There is no pH-dependence for the zeta potential of the non-ionic Ph-PGMA-PBzMA nanoparticles, whereas the HOOC-PGMA-PBzMA and PMAA-PBzMA nanoparticles acquire progressively greater anionic character at higher pH as the carboxylic acid groups become deprotonated. The diameter of the HOOC-PGMA-PBzMA nanoparticles remains relatively constant at ~34 nm while the PMAA-PBzMA nanoparticles increase from ~25 nm to ~45 nm diameter between pH 4 and pH 8. This observation is consistent with polyelectrolyte brush behavior, where a higher pH causes swelling of the coronal layer via extension of the increasingly anionic chains<sup>35,36</sup>. Therefore polyelectrolytic PMAA chains are likely to be in a more-stretched conformation than the PGMA chains due to coulombic repulsion between adjacent anionic groups. The HOOC-PGMA particles do not possess polyelectrolyte coronas and therefore do not exhibit such swelling behavior. We used transmission electron microscopy (TEM) and static AFM imaging on poly(L-lysine)-treated mica in fluid to confirm that these PBzMA-based nanoparticles could be imaged after their adsorption at a planar surface using AFM (Fig. S1). Indeed, nanoparticle diameters are very similar when imaged by TEM and AFM (~15 nm).

### 2.3.3 Calcite Growth Ex Situ

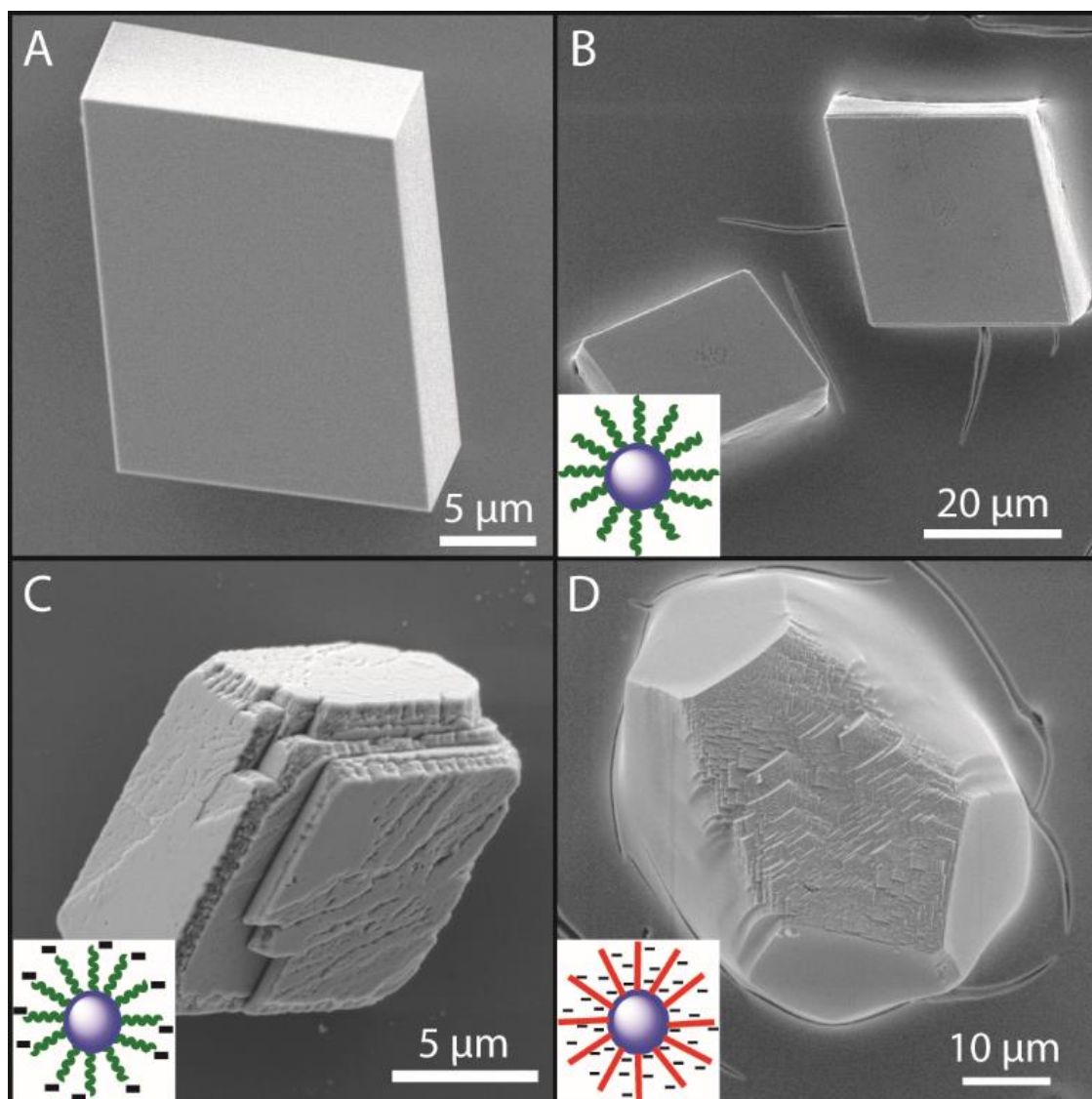


**Figure 2.2** Representative scanning electron microscopy (SEM) images of calcite grown ex situ at 20 °C with the three types of nanoparticles used in this study (see main text for further details). (A) Control calcite crystal prepared in the absence of any nanoparticles. (B) Representative crystals grown in the presence of non-ionic Ph-PGMA-PBzMA nanoparticles. (C) Representative crystal grown in the presence of anionic HOOC-PGMA-PBzMA nanoparticles. (D) Representative crystal grown in the

presence of PMAA-PBzMA nanoparticles. In each case the ammonia diffusion method was utilized at pH 8 using 5 mM CaCl<sub>2</sub> and a copolymer nanoparticle concentration of 0.75 wt%.

The most common method to examine the effect of nanoparticles on calcite formation is to grow bulk *ex situ* crystals in aqueous solution in their presence, as reported in various studies.<sup>5,23,25</sup> In control experiments performed in the absence of any nanoparticles, rhombohedral crystals with clean, smooth {104} facets are formed (Fig. 2A). Crystals grown in the presence of non-ionic Ph-PGMA-PBzMA nanoparticles remain rhombohedral, as expected (Fig. 2B). However, if anionic nanoparticles are present during calcite formation, the crystal morphology is affected. Calcite rhombohedra grown in the presence of HOOC-PGMA-PBzMA nanoparticles have blunted edges and much rougher {104} facets, suggesting some weak interactions between these nanoparticles and growing crystal (Fig. 2C). The presence of PMAA-PBzMA nanoparticles has a much more dramatic impact on the crystal morphology (Fig. 2D). The {104} facets are retained as endcaps, but crystals become rounded and extended into bullet-like shapes, indicating a very strong interaction between such nanoparticles and the crystal lattice. Previous *ex situ* growth studies have shown that such a drastic change in morphology often correlates with significant incorporation<sup>5,20,37-39</sup>. Although these images provide a useful initial guide, direct observation at much shorter length scales via *in situ* AFM is required to appreciate the true nature of the nanoparticle-crystal interaction.

#### 2.3.4 *In situ* AFM

To conduct *in situ* AFM studies, growth solution is flowed over the surface of a freshly-cleaved single crystal of calcite using a fluid cell containing the AFM tip.<sup>40,41</sup> Under carefully controlled conditions corresponding to relatively low supersaturation (supersaturation  $\sigma$  is defined in Equation 1, where  $AP$  is the activity product and  $K_{sp}$  is the equilibrium solubility product), calcite only grows via addition of  $\text{CaCO}_3$  growth units to hillocks, which are sources for atomic steps originating from screw dislocations within the crystal.<sup>40-42</sup>

$$\sigma = \ln\left(\frac{AP}{K_{sp}}\right) \quad \text{Equation (2.1)}$$

Observing *in situ* growth via this mechanism allows direct observation of nanoparticle-crystal interactions at conditions close to those found in nature (ambient, room temperature, and a low degree of supersaturation). Based on previous AFM literature and classical crystal growth theories, we anticipated three possible interactions for nanoparticles with a growing calcite crystal.<sup>8,12,42</sup> These are: (i) attaching and then detaching from the surface, (ii) attaching and becoming incorporated into the crystal, as reported by Cho et al.<sup>13</sup> and (iii) an intermediate scenario where a nanoparticle “hovers” on the calcite surface, while steps continue to flow beneath it.<sup>12</sup> It is hypothesized that all three interactions can occur to some degree. However, the specific nanoparticle surface chemistry is expected to determine the major interaction for a given nanoparticle type. With sufficient data, we can

analyze the behavior of an ensemble of particles to compare the effects of varied charge coronas on the particle-crystal interaction.

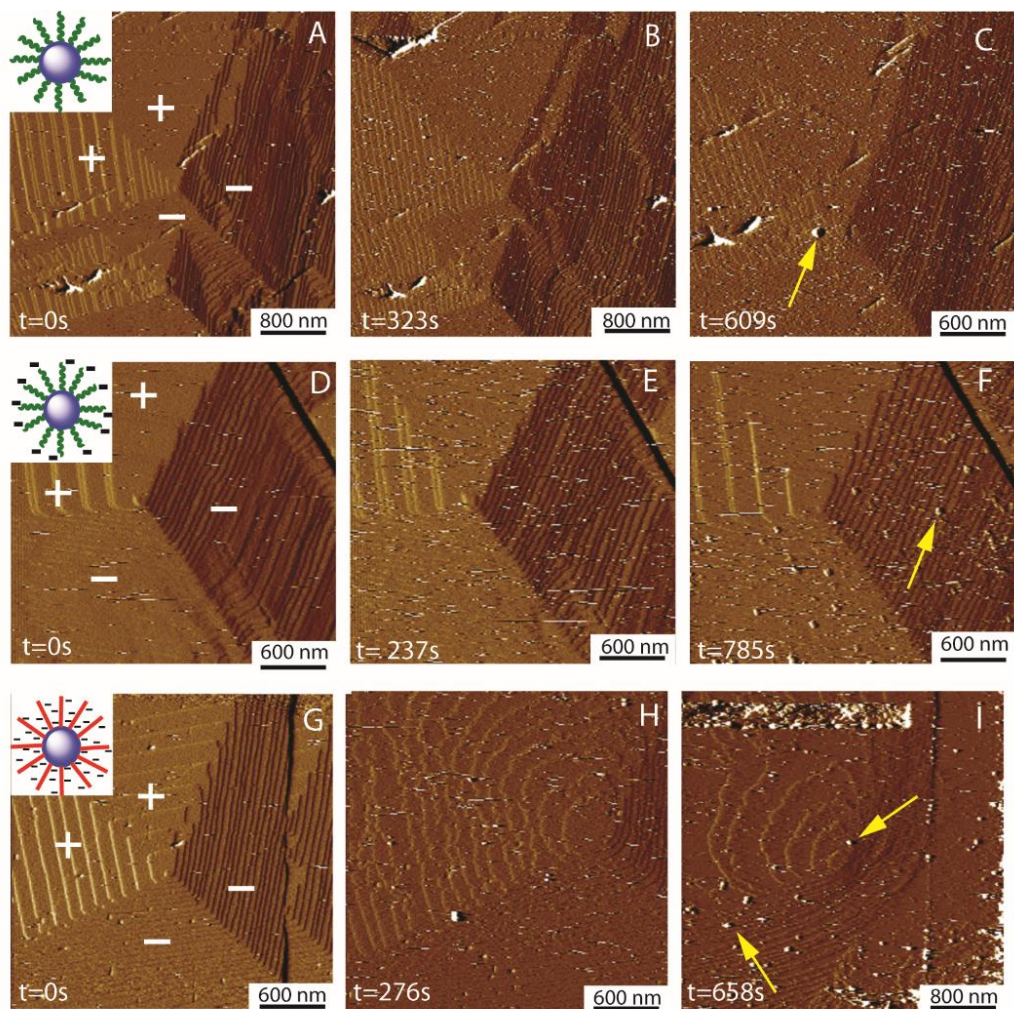


**Figure 2.3** Time-resolved in situ AFM studies of calcite growth in the presence of three types of sterically-stabilized diblock copolymer nanoparticles ( $\sigma = 1.15$ , nanoparticle concentration = .00075% wt). Zero time ( $t = 0$ ) refers to when the nanoparticle-containing growth solution is first added to the AFM cell. A-C: growth in the presence of non-ionic Ph-PGMA-PBzMA nanoparticles. D-F: growth in the presence of weakly anionic HOOC-PGMA-PBzMA nanoparticles. G-I: growth in the presence of strongly anionic PMAA-PBzMA nanoparticles. The (+) and (-) define the

obtuse and acute facets of the growing calcite hillock, respectively. Movies S1-S3 available online depict a more complete series of images. Images are deflection (color scale  $\pm 20$  mV) taken in contact mode.

Calcite growth studies using *in situ* AFM allows direct observation of the nanoparticle-crystal interactions. A typical series of images from these time-resolved experiments is shown in Figure 3A-3C (non-ionic Ph-PGMA-PBzMA nanoparticles), 3D-3F (weakly anionic HOOC-PGMA-PBzMA nanoparticles), and 3G-3I (strongly anionic PMAA-PBzMA nanoparticles) (Movies S1-S3). First, a control growth hillock is formed in the absence of any nanoparticles (Figs. 3A, 3D, 3G). Once such a hillock is identified, the growth solution is switched to one of identical composition, ionic strength and pH that contains nanoparticles. Then the nanoparticle-crystal interactions can be directly imaged under growth conditions. The Ph-PGMA-PBzMA nanoparticles (Figs. 3A-3C) have negligible effect on the growing hillock and minimally interact with the calcite surface, although they are most likely present very near to the calcite-solution interface (note the increased noise in Figs. 3B-3C). Such observations are fully consistent with the unmodified bulk calcite crystal shown in Figure 2B. The HOOC-PGMA-PBzMA nanoparticles bind to the acute facets of the growing hillock (Figs. 3E and 3F) but do not seem to modify this feature, which is similar to the minimal changes observed for the bulk calcite crystal in Figure 2C. In striking contrast, the strongly anionic PMAA-PBzMA nanoparticles initially cause roughening of both the obtuse and acute steps, leading to hillock rounding (Fig. 3H).

This hillock modification is consistent with the morphology of the bulk calcite crystals (Fig. 2D). Subsequently, the hillock becomes heavily decorated by nanoparticles on the acute facets (Fig. 3I). The selected stills provide a useful summary, but understanding the nanoparticle-calcite interaction mechanism(s) in more detail requires higher resolution images.

### 2.3.5 Nanoparticle-Crystal Interactions

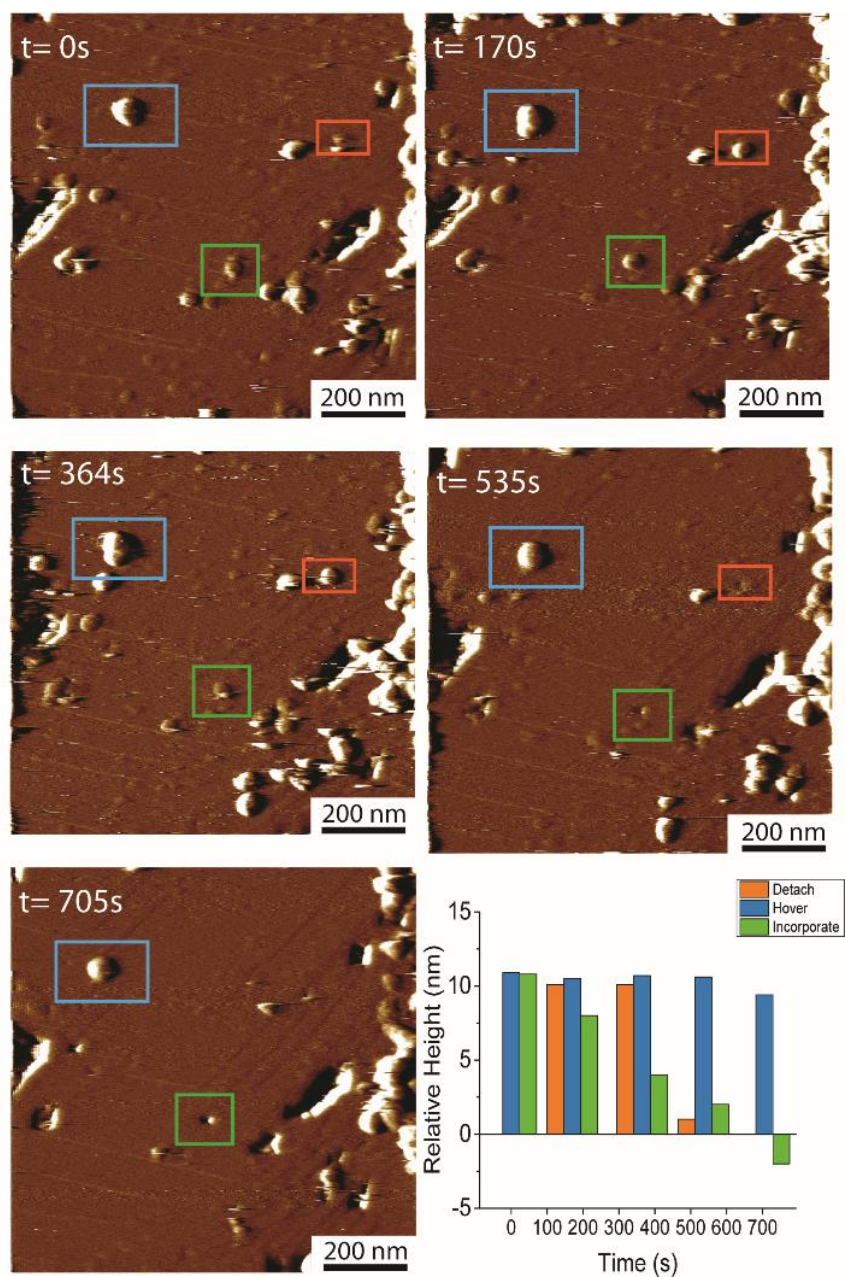


**Figure 2.4** High resolution in situ AFM images of the highly anionic PMAA-PBzMA nanoparticles interacting with a growing calcite face at  $\sigma = 1.15$ . The height measurements in the bottom right are from line scan measurements of the highlighted nanoparticles. Over time, three types of behavior can be observed, although the

highlighted nanoparticles start at similar relative height. The orange nanoparticle attaches between the first and second image, then detaches between the third and fourth image. There is a gradual reduction in the height of the green nanoparticle until it is apparently incorporated within the crystal. The blue nanoparticle “hovers” on the surface, staying attached but not becoming incorporated within the crystal. This Figure is also available as Movie S4.

Imaging the nanoparticle-crystal interactions at higher resolution reveals three types of behavior, as anticipated (Fig. 4): (i) after initial attachment, the nanoparticle immediately detaches again from the surface (orange box); (ii) the nanoparticle attaches to the surface and there is a progressive reduction in its apparent height as it becomes incorporated within the crystal (green box), producing a small cavity similar to those reported by Cho et al.<sup>13</sup>; (iii) the nanoparticle attaches to the calcite surface and “hovers” above it without changing its height significantly until either it becomes detached or is eventually occluded (blue box). Close inspection of the image series shown in Fig. 4 confirms multiple examples of these three modes of interaction. Sampling large populations of nanoparticles is required to quantify the relative contribution made by each mode for the three types of nanoparticles studied herein.

By tracking individual nanoparticle heights over time, we can build up a better understanding of their behavior and hence reveal the relative contributions made by each of the three modes of interactions (Figure 5A; see Supplementary Figures S4 and S5 for plots of individual nanoparticle behavior). Qualitatively, more PMAA-PBzMA

than HOOC-PGMA-PBzMA particles bind to the calcite surface within an equivalent amount of time. Tracking nanoparticle height as a function of time reveals that the strongly anionic PMAA-PBzMA and weakly anionic HOOC-PGMA-PBzMA nanoparticles appear to become incorporated within calcite at approximately the same rate, implying a similar incorporation mechanism for both types of nanoparticles (Figs. S4 and S5). A summary of the three modes of interactions reveals that a similar fraction of both types of nanoparticles are incorporated (40-45% of population), whereas the fraction of particles that hover and detach vary significantly between the two types. For the PMAA-PBzMA nanoparticles, ~40% hover while only ~15% become detached. Conversely, ~10% of the HOOC-PGMA-PBzMA nanoparticles hover while >50% detach (Fig. 5A). When the nanoparticles are sorted with respect to which type of interaction they undergo as a function of time, it becomes evident that most of the PMAA-PBzMA nanoparticles either begin incorporating into the calcite lattice or detach immediately (Figs. 5B and S7). Furthermore, it appears that nanoparticles that bind to the surface in later images are much more likely to “hover”.

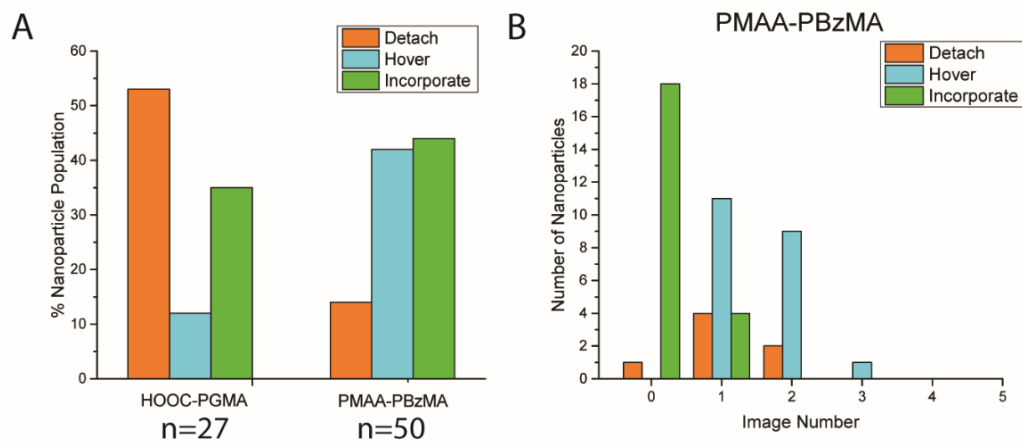


**Figure 2.5** Comparison of the three modes of interaction of HOOC-PGMA-PBzMA and PMAA-PBzMA nanoparticles with calcite as determined by in situ AFM studies. (A) Histograms showing the relative proportion of each nanoparticle population to exhibit either detachment, hovering or incorporation. (n=50 for PMAA-PBzMA and n=27 for HOOC-PGMA) (B) Histograms showing the number of nanoparticles each of the three types of behavior for PMAA-PBzMA nanoparticles over time. The image number refers to the last image obtained before a significant (>10%) height reduction is observed. A comparable histogram obtained for HOOC-PGMA-PBzMA nanoparticles is shown in Fig. S7 (albeit for fewer nanoparticles). See Methods section for further details on image analysis and nanoparticle selection.

## 2.4 Discussion

The nature of the steric stabilizer chains (and resulting anionic charge density of the nanoparticles) clearly dictate nanoparticle-crystal interactions. Thus, the non-ionic Ph-PGMA-PBzMA nanoparticles have essentially no interaction with growing calcite. The weakly anionic HOOC-PGMA-PBzMA nanoparticles only slightly

modify bulk calcite crystals but still interact strongly enough for any given nanoparticle to potentially participate in one of the three modes of interaction. The strongly anionic PMAA-PBzMA nanoparticles attach in much greater numbers to the calcite surface but still exhibit each of the three modes of interaction. The *in situ* AFM data shown in Figure 5 lead to the following three important questions regarding the nature of the nanoparticle-crystal interaction. (1) How does the variation in coronal charge density affect initial nanoparticle binding to the surface? (2) Why do only the PMAA-PBzMA nanoparticles “hover” in large numbers? (3) Why do nanoparticles that eventually bind later tend to “hover” rather than become incorporated directly?

#### *2.4.1 Charge Corona Effect on Particles in Solution*

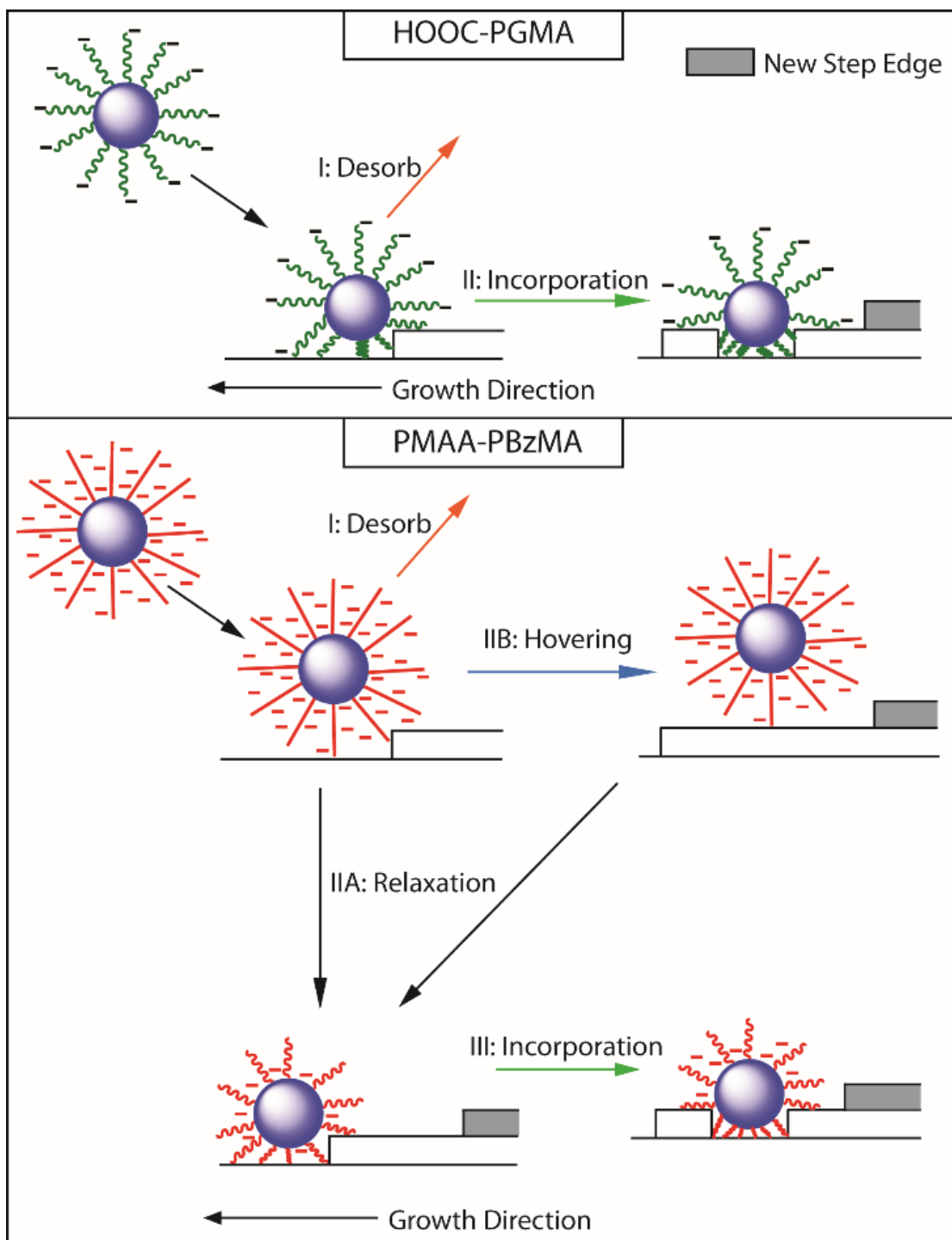
We cannot properly analyze nanoparticle-crystal interactions without first considering the chemical structure of the nanoparticles in the growth solution. Both Ph-PGMA-PBzMA and HOOC-PGMA-PBzMA possess flexible stabilizer chains with either zero or relatively low charge density. In contrast, PMAA should act as a polyelectrolyte brush because of its highly anionic nature at pH 8.<sup>35,36</sup> When immersed in a solution at a pH above its  $pK_a$ , a PMAA brush becomes swollen and extended due to deprotonation, resulting in coulombic repulsion between the highly anionic chains.<sup>35</sup> In Figure 1, DLS studies indicate that the mean diameter of the PMAA-PBzMA nanoparticles substantially increases on switching from below pH 4 (25 nm) to pH 8 (45 nm). Similar pH-dependent behavior has been observed for PMAA brushes.<sup>35</sup> Such polyelectrolyte brushes are known to be strongly affected by ionic strength, and can become swollen with increasing salt concentration.<sup>35,36</sup> Such

swelling is an osmotic effect driven by cation binding to the PMAA chains, since this generates an osmotic pressure via a net increase in charge density.<sup>35</sup> However, the PMAA chains eventually become saturated with ions and collapse (the so-called “salted brush” regime).<sup>35</sup> Therefore, PMAA stabilizer chains should become highly extended in calcite growth solution (1.8 mM  $\text{Ca}^{2+}$  and 36 mM  $\text{Na}^+$  ions at pH 8). In contrast, the HOOC-PGMA chains are not polyelectrolytes and thus do not exhibit such swelling behavior.

#### 2.4.2 A Model for Nanoparticles Interacting with a Growing Crystal

The observations made in these *in situ* AFM experiments combined with previous studies of peptides on calcium carbonate and oxalate lead us to present a model that describes the likely interactions of nanoparticles (or nanoscale additives) with growing crystals in the low supersaturation regime. This model is depicted in Scheme 2: the nanoparticle first binds to the surface via electrostatic interactions between the anionic carboxylate groups and the cationic  $\text{Ca}^{2+}$  ions in the crystal lattice. On attachment, relatively fast nanoparticle diffusion occurs to the step edges in most cases or if the particles happen to attach at a step edge, they need not diffuse. The concept of step edge diffusion is based on the experiments conducted by Cho et al., who clearly demonstrated that nanoparticles are bound almost exclusively to the step edges under equilibrium conditions, thus suggesting relatively fast surface diffusion, at least initially.<sup>13</sup> Once the nanoparticle becomes strongly bound to the surface, its diffusion becomes hindered by the ionic bond(s) between the charged group(s) and the surface. Subsequently, the bound nanoparticle adopts either a swollen or a collapsed

state. Weaver et al.<sup>43</sup> showed that similar binding behavior for peptides is best explained by invoking multistep time-dependent adsorption to the growing crystal surface. This concept is analogous to the brush-like PMAA stabilizer chains becoming “salted out” and collapsing. In their swollen, extended state such anionic chains are extended, so the  $\text{Ca}^{2+}$  and  $\text{CO}_3^{2-}$  ions can still access the step edge; this binding configuration allows the step to propagate under the pinned nanoparticle, which “hovers” on the surface. However, if the PMAA chains are instead “salted out” then the nanoparticle collapses and access to the step edge is blocked. Thus the step grows around the pinned nanoparticle, leading eventually to its incorporation within the crystal. Swollen nanoparticles can also subsequently collapse, hence “hovering” nanoparticles can also eventually become occluded. The PMAA-PBzMA nanoparticles have a much greater tendency (Fig. 5A) to become swollen and “hover”, with the anionic character of the PMAA chains being the most likely reason for such behavior. This study has provided new insights into nanoparticle-crystal interactions in real time on the nm length scale; our observations should inform the design of next-generation organic nanoparticles that enable the extent of occlusion within host crystals to be maximized.



**Scheme 2.2** Schematic representation of the possible modes of interaction of two types of anionic nanoparticles interacting with a growing calcite surface. On contact

with the surface, the nanoparticles first undergo fast diffusion to become bound at a step edge. Subsequent relaxation of the copolymer chains determines to what extent the growth species ( $\text{Ca}^{2+}$  and  $\text{CO}_3^{2-}$  ions) can access binding sites on the step edge. Hence the nanoparticle either (I) detaches or (II) continues to interact with the surface by “hovering”. For the highly anionic PMAA-PBzMA nanoparticles, the copolymer chains can either (IIB) remain rigid (slow relaxation) to allow access of growth ions to the step edge or (IIA) relax quickly, thus blocking growth species. For the HOOC-PGMA stabilizer chains, faster relaxation (II) blocks growth ions from diffusing to the step edge. When such mass transport is blocked, the pinned nanoparticle becomes occluded as the step grows around it.

#### *2.4.3 Initial Binding Process: Importance of the charge corona*

On adding the strongly anionic PMAA-PBzMA nanoparticles to the growing calcite crystal, *in situ* AFM studies reveal a substantial change in the hillock morphology (including roughening of the step edges) before these nanoparticles are observed at the surface (Fig. 3H). Similar local roughening is common for small molecules interacting with calcite, so the roughening we observe is possibly due to attachment of unbound polymer, osmotically driven out of the micelle in an equilibrium process<sup>44</sup>. Any free polymer will bind tightly to the step edge due to the PMAA block, so even a very low concentration of free polymer could cause a change in hillock morphology<sup>5</sup>. It is also possible that there is some contamination from free PMAA homopolymer, which could also cause hillock rounding. In either case, the smaller size of the free polymer, as compared to the nanoparticles, would allow for

faster diffusion to the growing crystal surface. The step roughening should also enhance initial nanoparticle attachment to the surface by generating more kink sites (high energy binding sites) on the step edges<sup>42</sup>. The weakly anionic HOOC-PGMA-PBzMA nanoparticles behave very differently. First, although attachment of some smaller units occurs at the acute step edges (Figure 3E), much less severe hillock modification is observed prior to nanoparticle attachment. Also, the nanoparticles do not appear to attach as strongly or to the same extent. With the non-ionic PGMA-PBzMA nanoparticles, there is no hillock modification over a comparable time scale (Fig. 3B), and step progression is clearly observed with no change in morphology or nanoparticle attachment (Supplementary Fig. S3).

Once the nanoparticles interact with the calcite surface, Figure 5A illustrates the strikingly different behavior for the two types of anionic nanoparticles. For the HOOC-PGMA-PBzMA nanoparticles, there is only a single terminal anionic carboxylate group per chain, so crystal binding is relatively weak and the nanoparticles tend to either immediately detach or become incorporated. In contrast, the PMAA-PBzMA nanoparticles can bind more strongly and access a much greater number of binding states as a result of the cooperativity conferred by the highly anionic PMAA chains. Therefore, for any given PMAA-PBzMA nanoparticle attachment, subsequent “hovering” or incorporation within the growing crystal lattice is much more favorable. This behavior is reflected in the quantitative data shown in Figs. 5B and S7: a much greater number of PMAA nanoparticles are observed at the calcite surface. Our *in situ* data are consistent with earlier (albeit more qualitative) *ex situ* data; determination of zeta potential alone is not sufficient to predict efficient

occlusion. Instead, the precise nature of the nanoparticles and their surface charge density must be considered<sup>23,24,29</sup>.

The nature of the stabilizer chains accounts for the observed interactions. When a nanoparticle initially attaches to the surface, it either remains adsorbed or subsequently becomes detached. If it stays bound, the long stabilizer chains must undergo relaxation to satisfy the local charge balance. For the HOOC-PGMA-PBzMA nanoparticles, such relaxation is likely to be fast, since the stabilizer chains only possess a single terminal anionic charge and the chains never adopt a stretched conformation. The PMAA-PBzMA nanoparticles most likely have more extended stabilizer chains so relaxation is more complex, possibly involving both fast and slow relaxation modes. For highly swollen PMAA-PBzMA nanoparticles with extended stabilizer chains, relaxation is likely to be relatively slow. Such extended chains are likely to be highly permeable to neighboring ions, making it easier for the crystal to grow beneath attached nanoparticles. “Hovering” occurs when such nanoparticles remain at the calcite surface in their swollen state for some time prior to ion-induced collapse. PMAA-PBzMA nanoparticles are more likely to display this hovering behavior because they are more prone to undergo slower relaxation. For either type of nanoparticle, once the stabilizer chains relax at the surface, the step edge is forced to grow around the nanoparticle, leading to its incorporation within the crystal lattice.

#### 2.4.4 Particles binding later hover: Effect of free polymer in solution

A surprising feature of the two histograms shown in Figure 5 is that most of the nanoparticles that bind later remain in their swollen state and “hover.” Though they may subsequently become incorporated, the concept of a time-dependent distribution of nanoparticles between these two states is surprising because such experiments usually assume a steady state has been attained, not least because the inflowing solution supplies a constant concentration of nanoparticles and growth units (i.e.,  $\text{Ca}^{2+}$  and  $\text{CO}_3^{2-}$  ions) for the crystal. However, the assumption of a steady state ignores the potential effect of free (co)polymer chains in solution, rather than existing in the form of nanoparticles. In principle, there is a micelle-unimer equilibrium for these diblock copolymer nanoparticles, with a background concentration of individual copolymer chains (unimers)<sup>44</sup>. Given that the PMAA-PBzMA diblock copolymer is highly anionic, its free chains most likely behave as molecular additives, binding to the step edge and hindering crystal growth. Such behavior might account for the substantial changes in hillock morphology observed for PMAA-PBzMA nanoparticles. In addition, if the hydrophobic core-forming PBzMA block is sufficiently large to prevent incorporation, the build-up of copolymer at the surface and particularly at step edges would provide an additional barrier to nanoparticles entering the collapsed state on the surface. This behavior would increase the relative fraction of particles in the hovering state, thus explaining the apparent time dependence for both types of nanoparticles. In principle, an increase in “hovering” over time could also be induced by the AFM tip interacting with nanoparticles under continuous imaging. In view of this possible imaging artifact, we ceased imaging for a few minutes between each

series of images prior to resuming AFM studies. This precaution had no effect on our observations.

## **2.5 Conclusions**

Charge density and surface chemistry are critical factors for determining nanoparticle-crystal interactions during crystal growth, including efficient nanoparticle occlusion. Previous work has shown that atoms must be comparable in size to  $\text{Ca}^{2+}$  to substitute into the ionic crystal, small molecules require negatively-charged functional groups, and nanoparticles must have highly anionic coronas in order to become incorporated within calcite. In the latter case, the number of anionic (e.g., carboxylate) groups per chain is a key factor in governing the nanoparticle-crystal interaction. The *in situ* AFM studies detailed in this report provide the first observation of “hovering” behavior for nanoparticles; this phenomenon has previously only been reported for peptides on growing calcium oxalate monohydrate crystals. We suggest that such “hovering” is one of three possible modes of interactions that appropriate nanoparticles may have with a growing crystal. The other two interactions are either simply surface attachment and detachment or attachment followed by immediate occlusion. Furthermore, for a highly anionic nanoparticle collapse of its steric stabilizer chains is the primary factor in determining its surface interaction, such that faster collapse enables its incorporation to proceed rapidly. Additionally, there is some evidence that free (co)polymer chains may modify the crystal surface, demonstrating that appropriate care must be taken to account for all the species likely to be present in the aqueous solution. This study can inform the design of next-generation

nanoparticles for even more efficient occlusion within calcite. For example, tuning solution chemistry to promote collapse of the electrolyte corona could be used to control the amount of nanoparticle incorporation. Going forward, consideration of the interaction of nanoparticles with the surface hydration layer of calcite and other crystals can also help to fine-tune incorporation amounts.<sup>45,46</sup> Furthermore, our model for nanoparticle-crystal interactions is likely to be applicable to other host crystals, leading to the ability to custom design single crystal composites that pair disparate materials within a single structure.

## ***2.6 Materials and Methods***

### *2.6.1 Particle Synthesis*

The synthesis of PGMA and PMAA macro-CTAs via RAFT solution polymerization has been described in detail elsewhere<sup>25,28</sup>. The synthesis of similar PBzMA-core nanoparticles via RAFT emulsion polymerization was recently reported by Armes and co-workers<sup>47</sup>.

### *2.6.2 Dynamic light scattering and Zeta Potential*

Dynamic light scattering (DLS) and zeta potential measurements were performed at 25°C using a Zetasizer Nano-ZS instrument (Malvern Instruments, UK) at a fixed scattering angle of 173° using Dispersion Technology Software version 6.20.

Copolymer dispersions were diluted in 1 mM KCl. Aqueous dispersions were adjusted to pH 9 using KOH and titrated to approximately pH 3 with HCl.

### *2.6.3 TEM*

Transmission electron microscopy (TEM) studies were conducted using a Philips CM 100 instrument operating at 100 kV and equipped with a Gatan 1 k CCD camera. Diluted nanoparticle dispersions (~0.10 % w/w) were dried on freshly glow-discharged carbon-coated copper/palladium grids (Agar Scientific, UK) and subsequently exposed to 0.75 w/v % uranyl formate solution for 30 s at 20°C prior to analysis.

#### *2.6.4 Ex Situ “Bulk” Calcite Growth*

Crystals were grown in a desiccator via the classical ammonia diffusion method<sup>48</sup>. All samples were 10 mL in total volume and used 5 mM CaCl<sub>2</sub> solution in Petri dishes. Crystals were grown on glass cover slips, which had been sonicated for 5 min each in DI water (18.6 MΩ) and ethanol to remove any surface contamination before being placed in the growth solution. The nanoparticle dispersions (15 wt%) were used neat in 0.5 mL aliquots for each sample. Crystals were allowed to grow in the desiccator saturated with ammonium carbonate for two days. Then the glass slides containing the calcite crystals were removed and dried with N<sub>2</sub> gas. The slides were then mounted on aluminum SEM imaging stubs and coated with ~100 nm of conductive carbon before being imaged using a Tescan MIRA3 FE-SEM.

#### *2.6.5 In Situ AFM Experiments*

Imaging experiments were performed using a Multimode AFM with a Nanoscope III Controller (Digital Instruments) using the method reported by Cho et. al<sup>13</sup>. Solutions were prepared by adding 5 μL of 15 wt% nanoparticle dispersion (final copolymer concentration = 5 μM) to premade aqueous solutions of CaCl<sub>2</sub> (1.8 mM) and NaCl

(39.4 mM). For imaging, geologic calcite (Iceland Spar, Ward's Scientific) was glued with epoxy to the steel AFM sample disk with a freshly-cleaved {104} face for imaging. Using a commercial fluid cell (MTFML, Bruker Nano) and a syringe pump to control fluid flow, growth solution was flowed through the cell at 20°C at a typical rate of 0.30 mL/min. Imaging was performed using Bruker Nano DNP-S model cantilevers with a nominal radius of curvature for the tip of less than 10 nm. Images of the calcite surface were recorded in either contact mode (primarily) or tapping mode using scan rates of ~3 Hz and typically 256 lines per image. The key to imaging the nanoparticles was minimizing the force applied by the tip, otherwise unacceptable levels of nanoparticle displacement were observed. Even in the best case scenario, there was clear (but consistent) movement of the nanoparticles by the tip towards the edges of the image. However, in the minimal force case, this tip effect was consistent and reproducible (see Supplementary Information and Fig. S6). Detailed imaging areas were typically 1x1, 3x3, or 5x5  $\mu\text{m}$ . For consistent image sequences, images were always taken in the up direction. For imaging the anionic nanoparticles adsorbed onto mica, the mica was freshly cleaved and treated with poly(L-Lysine) to ensure its surface charge reversal and hence promote nanoparticle binding to the surface.

#### *2.6.6 AFM Image Analysis*

Images were analyzed using Nanoscope Analysis software. Nanoparticles were selected for inclusion in statistics only if their initial height was between 9 and 20 nm (so as to minimize the unwanted inclusion of any nanoparticle aggregates) and there were no other nanoparticles within 50 nm of the measured particle. Heights were

determined through individual line scans across at least six images (or until the nanoparticle either detached or became fully incorporated). All nanoparticles were tracked by hand to ensure there was no double counting. Residency time on the surface was determined by taking the time at the last image before the nanoparticle changed significantly in height. Qualification for the designation of “hovering” required less than 10% variation in the observed nanoparticle height for at least three consecutive images (~5 minutes real time. For the PMAA-PBzMA nanoparticles, three different experiments were conducted to analyze 50 nanoparticles. For the HOOC-PGMA-PBzMA nanoparticles, two separate experiments yielded a total of 27 nanoparticles for analysis.

## ***2.7 Acknowledgements***

This work was funded by a joint National Science Foundation (NSF) and EPSRC Materials World Network (MWN) grant (DMR 1210304 and EP/J018589/1). This work made use of the Cornell Center for Materials Research Shared Facilities which are supported through the NSF MRSEC program (DMR-1120296). We thank the Wiesner group at Cornell for the shared use of their AFM. SPA acknowledges a five-year ERC Advanced Investigator grant (PISA 320372) and EPSRC support.

## ***2.8 Supporting Information***

### ***2.8.1 Tip Effects***

AFM tip effects were minimized in a similar manner to previous *in situ* AFM studies of calcite<sup>1</sup>. However, the diblock copolymer nanoparticles used in this work are inherently elastic. Thus they are particularly sensitive to the tip scanning the

surface. Some of the nanoparticles are inevitably pushed to the exterior of the imaging area, as shown in Supplementary Information Figure S6. This effect is mitigated by minimizing the force that the tip applies to the surface. However, the nanoparticles are nevertheless still perturbed by the tip (Fig. S6). Additionally, it was observed that some of the “hovering” nanoparticles subsequently detached or became incorporated into the calcite crystal. In principle, it is possible that the “hover and detach” process is purely an artifact of the imaging. In practice, it is more likely that some fraction of the “hovering” nanoparticles are not able to attain their collapsed (adsorbed) state and do subsequently detach. However, we cannot deconvolute the artifact from what may be happening elsewhere on the surface and therefore we present the “hovering” data as a separate category. It is likely that tip scanning reduces the number of binding events per image with increasing image number as compared to a pristine (un-imaged) area of the crystal face. Again, this perturbation should equally affect the different nanoparticles; we are confident that we have accurately captured a population of nanoparticles and their behavior, but the effect must be considered in the analysis of the nanoparticle dynamics.

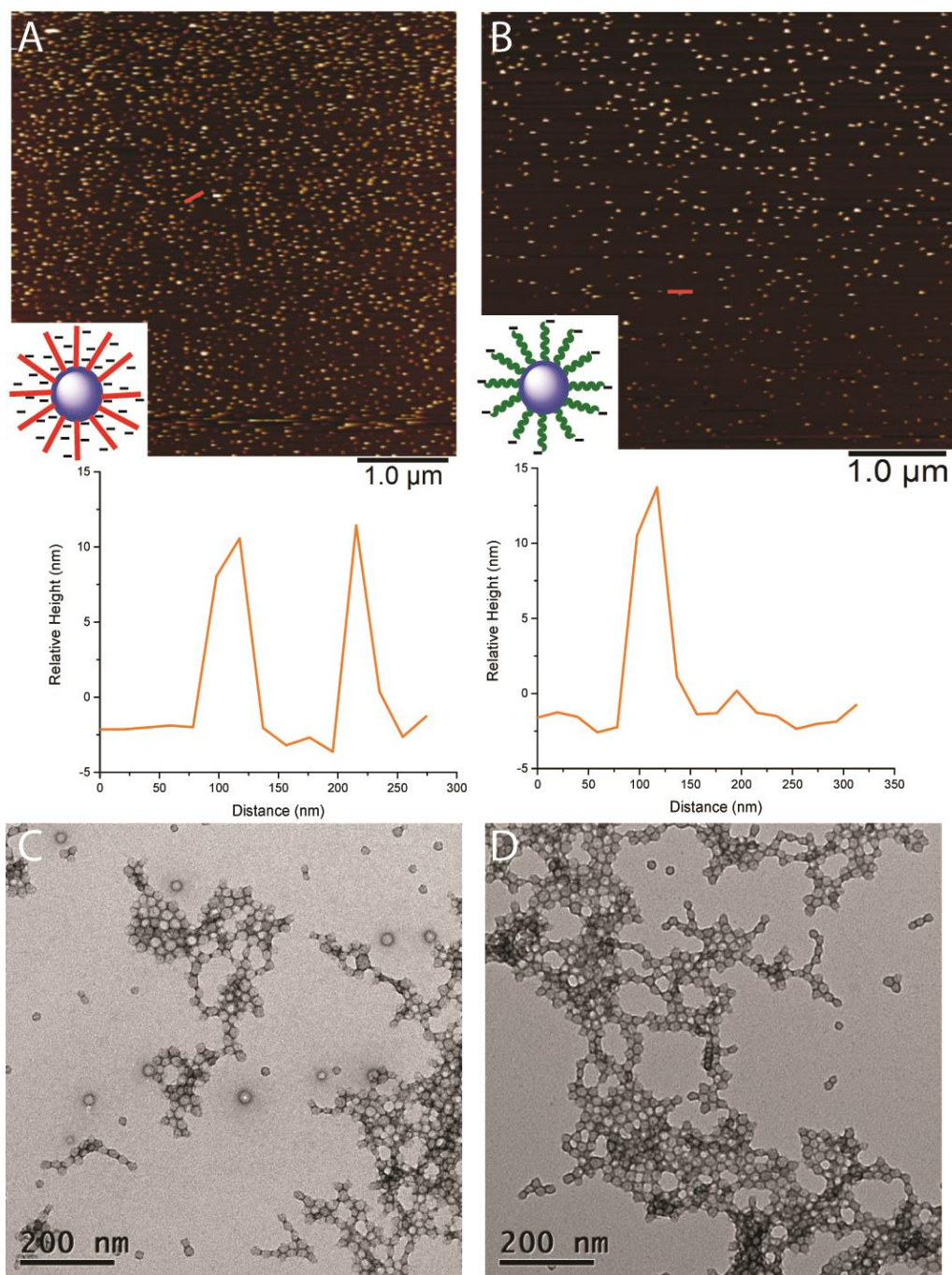


**Figure 2.6(S1).** Tapping mode AFM images, line scans and transmission electron micrographs (TEM) of (A, C) PMAA-PBzMA and (B, D) HOOC-PGMA-PBzMA nanoparticles. AFM images of the nanoparticles absorbed onto poly(lysine)-treated mica were obtained in deionized water. TEM images were obtained by drying a dilute

dispersion of nanoparticles onto a carbon-coated TEM grid before staining with uranyl formate. According to TEM (17.1 nm average) and AFM studies (15.2 nm average), the PMAA-PBzMA (A, C) and HOOC-PGMA-PBzMA (B, D) nanoparticles are very similar in size (~12 nm).

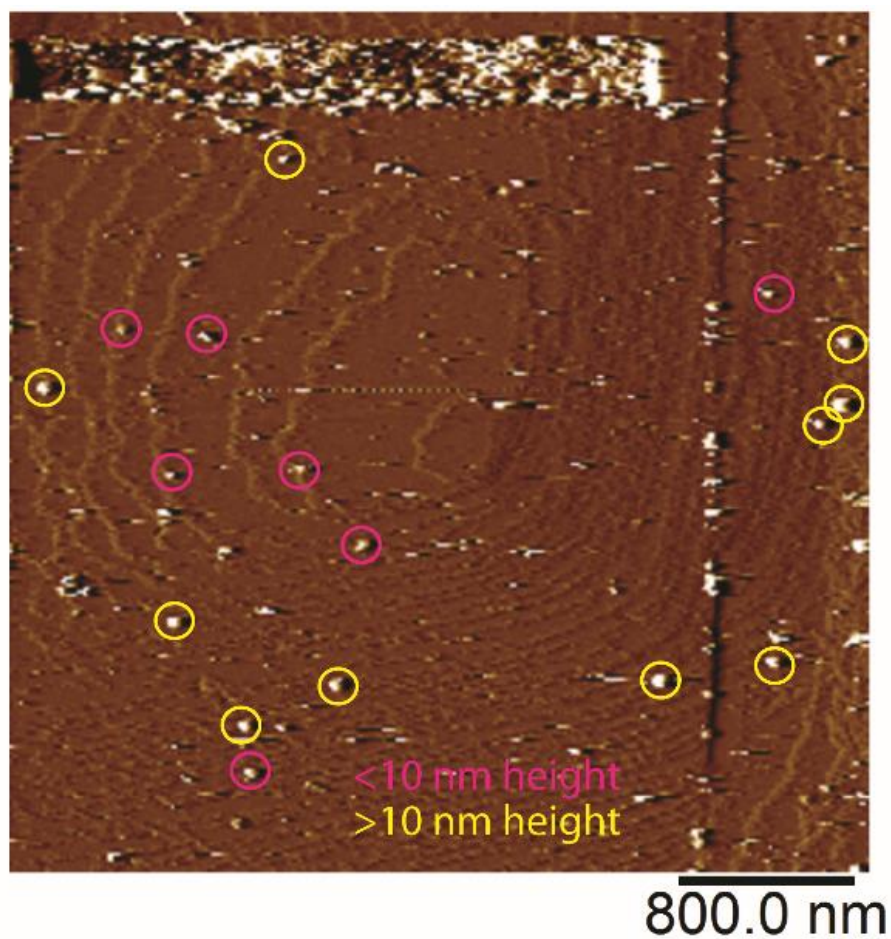


**Figure 2.7(S2).** A typical *in situ* AFM image used to track nanoparticle interactions (PMAA-PBzMA) with the surface of a calcite crystal. Yellow circles highlight the

nanoparticles which meet the requirements for further tracking and analysis.

Nanoparticles indicated by pink circles do not qualify for tracking because they have already begun to be incorporated. Each nanoparticle indicated by a yellow circle has had its height tracked and recorded and is included in the larger data set.

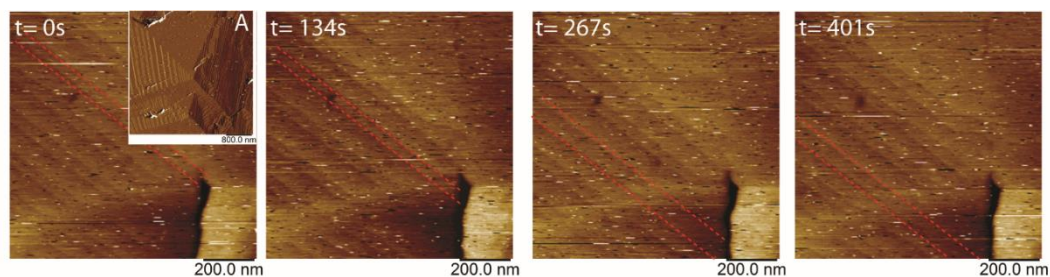


**Figure 2.8(S3).** Time series of *in situ* AFM images during calcite step growth in the presence of uncharged Ph-PGMA-PBzMA nanoparticles. Inset (A) shows a control hillock before addition of these nanoparticles. The steps clearly move unhindered with no nanoparticle attachment despite their presence in solution near the crystal surface (as indicated by the greater noise and streaking in images).

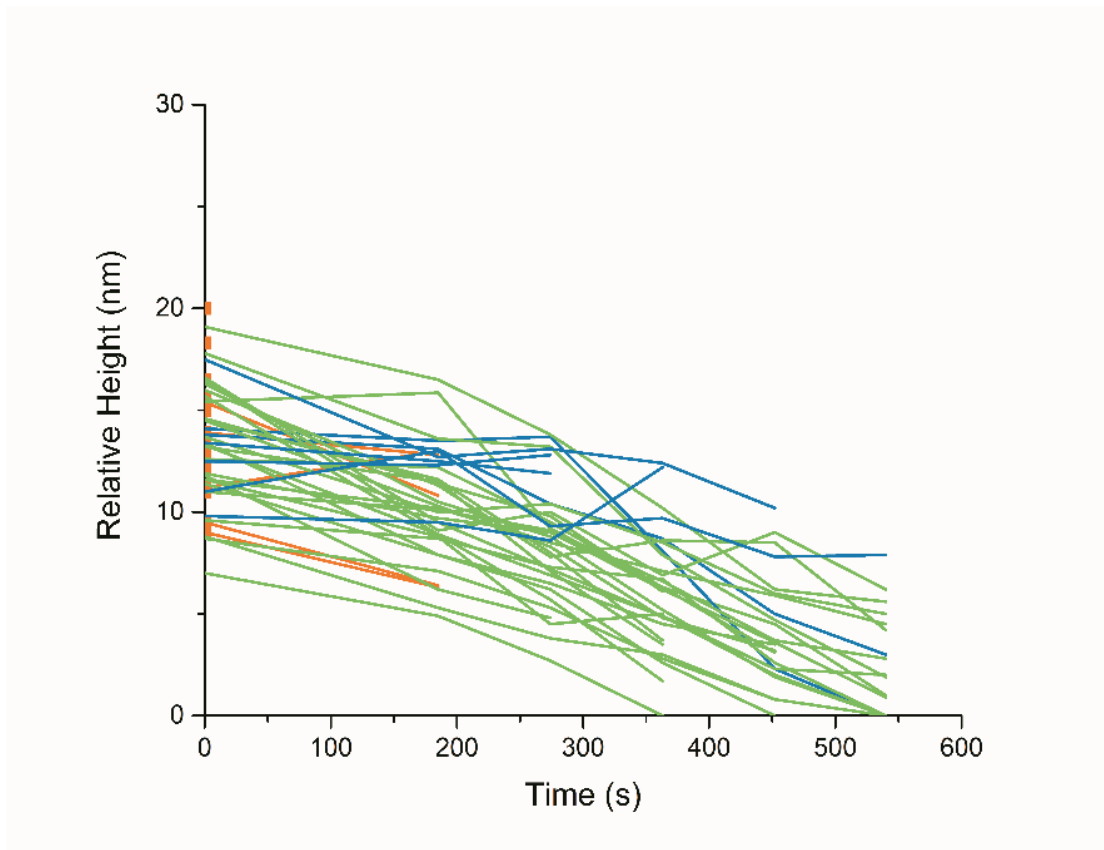


**Figure 2.9(S4).** Relative nanoparticle height over time for a single *in situ* AFM image series of HOOC-PGMA-PBzMA nanoparticles on the surface of a calcite crystal. Each line corresponds to an individual nanoparticle tracked across multiple AFM images. Three types of nanoparticle behavior were observed; (i) immediate detachment from the surface within one image (orange lines,  $n = 17$ ), (ii) hovering on the surface before either detachment or incorporation (blue lines,  $n = 6$ ), and (iii) incorporation directly into the crystal (green lines,  $n = 27$ ). The distribution of hovering nanoparticles between later detachment and incorporation is likely to be strongly affected by the

AFM tip and is therefore not studied in further detail. Nanoparticles that are directly incorporated into the calcite appear to do so at similar rates.

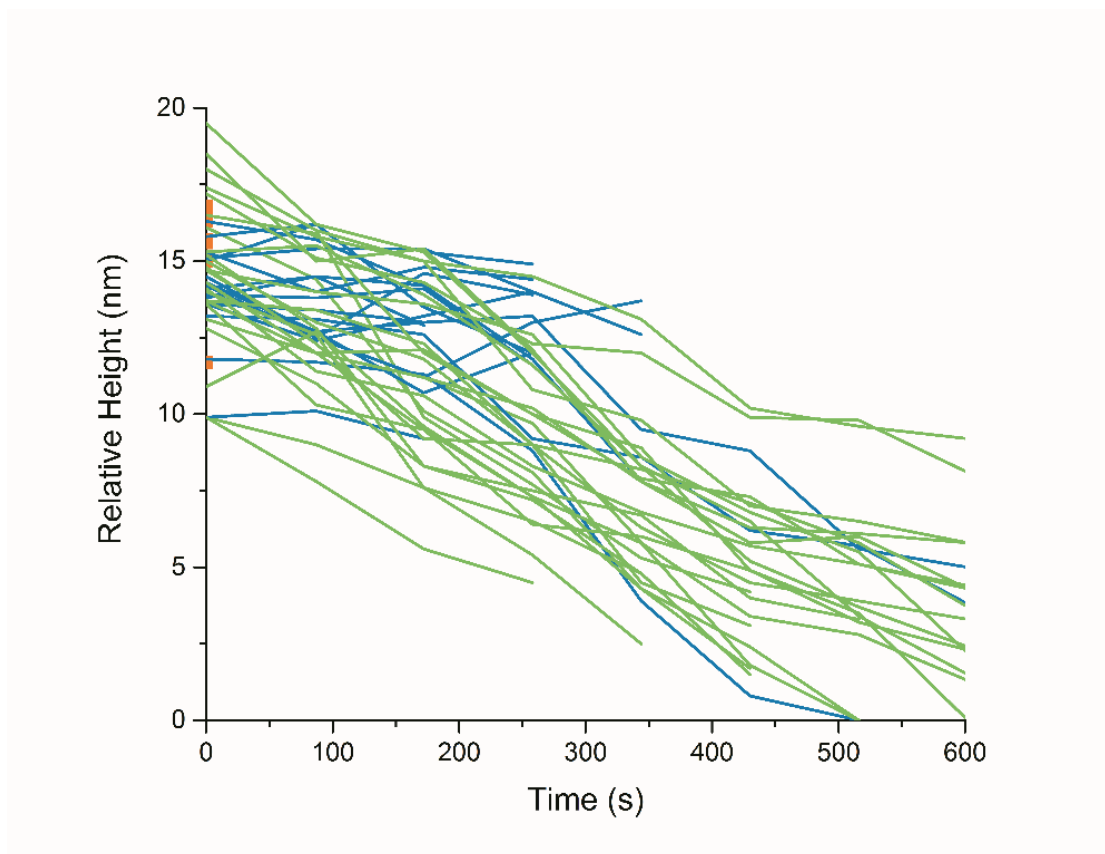


**Figure 2.10(S5).** Relative nanoparticle height over time for the PMAA-PBzMA nanoparticles. Each line corresponds to an individual nanoparticle tracked across multiple AFM images. The color coding by behavior type is the same to that in Figure S4: orange represents nanoparticle detachment ( $n = 7$ ), blue represents nanoparticle hovering ( $n = 17$ ), and green corresponds to immediate nanoparticle incorporation into the crystal ( $n = 26$ ). Incorporation appears to occur at similar rates for all nanoparticles.

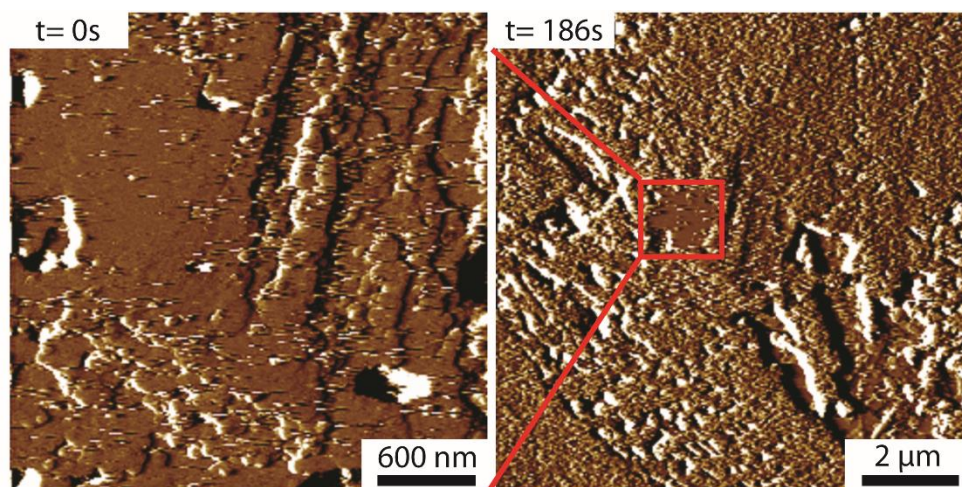


**Figure 2.11(S6).** *In situ* AFM images showing the effect of the AFM tip on PMAA-PBzMA nanoparticles on the surface of calcite. Similar observations were also made for HOOC-PGMA-PBzMA nanoparticles (not shown). The lower magnification image obtained at 186 seconds reveals the region where the sample was imaged. There are clearly some tip artifacts, but these will be identical for all samples analyzed and the most likely effect is to remove some of the “hovering” nanoparticles, thus preventing further binding and incorporation.

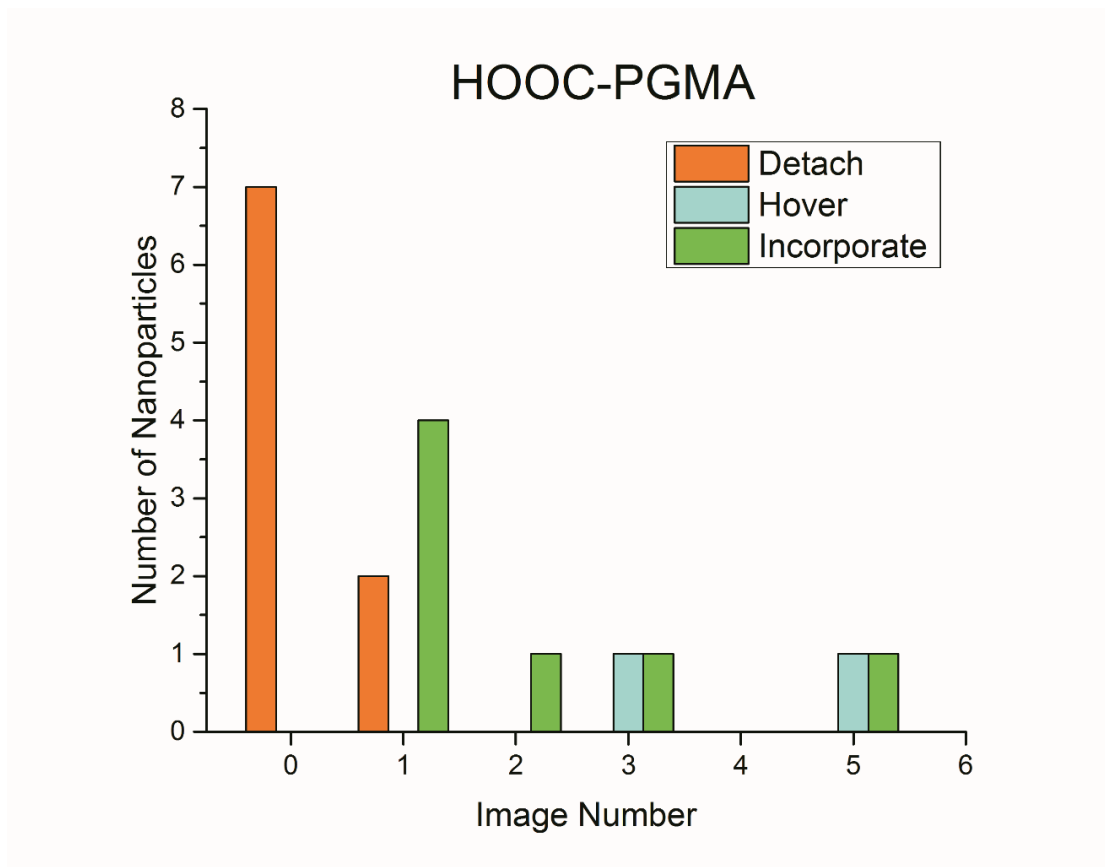


**Figure 2.12(S7).** Histogram showing the number of nanoparticles that either detach, hover or incorporate for HOOC-PGMA-PBzMA nanoparticles over time. The image number refers to the last image obtained before a significant ( $> 10\%$ ) height reduction is observed. Note the similarity to the histogram shown in Figure 5B of the main manuscript.

## REFERENCES

- (1) Lowenstam, H. .; Weiner, S. *On Biomineralization*; Oxford University Press Inc., 1989.
- (2) Addadi, L.; Weiner, S. *Phys. Scr.* 2014, 89 (9), 98003.
- (3) Weiner, S.; Wagner, H. D. *Annu. Rev. Mater. Sci.* 1998, 28 (1), 271.
- (4) Weiner, S.; Addadi, L. *Annu. Rev. Mater. Res.* 2011, 41 (1), 21.
- (5) Kim, Y.-Y.; Carloni, J. D.; Demarchi, B.; Sparks, D.; Reid, D. G.; Kunitake, M. E.; Tang, C. C.; Duer, M. J.; Freeman, C. L.; Pokroy, B.; Penkman, K.; Harding, J. H.; Estroff, L. A.; Baker, S. P.; Meldrum, F. C. *Nat. Mater.* 2016, 15 (8), 903.
- (6) Orme, C. A.; Noy, A.; Wierzbicki, A.; McBride, M. T.; Grantham, M.; Teng, H. H.; Dove, P. M.; DeYoreo, J. J. *Nature* 2001, 411 (6839), 775.
- (7) Davis, K. J.; Dove, P. M.; De Yoreo, J. J. *Science*. 2000, 290 (5494).
- (8) Qiu, S. R.; Orme, C. A. *Chemical Reviews*, 2008, 4784.
- (9) Poloni, L. N.; Ford, A. P.; Ward, M. D. *Cryst. Growth Des.* 2016, 16 (9), 5525.
- (10) Rimer, J. D.; An, Z.; Zhu, Z.; Lee, M. H.; Goldfarb, D. S.; Wesson, J. A.; Ward, M. D. *Science* 2010, 330 (6002), 337.
- (11) Vekilov, P. G.; Chung, S.; Olafson, K. N.; *MRS Bull.* 2016, 41 (5), 375.
- (12) Qiu, S. R.; Wierzbicki, A.; Orme, C. A.; Cody, A. M.; Hoyer, J. R.; Nancollas, G. H.; Zepeda, S.; De Yoreo, J. J. *Proc. Natl. Acad. Sci. U. S. A.* 2004, 101 (7), 1811.

- (13) Cho, K.R.; Kim, Y.-Y.; Yang, P.; Cai, W.; Pan, H.; Kulak, A. N.; Lau, J. L.; Kulshreshtha, P.; Armes, S. P.; Meldrum, F. C.; De Yoreo, J. J. *Nat. Commun.* 2016, 7, 10187.
- (14) Friddle, R. W.; Weaver, M. L.; Qiu, S. R.; Wierzbicki, a; Casey, W. H.; De Yoreo, J. J. *Proc. Natl. Acad. Sci. U. S. A.* 2010, 107 (1), 11.
- (15) S. Elhadj; E. A. Salter; A. Wierzbicki; J. J. De Yoreo; N. Han; Dove, P. M. *Crystal Growth and Design*, 2005, 6(1), 197.
- (16) Elhadj, S.; De Yoreo, J. J.; Hoyer, J. R.; Dove, P. M. *Proc. Natl. Acad. Sci. U. S. A.* 2006, 103 (51), 19237.
- (17) Weaver, M. L.; Qiu, S. R.; Friddle, R. W.; Casey, W. H.; De Yoreo, J. J. *Cryst. Growth Des.* 2010, 10 (7), 2954.
- (18) Shtukenberg, A. G.; Tripathi, K.; Ketchum, R.; Jeon, J. J.; Sanda, A.; Kahr, B. *Cryst. Growth Des.* 2016, 16 (8), 4589.
- (19) Li, H.; Xin, H. L.; Kunitake, M. E.; Keene, E. C.; Muller, D. A.; Estroff, L. A. *Adv. Funct. Mater.* 2011, 21 (11), 2028.
- (20) Pokroy, B.; Fitch, A. N.; Marin, F.; Kapon, M.; Adir, N.; Zolotoyabko, E. J. *Struct. Biol.* 2006, 155 (1), 96.
- (21) Kunitake, M. E.; Mangano, L. M.; Peloquin, J. M.; Baker, S. P.; Estroff, L. A. *Acta Biomater.* 2013, 9 (2), 5353.
- (22) Elhadj, S.; De Yoreo, J. J.; Hoyer, J. R.; Dove, P. M. *Proc. Natl. Acad. Sci. U. S. A.* 2006, 103 (51), 19237.
- (23) Ning, Y.; Fielding, L. A.; Doncom, K. E. B.; Penfold, N. J. W.; Kulak, A. N.; Matsuoka, H.; Armes, S. P. *ACS Macro Lett.* 2016, 5 (3), 311.

- (24) Kim, Y.-Y.; Ribeiro, L.; Maillot, F.; Ward, O.; Eichhorn, S. J.; Meldrum, F. C. *Adv. Mater.* 2010, 22 (18), 2082.
- (25) Kim, Y.-Y.; Ganesan, K.; Yang, P.; Kulak, A. N.; Borukhin, S.; Pechook, S.; Ribeiro, L.; Kröger, R.; Eichhorn, S. J.; Armes, S. P.; Pokroy, B.; Meldrum, F. C. *Nat. Mater.* 2011, 10 (11), 890.
- (26) Muñoz-Espí, R.; Qi, Y.; Lieberwirth, I.; Gómez, C. M.; Wegner, G. *Chem. - A Eur. J.* 2006, 12 (1), 118.
- (27) Wegner, G.; Demir, M. M.; Faatz, M.; Gorna, K.; Munoz-Espi, R.; Guillemet, B.; Gröhn, F. *Macromol. Res.* 2007, 15 (2), 95.
- (28) Kim, Y.-Y.; Semsarilar, M.; Carloni, J. D.; Cho, K. R.; Kulak, A. N.; Polishchuk, I.; Hendley, C. T.; Smeets, P. J. M.; Fielding, L. A.; Pokroy, B.; Tang, C. C.; Estroff, L. A.; Baker, S. P.; Armes, S. P.; Meldrum, F. C. *Adv. Funct. Mater.* 2016, 26 (9), 1382.
- (29) Ning, Y.; Fielding, L. A.; Ratcliffe, L. P. D.; Wang, Y.-W.; Meldrum, F. C.; Armes, S. P. *J. Am. Chem. Soc.* 2016, 138 (36), 11734.
- (30) Canning, S. L.; Smith, G. N.; Armes, S. P. *Macromolecules* 2016, 49 (6), 1985.
- (31) Warren, N. J.; Armes, S. P. *J. Am. Chem. Soc.* 2014, 136 (29), 10174.
- (32) Derry, M. J.; Fielding, L. A.; Armes, S. P. *Prog. Polym. Sci.* 2016, 52, 1.
- (33) Hanisch, A.; Yang, P.; Kulak, A. N.; Fielding, L. A.; Meldrum, F. C.; Armes, S. P. *Macromolecules* 2016, 49 (1), 192.
- (34) Ning, Y.; Fielding, L. A.; Andrews, T. S.; Growney, D. J.; Armes, S. P. *Nanoscale* 2015, 7 (15), 6691.

- (35) Parnell, A. J.; Martin, S. J.; Dang, C. C.; Geoghegan, M.; Jones, R. A. L.; Crook, C. J.; Howse, J. R.; Ryan, A. J. *Polymer (Guildf)*. 2009, 50 (4), 1005.
- (36) Minko, S. J. *Macromol. Sci. Part C Polym. Rev.* 2006, 46 (4), 397.
- (37) Berman, A.; Addadi, L.; Kwick, Å.; Leiserowitz, L.; Nelson, M.; Weiner, S. *Science*. 1990, 250 (4981).
- (38) Metzler, R. A.; Tribello, G. A.; Parrinello, M.; Gilbert, P. U. P. A. *J. Am. Chem. Soc.* 2010, 132 (33), 11585.
- (39) Meldrum, F. C.; Hyde, S. T. J. *Cryst. Growth* 2001, 231 (4), 544.
- (40) Poloni, L. N.; Zhong, X.; Ward, M. D.; Mandal, T. *Chemistry of Materials*, 2016, 29 (1), 331.
- (41) De Yoreo, J. J.; Chung, S.; Friddle, R. W. *Adv. Funct. Mater.* 2013, 23 (20), 2525.
- (42) Yoreo, J. J. De; Vekilov, P. G. *Principles of Crystal Nucleation and Growth* 2003.
- (43) Weaver, M. L.; Qiu, S. R.; Friddle, R. W.; Casey, W. H.; Yoreo, J. J. De. *Crystal Growth and Design*, 2010, 10 (7), 2954.
- (44) Munk, P. In *Solvents and Self-Organization of Polymers*; Springer Netherlands: Dordrecht, 1996; pp 19–32.
- (45) De La Pierre, M.; Raiteri, P.; Gale, J. D. *Cryst. Growth Des.* 2016, 16 (10), 5907.
- (46) De La Pierre, M.; Raiteri, P.; Stack, A. G.; Gale, J. D. *Angew. Chemie Int. Ed.* 2017, 56 (29), 8464.

- (47) Derry, M. J.; Fielding, L. A.; Armes, S. P. *Polym. Chem.* 2015, 6 (16), 3054.
- (48) Aizenberg, J.; Black, A. J.; Whitesides, G. M. *Nature* 1999, 398 (6727), 495.

## CHAPTER 3

### TUNING PARTICLE-SUBSTRATE INTERACTIONS WITH SOLUTION CHEMISTRY

Coit T. Hendley IV<sup>1</sup>, Lee A. Fielding<sup>2</sup>, Elizabeth R. Jones<sup>3</sup>, Anthony Ryan<sup>3</sup>, Steven P. Armes<sup>3</sup>, Lara Estroff<sup>1,4\*</sup>

<sup>1</sup>Department of Materials Science and Engineering, Cornell University, Ithaca, NY 14853, USA.

<sup>2</sup>The School of Materials, University of Manchester, Oxford Road, Manchester, M13 9PL, UK

<sup>3</sup>Department of Chemistry, University of Sheffield, Brook Hill, Sheffield, Yorkshire, S3 7HF, UK.

<sup>4</sup>Kavli Institute, Cornell University, Ithaca, NY 14853, USA.

#### **3.1 Abstract**

Incorporation of functional materials into single crystals is a long held goal of the crystal growth community because of the potential to synthesize composites with properties that would not be expected based on their constituents. Recently, progress has been made using long polymeric stabilizer chains for both polymeric and inorganic nanoparticles. An understanding of the mechanisms of particle-crystal interactions is needed before chemistries can be designed that optimally incorporate nanoparticles into single crystals. *In situ* Atomic Force Microscopy (AFM) has proven

to be a valuable tool for directly observing particles as they interact with and are incorporated into single crystals of calcite. In this work we use evidence from *in situ* AFM experiments to propose two regimes of particle-crystal interactions: (i) *particle driven* where the structure of the charge corona determines the interaction with the crystal, and (ii) *surface driven*, where the local environment on the crystal surface determines the interaction.

### **3.2 Introduction**

Incorporating additives into single crystals is of significant interest because of the potential for synthesizing composites with emergent properties. Calcite serves as an ideal model system for studying additive-crystal interactions because it relatively easily incorporates additives into micron size single crystals. Previous work has extensively studied the role of atomic substitutions, small molecules, peptides, and nanoparticles using both *ex situ* and *in situ* methods in the context of biomineral formation.<sup>1-6</sup> Of particular interest are nanoparticles, because optimizing nanoparticle incorporation into single crystals would enable designer single crystal composites. A wide variety of nanoparticles, such as latex, metal oxides, and block copolymer micelles readily become incorporated into calcite single crystals.<sup>6-9</sup> However, generally nanoparticle incorporation requires that the particles are stabilized by polymer chains with high densities of negatively charged groups, usually carboxylic acids.<sup>9-12</sup> Therefore understanding the interactions at the organic-inorganic interface when the particles are on the crystal surface is critical. We expect that particle-surface interactions will be strongly affected by the bound hydration layers present on crystal

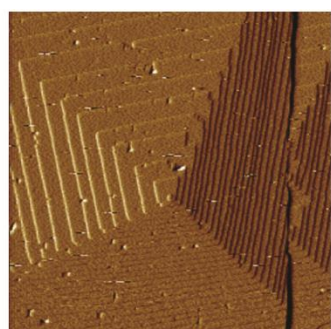
surfaces in aqueous solution because water at the interface is highly structured.<sup>13</sup> Ions in solution can potentially affect both the structuring of the hydration layer and the structure of the nanoparticles, so solution chemistry is likely an important factor when considering particle-crystal interactions. In this work we utilize *in situ* Atomic Force Microscopy (AFM) to directly observe nanoparticles on a growing crystal surface, because it makes possible detailed analysis of additive-surface interactions.<sup>1,4,14–16</sup>

In particular, polymer nanoparticles have been the focus of nanoparticle-crystal interactions *in situ* because they have easily tunable surface chemistry. In depth investigations directly observing polymeric nanoparticles on a growing calcite crystal using *in situ* (AFM) have begun to reveal the particle-crystal interactions. Cho and coworkers were the first to study the nanoparticle-calcite interaction and showed that individual polymeric particles land on the crystal surface, diffuse to step edges, and subsequently become occluded in the crystal by step propagation.<sup>17</sup> Our group recently studied the behavior of populations of nanoparticles as they interact with the surface. (Chapter 2) By tracking large numbers of nanoparticles as they interacted with the surface we showed that the particle-crystal interaction for polymeric nanoparticles is determined by the structure of the charge corona. Depending on the charge corona chemistry, the population of particles is divided between three possible behaviors: detachment from the surface, hovering on the surface, or collapsing on the surface and becoming incorporated. The collapsed state best facilitates incorporation into the crystal because it forces steps to grow around and occlude the particle. This work utilizes *in situ* AFM to help complete our understanding of the effects of different solution conditions on particle-crystal interactions.

### *3.2.1 Polyelectrolyte Nanoparticles are Affected by Solution Conditions*

Polymeric nanoparticles in water have a dense coating of hydrophilic stabilizer chains that keep the particles from aggregating in solution. These chains are typically spaced within one radius of gyration of one another, which causes the chains to behave as if they were polymer brushes.<sup>18</sup> To explore the effects of growth conditions on particle-crystal interactions we chose polymeric nanoparticles with two different surface chemistries; one with a carboxylic acid group at the end of each stabilizer chain (HOOC-PGMA-PBzMA, Figure 1), and one with fully acidified stabilizer chains (PMAA-PBzMA, Figure 1). The PMAA-PBzMA particles act as a weak polyelectrolyte and exhibit swelling with increasing pH because the chains are forced to separate and extend by coulombic repulsion and osmotic pressure as the acidic groups become deprotonated.<sup>18-20</sup> Increasing cation concentration can also swell the particles as the ions enter the area around the chains to balance the charges.<sup>18,19,21</sup> However, once charge balance is satisfied the polyelectrolyte chains collapse, which is called the “salted” or “collapsed” state.<sup>18-20</sup> Though this effect can be caused by any cation, divalent cations are much more effective at collapsing a polyelectrolyte than monovalent because they can crosslink the stabilizer chains.<sup>20,21</sup> The HOOC-PGMA-PBzMA particles will not behave as a polyelectrolyte and cannot access such a dynamic collapse. They only have one negative charge at the end of each chain, which makes the conformation of the PGMA chains relatively relaxed and flexible as well as insensitive to changes in pH and cation concentration. With particles of two different surface chemistries and charge corona structures, we can compare the particle-surface

interactions as a function of changing supersaturation and ionic strength as well as the effects of changing the concentration of divalent or monovalent ions.

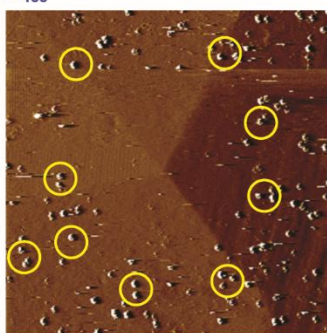
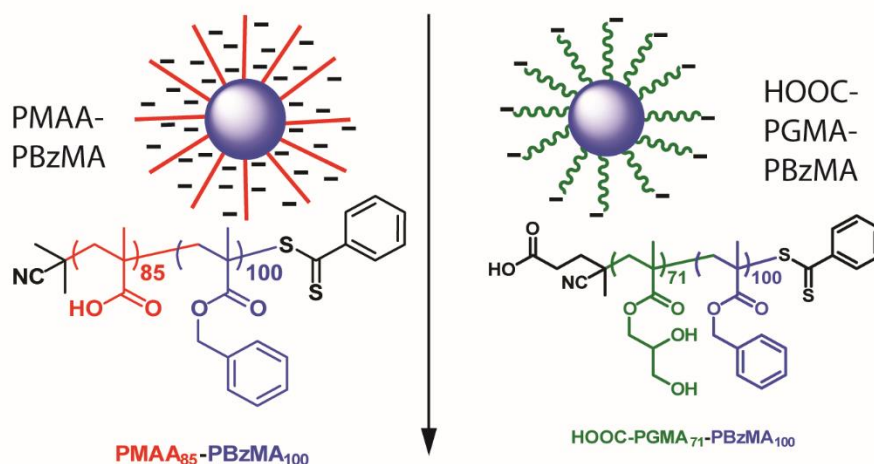


Experimental Conditions

	$\sigma = 0.76$	$\sigma = 1.15$	$\sigma = 1.54$
IS= 35 mM		IS <sub>1</sub>	
IS= 45 mM	$\sigma_1$	$\sigma_2$ , IS <sub>2</sub>	$\sigma_3$
IS= 55 mM		IS <sub>3</sub>	

600.0 nm

A: Control Growth    B: Choose Growth Condition and Particle



2.0  $\mu\text{m}$

C: Count and Track Particles

**Scheme 3.1:** Experimental Design. We use two different types of polymeric nanoparticles to evaluate the importance of solution conditions like supersaturation

and ionic strength. Here we show a control growth hillock on calcite (A) from which we subsequently choose a growth condition and nanoparticle (B). Then we observe the effects on the hillock and track the nanoparticles over time as growth proceeds (C).

Our workflow is as follows (Scheme 1): First, using a fluid flow setup optimized for calcite growth, a hillock is grown on a sample of geologic calcite using a solution of  $\text{CaCO}_3$  in an AFM (Scheme 1A). The supersaturations are low enough so only hillock growth is accessible.<sup>14,22</sup> Once a stable hillock is formed, the growth conditions (supersaturation or ionic strength) can be increased or decreased by simply changing ion concentrations in the inflowing solution (Scheme 1B: Experimental Conditions  $\sigma_{1-3}$ ,  $\text{IS}_{1-3}$ ). Then a growth solution containing the particle of interest is added (Scheme 1B: PMAA-PBzMA or HOOC-PGMA-PBzMA). Finally, we take a series of images of the hillock as growth proceeds with the nanoparticles present and track the particle population. We performed experiments that spanned both supersaturation and ionic strength (Scheme 1B: Experimental Conditions  $\sigma_{1-3}$ ,  $\text{IS}_{1-3}$ ).

### 3.3 Results and Discussion

#### 3.3.1 Nanoparticle Structuring in Solution

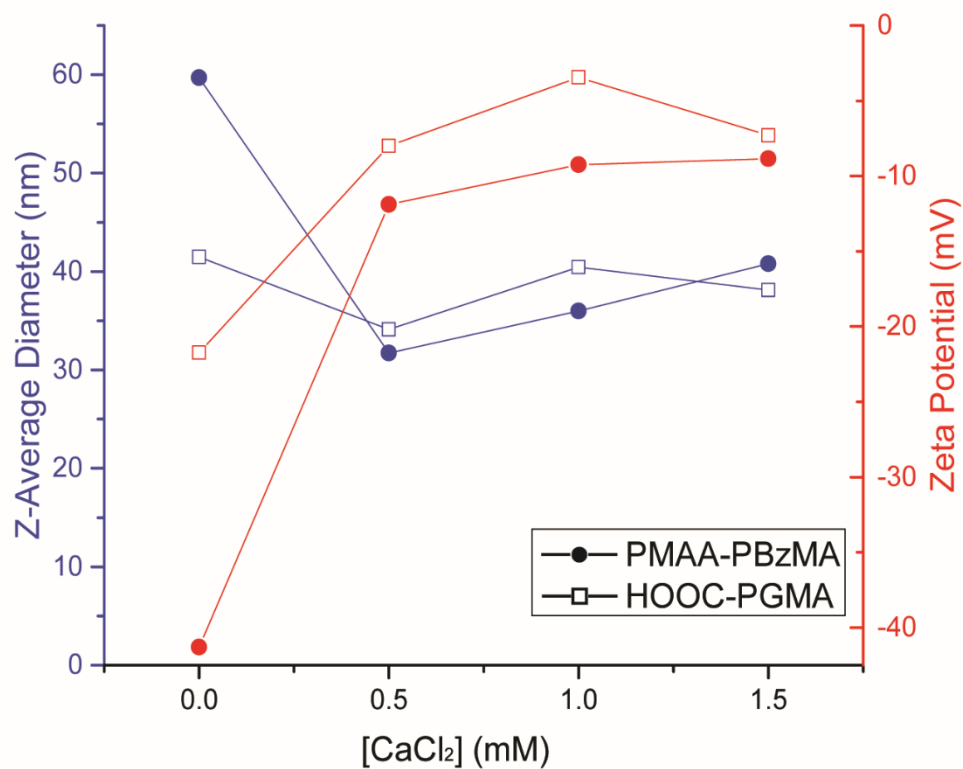


**Figure 3.1:** Z-average diameter and zeta potential measurements as a function of calcium chloride concentration for both nanoparticle types used in this study. pH = 8 set using KOH, CaCl<sub>2</sub> diluted from 1 M stock solution (CaCl<sub>2</sub>·2H<sub>2</sub>O, Sigma Aldrich).

Before imaging the particle-crystal interactions we studied the solution behavior of the nanoparticles as a function of calcium chloride concentration at pH 8 (Figure 1). For both nanoparticle types, the zeta potential becomes less negative at very low concentrations (0.5 mM calcium chloride). Strikingly, at the same calcium

chloride concentration, the diameter of the PMAA-PBzMA nanoparticles is reduced by ~30 nm while the diameter of the HOOC-PGMA-PBzMA nanoparticles is unchanged. The decrease in diameter is consistent with the PMAA stabilizer chains collapsing in the presence of divalent cations. When monovalent sodium is used instead of divalent calcium, we observe charge screening for the PMAA-PBzMA nanoparticles, but no decrease in diameter for concentrations as high as 45 mM NaCl (Supplementary Figure S1).

### 3.3.2 Divalent Cations Increase Surface Interactions

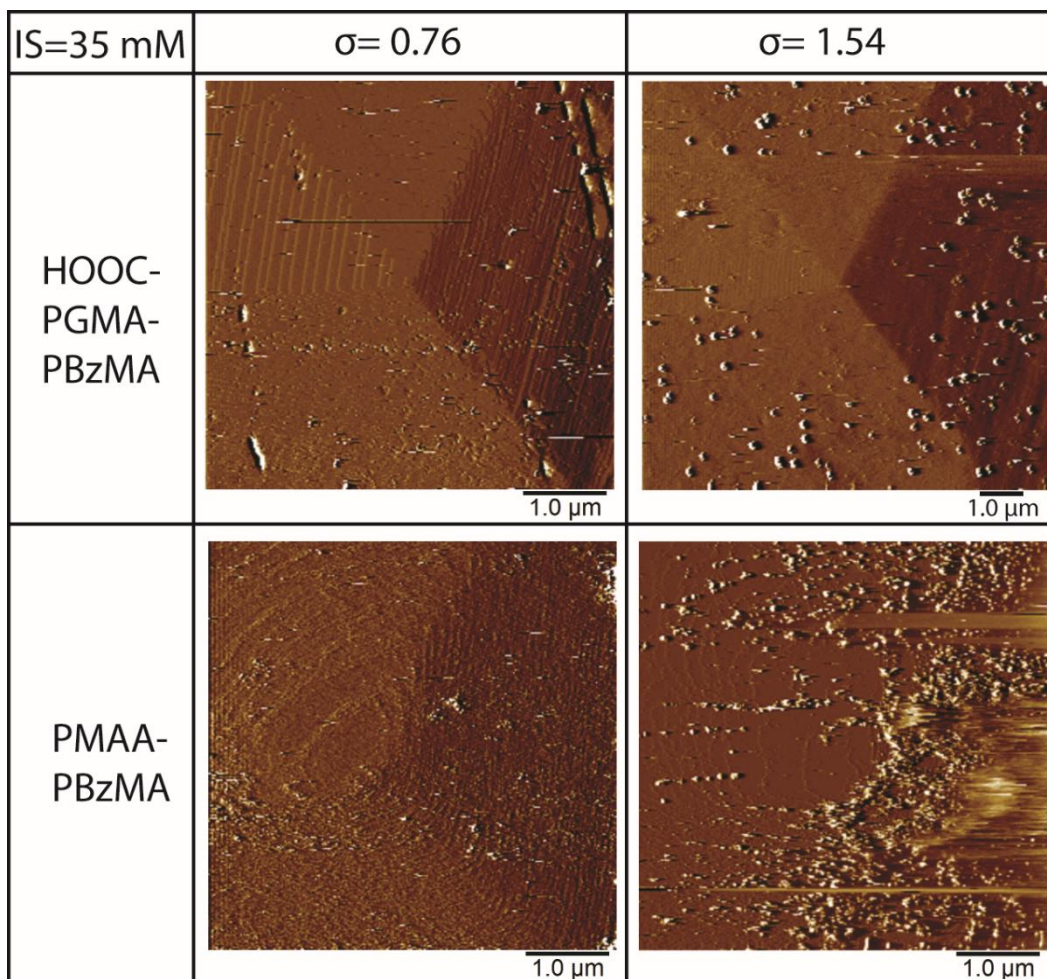


**Figure 3.2:** Representative AFM images (at  $t \sim 10$  min after adding nanoparticles) from experiments spanning supersaturation. Qualitatively supersaturation has a major impact on the particle-crystal interaction. An increase in supersaturation brought by increasing  $[\text{Ca}^{2+}]$  and  $[\text{CO}_3^{2-}]$  in solution greatly enhances the attachment of both types of particles to the surface. In particular, for the PMAA-PBzMA particles, a film of particles forms on the surface at the highest sigma. Particle concentration is 0.00075% wt.  $\sigma=0.76$  corresponds to 1.4 mM  $\text{CaCl}_2$  and  $\sigma=1.54$  is  $[\text{CaCl}_2] = 2.2$  mM. The  $[\text{NaCl}]$  is adjusted to keep the ionic strength (IS) constant at 35 mM.

From our previous studies, we know that a collapsed particle state should lead to increased attachment to the crystal surface and increased incorporation. Our DLS data indicate that increased divalent cation concentration will increase particle collapse in solution. Therefore, we should be able to drive the particle attachment/incorporation by increasing  $[\text{Ca}^{2+}]$  and supersaturation. Figure 2 presents an *in situ* sampling of the particle-crystal interaction at supersaturations corresponding to  $\pm 20\%$   $[\text{Ca}^{2+}]$  around  $\sigma=1.15$  ( $[\text{Ca}^{2+}] = 1.8$  mM). The effect is clear even upon qualitative analysis (Fig. 2). Both types of nanoparticles attach with greater frequency at condition  $\sigma_3$ , while hardly attaching at all at condition  $\sigma_1$  (Fig. 2). The polyelectrolyte PMAA-PBzMA particles qualitatively attach in greater quantities than HOOC-PGMA-PBzMA, so much so that at  $\sigma_3$  the PMAA-PBzMA particles begin to form a film on the surface which persists even under continuous tip rastering in

contact mode (Supplementary Figures S2 and S3). Previous reports indicate that normally such a film would be subject to movement by the tip. (Chapter 2)

We can quantitatively measure the attachment by analyzing the area of the crystal surface that is covered by particles in a given image (Methods, Supplementary Figure S4). Our surface coverage measurements indicate that an increase in  $[Ca^{2+}]$  increases attachment to the surface for both particle types (Figure 3). The large increase in attachment for the PMAA-PBzMA particles is likely related to the polyelectrolyte character of PMAA. Polyelectrolyte behavior is driven by cations, so calcium is key to understanding the particle-crystal interaction in this case. Though we cannot strictly deconvolute the effects of supersaturation from  $[Ca^{2+}]$ , polyelectrolytes are extremely sensitive to divalent cation concentration (as shown in

the DLS), so we believe the disproportionate increase in attachment is most easily explained by the increasing cation concentration.

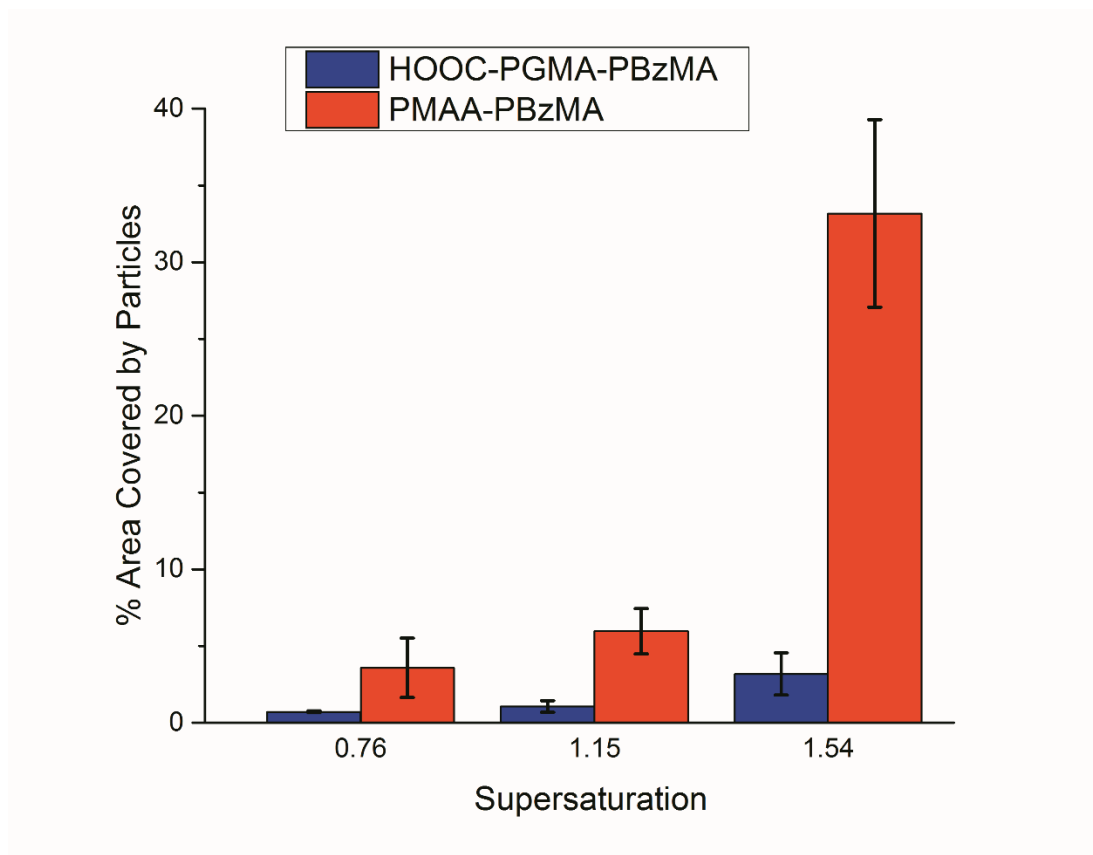


**Figure 3.3:** Area coverage measured by ImageJ at three different supersaturations, and constant IS=35. Both particle types increase in coverage with increasing supersaturation. From  $\sigma=1.15$  to  $\sigma=1.54$  the PMAA attachment increases significantly and disproportionately. Data are the mean of measurements across five images from  $t\sim 10$  to  $t\sim 15$  min after particle injection. Error bars are one standard deviation above and below the mean

### 3.3.3 Polyelectrolyte particle-surface interactions depend on particle structure

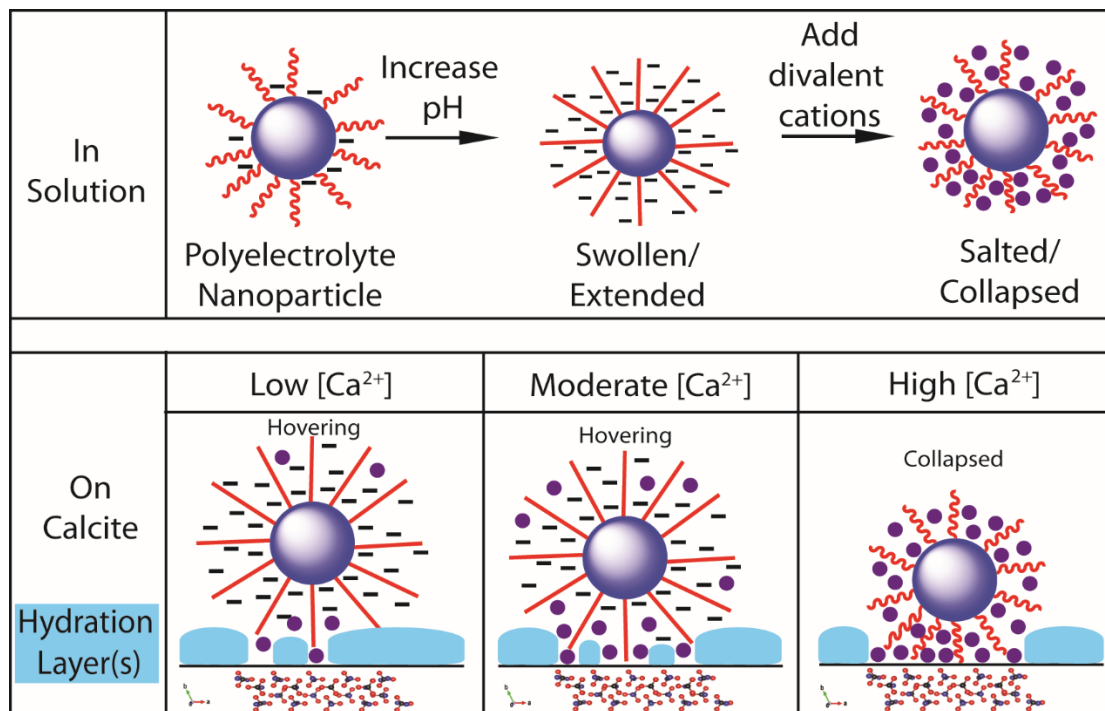


**Figure 3.4:** Structural changes in the charge corona of a polyelectrolyte nanoparticle with pH and cation concentration such as the PMAA-PBzMA nanoparticles used in this study. Chains are extended by osmotic pressure and coulombic repulsion at the pH of calcite growth (pH 8) but are collapsed if there is sufficient concentration of cations to satisfy the negative charges on the chains.

The PMAA-PBzMA particles are polyelectrolytes and as such their charge corona is changed when cation concentration varies. With increasing pH, the PMAA chains first become extended and osmotically swollen as Coulombic repulsion forces the chains apart from one another (Fig. 4). However, once enough divalent cations are

localized in the PMAA chains, the charges balance, and the chains crosslink and collapse (Fig. 4). Zeta potential and diameter measurements illustrate that the collapse effect occurs with increasing  $[\text{Ca}^{2+}]$  but not with  $[\text{Na}^+]$  (Figure 1 and Supplementary Figure S1). Any cation should be able to salt and collapse a polyelectrolyte at high enough concentrations, but divalent cations are much more potent than monovalent.<sup>20,21</sup>

On the crystal surface, if the particle remains in the swollen/extended state it is more likely to detach from the surface or “hover” on the surface as we have previously reported. (Chapter 2) In contrast, the collapsed state leads to more particle-crystal bonds forming and therefore makes incorporation more favorable as the steps are forced to grow around the particle (Fig. 4). Increasing  $[\text{Ca}^{2+}]$  increases the number of PMAA-PBzMA nanoparticles in the collapsed state, increasing attachment to the surface. The collapsed state also most easily displaces the hydration layer on the surface. Though in principle increasing  $[\text{Na}^+]$  should eventually cause the same effect, we do not observe it here. In fact, as long as  $\text{Ca}^{2+}$  is present, it dominates the interaction. Because the state of the particle determines its interaction with the growing crystal we have termed this regime *particle driven interaction*.

In an attempt to quantify the expected increase in particle incorporation, we performed an *ex situ* experiment studying the impact of varying supersaturation in the presence of the PMAA-PBzMA nanoparticles (Supplementary Fig. S5). However, at higher driving forces we observed the presence of some polycrystalline aggregate structures (calcite and vaterite by XRD, Fig. S6), so we could not analyze individual

single crystals to measure incorporation. Therefore, we focused on *in situ* growth studies to remove this variable and study the effect of the particles on growth only.

### 3.3.4 Background electrolyte reveals a second interaction regime

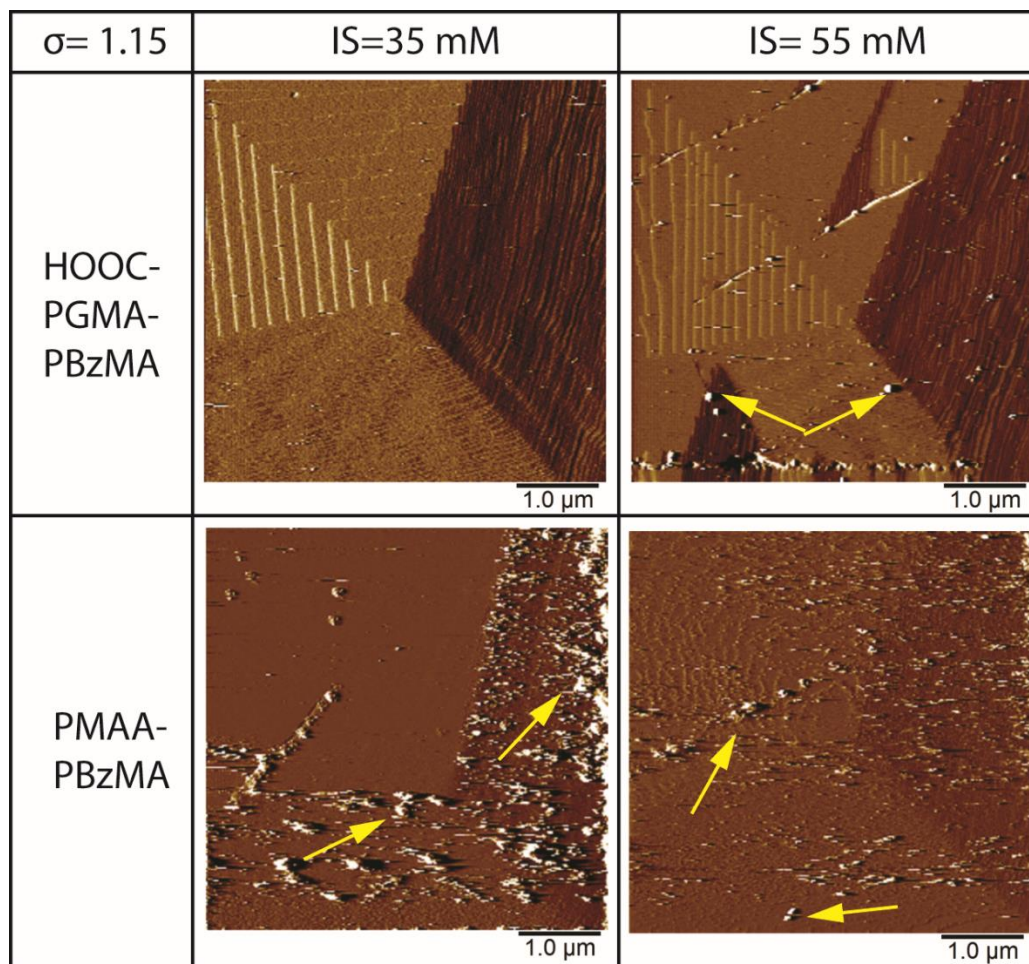


**Figure 3.5:** Representative AFM images (at  $t \sim 10$  min) after introduction of 0.00075 % wt particles. Effect of varying ionic strength by changing [NaCl] in the growth solution. The increase in the number of HOOC-PGMA-PBzMA particles (yellow arrows, top right) which attach to the crystal surface is notable. The PMAA particles

appear to attach readily at both ionic strengths (yellow arrows, bottom).  $\sigma=1.15$  corresponds to  $[\text{Ca}^{2+}] = 1.8 \text{ mM}$ . The ionic strength is varied by changing  $[\text{NaCl}]$ .

If the PMAA nanoparticles in the collapsed state more easily attach and push away the hydration layer, than disrupting the hydration layer using monovalent ions could also enhance attachment without affecting the particle. Some monovalent cations are already present during the growth in the form of  $\text{Na}^+$  as part of the background electrolyte, though their effect on the growth is generally understood to be limited to minor binding at the acute step edges.<sup>23,24</sup> We vary  $[\text{Na}^+]$  by controlling the ionic strength with  $[\text{NaCl}]$  in the growth solution while keeping  $[\text{Ca}^{2+}]$  constant. A representative set of images reveals the HOOC-PGMA-PBzMA nanoparticles appear to have little or no interaction with the crystal at condition  $\text{IS}_1$  but are clearly visible on the surface at condition  $\text{IS}_3$  (Fig. 2). A change in IS does not affect the structure of HOOC-PGMA-PBzMA nanoparticles so any change in the attachment cannot be *particle driven*. We can more quantitatively estimate the area covered by particles on the surface using a threshold in ImageJ (Methods, Supplementary Figure S4 for details). These analyses indeed show that the HOOC-PGMA-PBzMA particles cover more area at a higher IS (Fig. 6). In contrast, according to our area measurements, the PMAA-PBzMA particles are relatively unaffected by varying  $[\text{NaCl}]$  while still covering more of the crystal surface than the HOOC-PGMA-PBzMA particles (Fig. 6). The effects of  $[\text{NaCl}]$  lead us to hypothesize there are indeed two different interaction regimes.

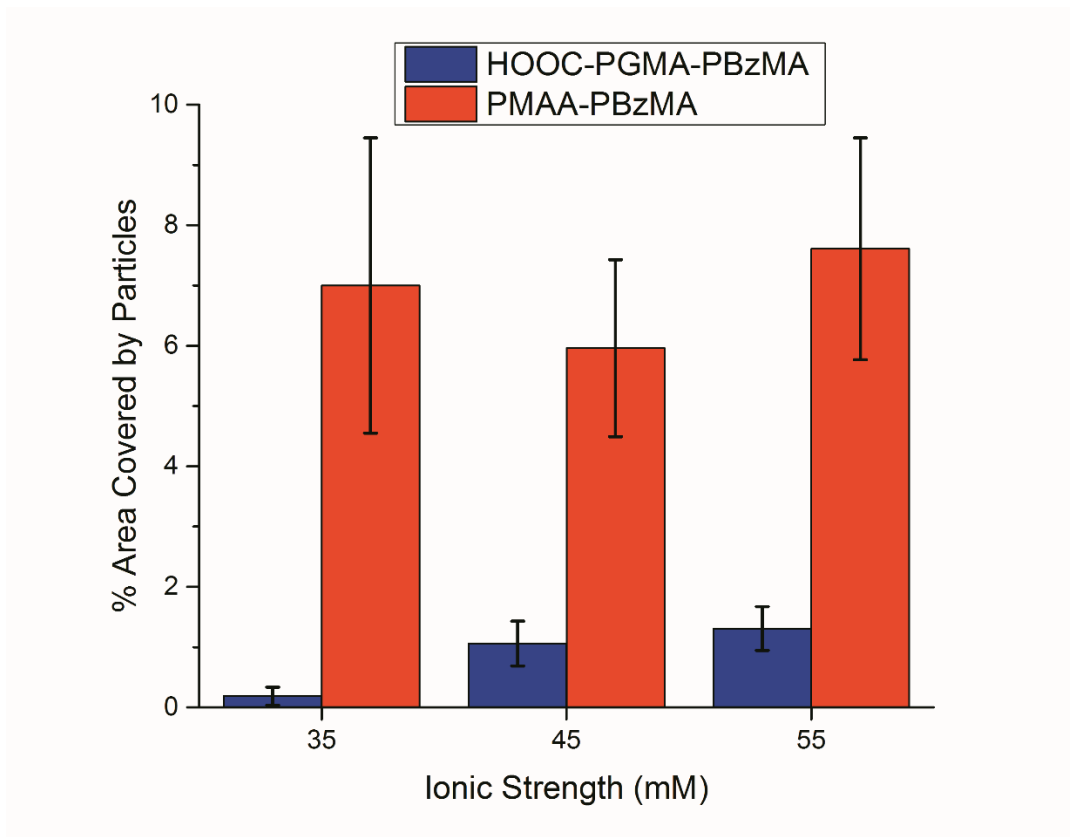


**Figure 3.6:** Area coverage measured by ImageJ at three different ionic strengths, and constant  $\sigma=1.15$ . There is no apparent change for the PMAA-PBzMA nanoparticles while no binding increases to ~1% coverage for HOOC-PGMA-PBzMA nanoparticles. Data are the mean of measurements across five images from  $t \sim 10$  to  $t \sim 15$  min after particle injection. Error bars are one standard deviation above and below the mean.

### 3.3.5 Non-polyelectrolyte particle binding depends on hydration layer structure

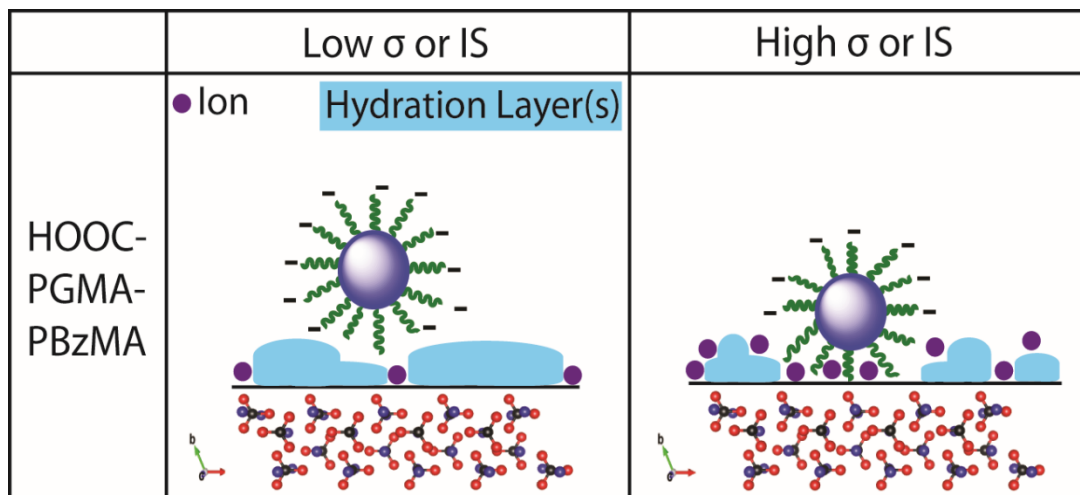


**Figure 3.7:** The interaction between HOOC-PGMA-PBzMA particles and calcite is determined by the local crystal surface environment. Calcite structure is adapted from Margraff, Reeder, 1985 (AMSCD).

The HOOC-PGMA-PBzMA particle corona is not affected by a change in pH or ion concentration since PGMA is not a polyelectrolyte (Figure 1). Therefore, its interaction with the surface can only be affected by highly localized changes in the near-surface environment. Computational and experimental work has suggested that the limiting factor governing binding of additives to calcite is the dehydration of the two or more hydration layers of bound water on the crystal surface.<sup>13,25</sup> We propose that the increase in HOOC-PGMA-PBzMA particle attachment with ionic strength can be explained by the cations (or anions) facilitating the interaction by disrupting the hydration layer or by enhancing the favorability of binding sites on the hydration layer itself (Fig. 7). In the case of sodium or chloride, the effect is weaker than that of

calcium or carbonate; though sodium does interact with the calcite surface (in particular the acute step edge), it does not bind as strongly as calcium or carbonate.<sup>23,24</sup> Since only the local surface environment drives the interaction in this case, we have termed this the *surface driven interaction* regime. It is possible that at much higher IS (e.g., >1 M NaCl), salting-out of the PMAA-PBzMA corona could occur, but since such high electrolyte concentrations could cause particle aggregation or grow undesired crystal phases we did not pursue this option. The relatively limited effect of varying IS on the PMAA-PBzMA particles lead us to conclude that the *surface driven* effect is substantially weaker and only present if there are no polyelectrolyte particles.

We can now predict based on our *in situ* results that increasing IS results in an increase in particle-crystal interaction for HOOC-PGMA-PBzMA in general. To test our prediction, we performed a bulk growth experiment of calcite *ex situ* with the HOOC-PGMA-PBzMA nanoparticles using the ammonia diffusion method. The bulk growth shows that indeed the interaction between the nanoparticles and the crystal is enhanced by increasing from 5 mM NaCl to 500 mM NaCl (Supplementary Figure S7). The crystal morphology becomes increasingly roughened only in the presence of nanoparticles. Increased roughness implies at a minimum there is increased surface interaction and modification. It can also indicate increased incorporation either near the crystal surface or throughout the bulk of the crystal. With refined control over the nanoparticle-crystal interactions, we can probe the nuances of the particle-surface interactions.

### 3.3.6 Micelle Bonding Permanency

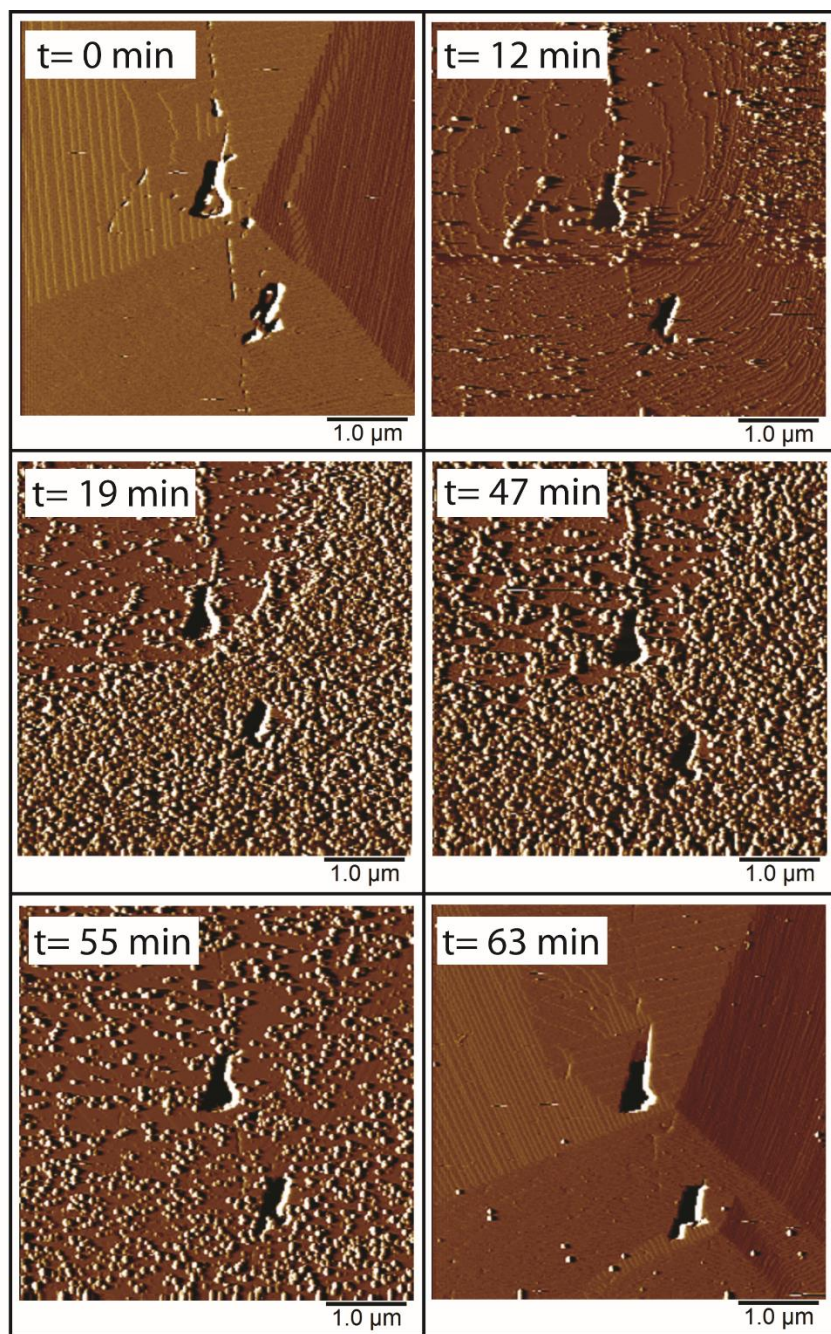


**Figure 3.8:** Growth and recovery of a hillock as PMAA-PBzMA nanoparticles round the hillock and form a bound film (t=0 min to t=47 min) and then are gradually

removed via incorporation near the hillock peak once a control growth solution is added (t=47 min to t=63 min). Growth at  $\sigma=1.54$  (2.2 mM  $\text{Ca}^{2+}$ ) and .00075% wt nanoparticles.

Typically during *in situ* AFM experiments studying the effect of an additive is limited to the kinetic changes to the hillock under growth or dissolution conditions. However, with a more complete understanding of particle-surface interactions, we can now study the kinetics of nanoparticle-surface binding. Either the particles are bound irreversibly and act as a step pinner to block growth, or the bonding is an equilibrium, and the particles can freely attach and detach from the surface. The bound film of nanoparticles at the highest supersaturation tested ( $\sigma_3=1.54$ ) makes it possible to conveniently test such kinetic binding principles. We performed a growth experiment at growth condition  $\sigma_3$  with nanoparticles present, but instead of simply continuously imaging the growth in the presence of particles, once a film of particles was observed, the growth solution was changed to a pure calcium carbonate solution ( $\sigma_3=1.54$ ) with no polymer particles. Figure 8 and Movie S1 reveal that though the particles attach and form a film over ~12 min, more than twice that time is required for them to begin to disappear from the surface. It appears that they are primarily becoming incorporated near the hillock peak (Fig. 8 t=47 min to t=63 min). Further, consistent with our previous report, (Chapter 2) we observe the growth hillock (particularly the acute step edges) becoming severely rounded (Fig. 8 t=12 min). However, once the nanoparticles are no longer on the hillock surface, the growth hillocks regain their original rhombohedral morphology (Fig. 8 t=63 min). Lower magnification imaging reveals

the crystal cannot completely recover from the effects of the nanoparticles on the growth (Figure 9). Once the particles are bound to the surface, growth apparently proceeds along the hillock peak and ridges even while particles are still flowing in (Fig. 9 t=12 min to t=42 min). Upon switching to pure growth solution, a hopper like region emerges under the particle film before the hillock fully recovers (Fig. 9 t=36 min to t=60 min). Once the hillock fully recovers, growth proceeds rapidly upward, apparently generating a macrostep, or multi-growth unit high step edge (Fig. 9 t=60 min-t=95 min).

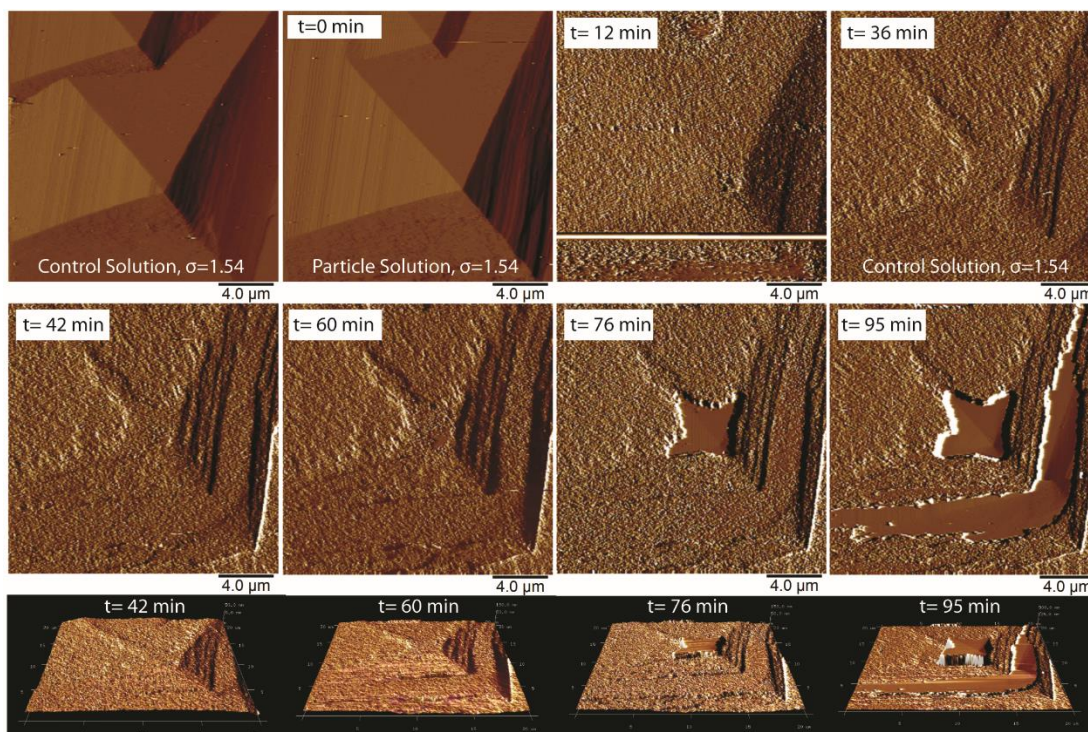


**Figure 3.9:** A film is formed on the crystal surface after the particles are added (t=0). Subsequently, growth apparently proceeds along the hillock peak and ridges while particles are present (t=36 min) and accelerates under control growth conditions (t=36 min to t=60 min). The original hillock recovers, maintaining its rhombohedral

morphology in a hopper-like region ( $t=76$  min to  $t=95$  min). Growth proceeds rapidly upon hillock recovery ( $t=60$  min to  $t=95$  min). The 3D images at bottom visualize the apparently rapid vertical growth upon hillock recovery from 60 to 95 min. Growth at  $\sigma=1.54$  (2.2 mM  $\text{Ca}^{2+}$ ) and .00075%wt nanoparticles.

There are several possibilities to explain the complex binding behavior observed in Figures 8 and 9. The permanency of the micelle binding on first glance seems to be dependent on the distance between the binding site and the hillock peak or ridge. Particles further from the peaks and ridges apparently fully halt growth while those further up do not (Fig. 9). The hillock peak and upper ridges have locally high curvature relative to areas of continuous step flow, so the acidic stabilizer chains cannot form as many bonds with the surface (Figure 10). Less surface binding makes the stabilizers more permeable to growth ions and ion pairs, so there is a local increase in the fraction of particles that “hover” on the surface as the hillock peak and ridges continue to grow. The modified morphology of the final hillock resembles the “hopper-like” bulk crystal morphology that is known to form in the presence of some additives, and this mechanism could explain their formation.<sup>26,27</sup> Further, it is also common in bulk crystal growth for single crystals modified by acidic additives to take on a “bullet-like” shape with  $\{104\}$  faceted end caps connected by a roughened cylinder with macro-steps (multiple step high edges) covering it.<sup>28,29</sup> A local geometry dependent binding mechanism as described here could also help explain this increase

in roughening and apparent increase in macrostep formation in single crystals.

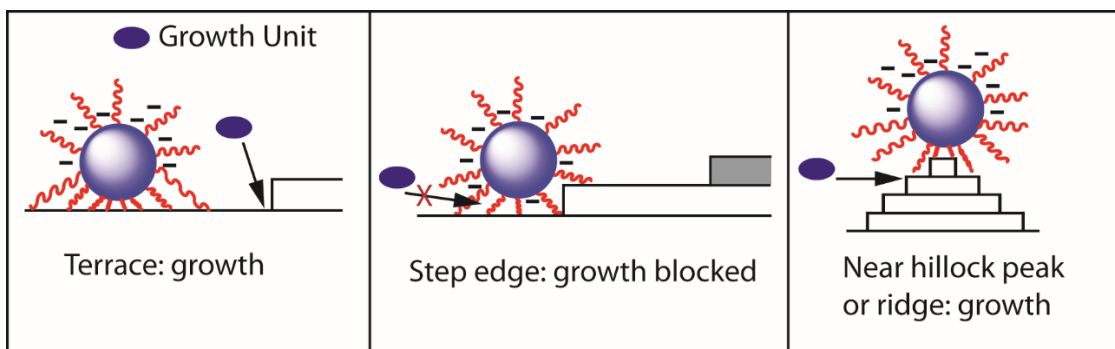


**Figure 3.10:** When on a terrace or bound to a step edge, the polymer nanoparticle locally blocks growth unit access, preventing growth. However, in an area of locally high curvature such as a peak or ridge, the stabilizer chains are more permeable and growth units can access the kink sites.

### 3.4 Conclusions

We have shown that for nanoparticles with long polymeric stabilizer chains, two general regimes of particle-crystal surface interaction exist. If the stabilizer chains are polyelectrolyte in character the particle-crystal interaction is *particle driven* and will be dominated by the structure of the charge corona. At higher divalent cation concentrations the charge corona is more likely to enter the collapsed state, which enhances attachment and incorporation into the crystal. If the stabilizer chains are not polyelectrolytes, the particle-crystal interaction will instead be *surface driven*, and as such dependent on the local surface environment. For calcite in particular, an increase in the disruption and dehydration of bound waters on the calcite surface by an increase in ion concentration is most likely the determining factor in the *surface driven* case. We have further demonstrated that the bonding of polyelectrolyte nanoparticles is

complicated by local surface geometry, where near hillock peaks and ridges particles are more likely to hover on the surface and allow growth to proceed while areas of only step flow will have growth halted. Such limiting of growth can help explain macrostep formation and the “bullet-like” morphologies observed in bulk calcite growth with highly anionic polymeric nanoparticles. The interaction regimes we propose enhance our understanding of the ensemble behavior of particle-crystal interactions and that nanoscale understanding using *in situ* AFM can inform bulk crystal growth experiments. More generally, we confirm that *both* surface chemistry and growth conditions are key for driving nanoparticle-crystal interactions.

### **3.5 Methods**

#### *3.5.1 Nanoparticle Synthesis*

The synthesis of PMAA and PGMA macro-CTAs via RAFT solution polymerization was similar to methods described elsewhere.<sup>6,29</sup> Similar PBzMA-core nanoparticles were recently synthesized via RAFT emulsion polymerization by Armes and co-workers.<sup>30</sup>

#### *3.5.2 Dynamic light scattering and Zeta Potential*

Dynamic light scattering (DLS) and zeta potential measurements were performed at 25°C using a Zetasizer Nano-ZS instrument (Malvern) at a fixed scattering angle of 173°. Copolymer dispersions were diluted in DI water before the addition of ion containing solutions. The ionic solutions were diluted from 1 M stock solutions of CaCl<sub>2</sub> (CaCl<sub>2</sub>·2H<sub>2</sub>O, 99%/ACS Reagent, Sigma Aldrich) and NaCl (Sodium Chloride,

100%/ACS Reagent, JT Baker). Aqueous dispersions were adjusted to pH 9 using KOH.

### 3.5.3 *In Situ Calcite Growth*

*In situ* calcite growth experiments were performed using a method similar to that previously reported by this group (Chapter 2) and that of Cho et al.<sup>17</sup> Briefly, a freshly cleaved geologic calcite {104} surface (Iceland Spar, Ward's Scientific) is glued using epoxy to an AFM sample disk and mounted in the AFM. The surface is imaged dry (~3 Hz imaging rate, 256 samples/line, contact mode) to find an area with minimal surface roughness, making nucleation of hillocks more likely. Then a control (1.8 mM Ca, 3.6 mM NaCO<sub>3</sub>, 18.6 MΩ DI water) solution is flowed over the surface and imaging proceeds to find a hillock which is separated and stable. A syringe pump (Harvard Apparatus) controls solution flow at 0.3 mL/min at room temperature. Then the growth solution is changed to the supersaturation or ionic strength of interest without any nanoparticles. Finally, a final solution change to one with the nanoparticles present (5 μL of “neat” 15 wt/v% particles per 100 mL of growth solution) is made. Experiments were performed using a Multimode III AFM (Veeco Instruments) with a fluid flow cell (Bruker) and a Nanoscope III controller (Digital Instruments). Images were analyzed and processed using Nanoscope Analysis software (Bruker).

### 3.5.4 *Image Analysis*

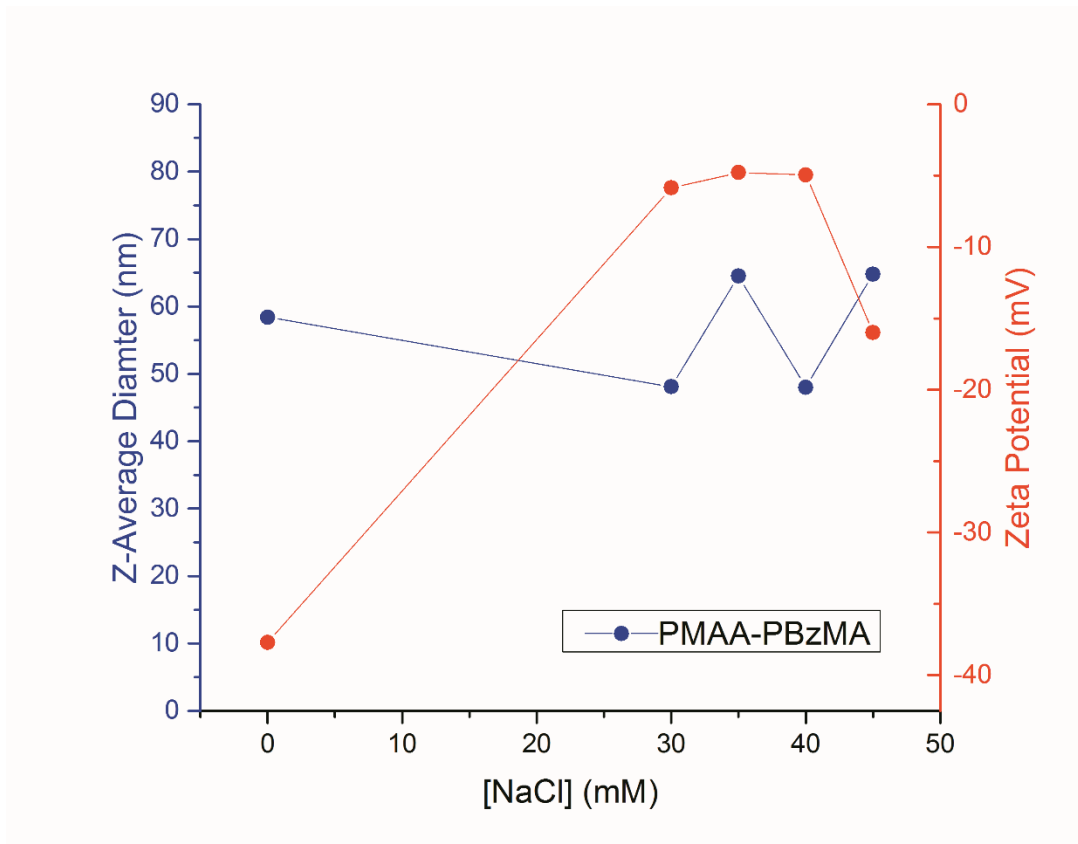
Images were processed using Nanoscope Analysis and FIJI (Image J) software. An example series of images for the area of coverage can be seen in Supplementary

Figure 2. First, the deflection images were set to the same scale ( $\pm 20$  mV). Then they were imported into FIJI and cropped to only include the original image area. For easier thresholding we converted the images to 8 bit grayscale. We then chose a threshold (in this case 90) which maximized the particle area without selecting non particle features on the crystal surface. The same threshold was applied to all images. Finally, the Particle Analysis feature measured the particle surface coverage by percent. This procedure was repeated for five images per experiment and the data averaged. We report the mean with the error of one standard deviation above and below.

### ***3.6 Acknowledgements***

Thanks to Rachel Connelly for performing the zeta potential measurements. This work was funded by a joint National Science Foundation (NSF) and EPSRC Materials World Network (MWN) grant (DMR 1210304 and EP/J018589/1). This work made use of the Cornell Center for Materials Research Shared Facilities which are supported through the NSF MRSEC program (DMR-1120296). We thank the Wiesner group at Cornell for the shared use of their AFM. SPA acknowledges a five-year ERC Advanced Investigator grant (PISA 320372) and EPSRC support.

### 3.7 Supplementary



**Figure 3.11(S1):** Diameter and zeta potential of PMAA-PBzMA nanoparticles with increasing [NaCl] measured at pH 8 (set using KOH). There is a limited effect on the PMAA-PBzMA diameter. NaCl was diluted from 1 M stock solution (NaCl 100% ACS Reagent, JT Baker).

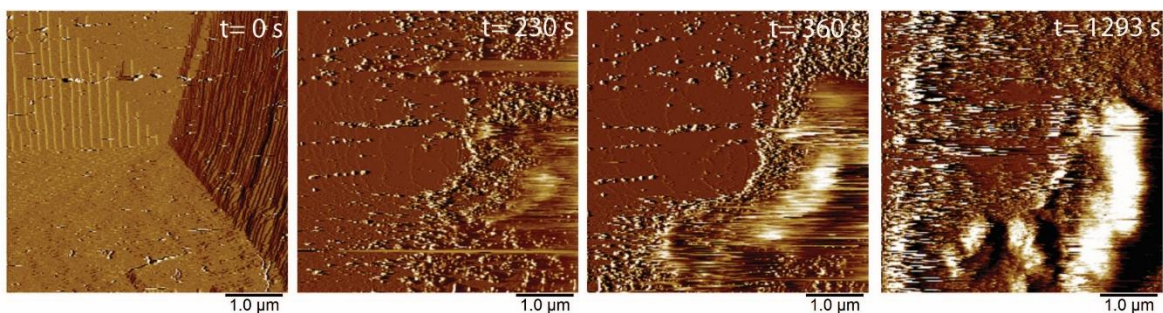


**Figure 3.12(S2)** A time series for PMAA-PBzMA particles at the highest supersaturation ( $\sigma=1.54$ ). The particles attach densely and eventually form a film on the surface.

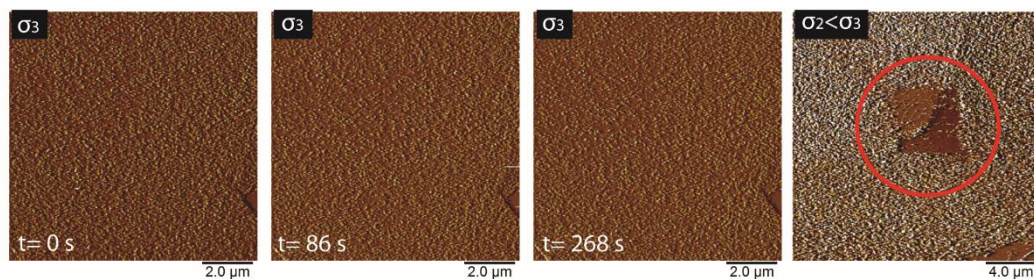


**Figure 3.13(S3):** The polymer film formed at high supersaturation ( $\sigma=1.54$ ) by the PMAA-PBzMA particles is unaffected by the tip. At lower supersaturations the tip always moved some population of the particles to the edges of the imaging area (red circle).

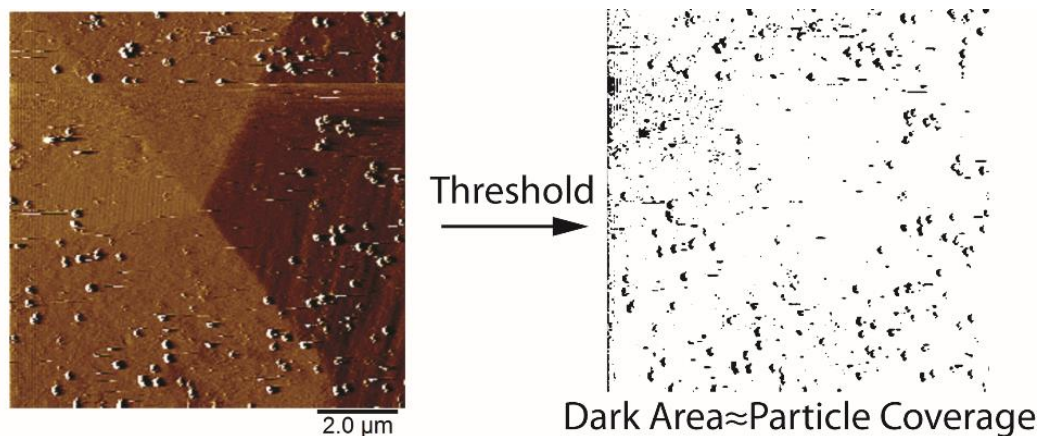


**Figure 3.14(S4):** Visualization of particle analysis procedure. See Methods for details.

A deflection image is set to 20mV scale, then the image is thresholded to ensure only particles are selected. Finally the thresholded area is measured.

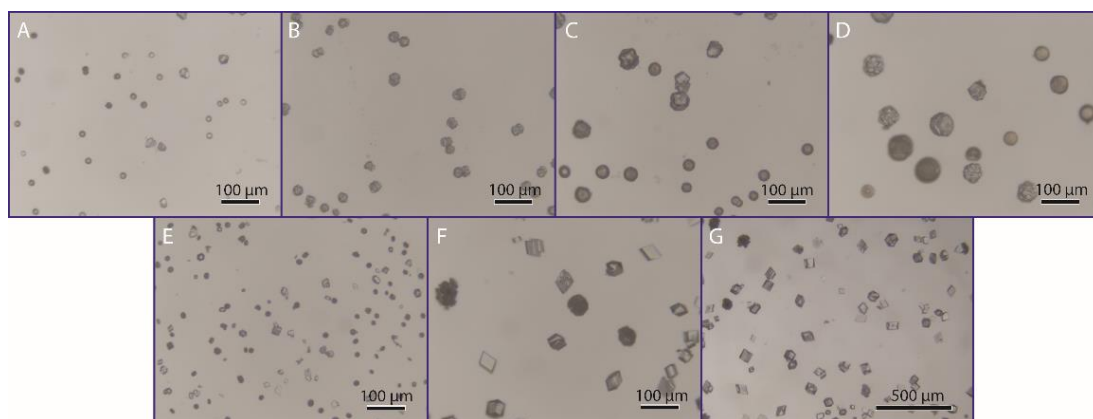


**Figure 3.15(S5):** Ex situ growth with PMAA-PBzMA particles at initial calcium concentrations of: (A) 1 mM, (B) 2 mM, (C) 5 mM, (D) 10 mM and control growth without particles at (E) 1 mM, (F) 5 mM, (G) 10 mM. The crystals grown at higher  $\sigma$  and with the nanoparticles appear to have fewer single crystals and more polycrystals

and non-calcite polymorphs of  $\text{CaCO}_3$  (XRD Fig. S7). The particle concentration is 0.75 %wt.

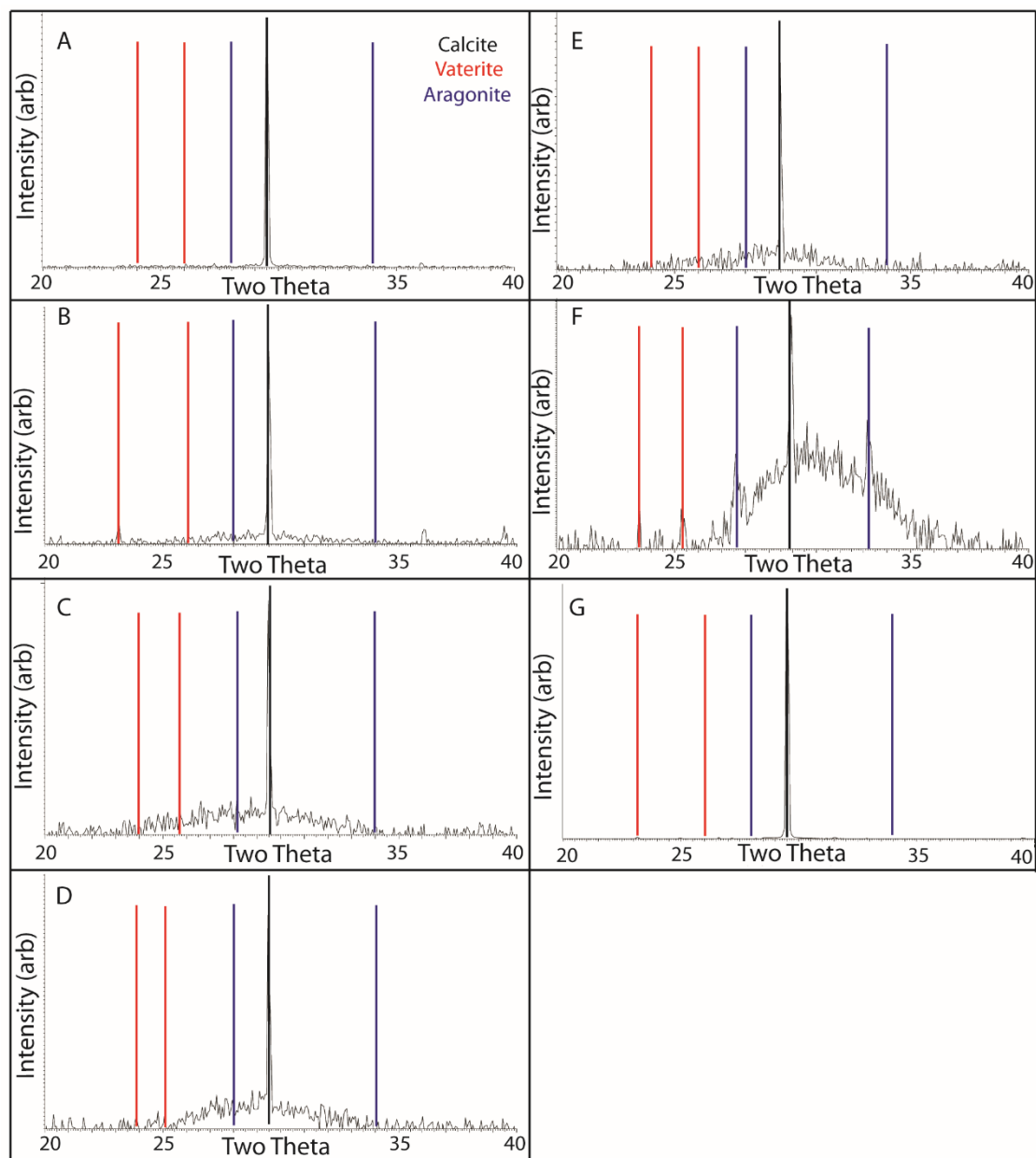


**Figure 3.16(S6):** XRD patterns corresponding to samples of Figure S6. We observe an increase in polycrystals of calcite and other phases at higher  $\sigma$  and when polyelectrolyte nanoparticles are present. *Ex situ* growth was performed using the

ammonium diffusion method with  $[\text{CaCl}_2]$  as listed in Figure S4 and particle concentration 0.75% wt.

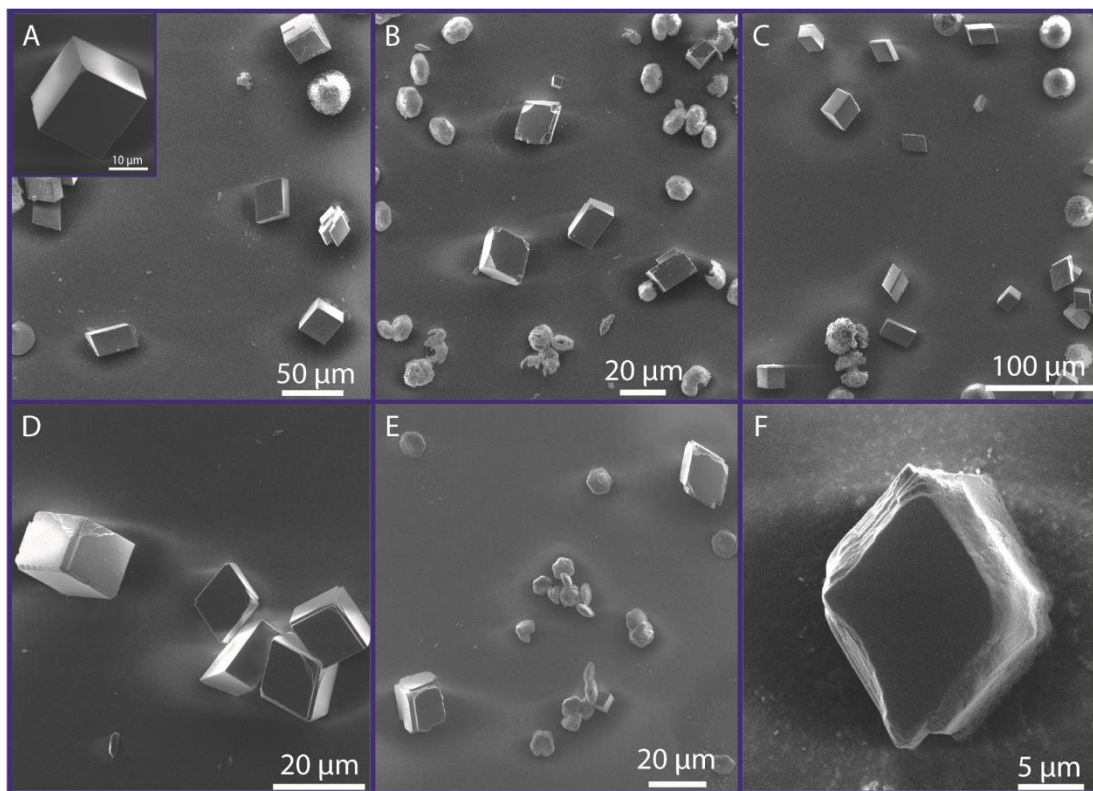


**Figure 3.17(S7):** (A inset) control calcite growth at 5 mM  $[\text{Ca}^{2+}]$ . (A-C) calcite growth with increasing  $[\text{Na}^+]$  of (A) 5 mM, (B) 100 mM, (C) 500 mM. (D-F) calcite growth in the presence of 0.75% wt of HOOC-PGMA-PBzMA nanoparticles at  $[\text{Na}^+]$  of (D) 5mM, (E) 100 mM and (F) 500 mM. Increased rounding and roughening of single crystal edges and facets in the presence of nanoparticles indicates increased interaction, as predicted by the *in situ* experiments.

## REFERENCES

- (1) Qiu, S. R.; Orme, C. A. *Chemical Reviews*, 2008, 4784.
- (2) Chen, C.-L.; Qi, J.; Tao, J.; Zuckermann, R. N.; DeYoreo, J. J.; *Sci. Rep.* 2014, 4, 6266.
- (3) Metzler, R. A.; Tribello, G. A.; Parrinello, M.; Gilbert, P. U. P. A. *J. Am. Chem. Soc.* 2010, 132 (33), 11585.
- (4) Friddle, R. W.; Weaver, M. L.; Qiu, S. R.; Wierzbicki, A.; Casey, W. H.; De Yoreo, J. J. *Proc. Natl. Acad. Sci. U. S. A.* 2010, 107 (1), 11.
- (5) Chen, C.-L.; Qi, J.; Zuckermann, R. N.; DeYoreo, J. J. *J. Am. Chem. Soc.* 2011, 133 (14), 5214.
- (6) Kim, Y.-Y.; Ganesan, K.; Yang, P.; Kulak, A. N.; Borukhin, S.; Pechook, S.; Ribeiro, L.; Kröger, R.; Eichhorn, S. J.; Armes, S. P.; Pokroy, B.; Meldrum, F. C. *Nat. Mater.* 2011, 10 (11), 890.
- (7) Muñoz-Espí, R.; Qi, Y.; Lieberwirth, I.; Gómez, C. M.; Wegner, G.; *G. Chem. - A Eur. J.* 2006, 12 (1), 118.
- (8) Wegner, G.; Demir, M. M.; Faatz, M.; Gorna, K.; Munoz-Espi, R.; Guillemet, B.; Gröhn, F. *Macromol. Res.* 2007, 15 (2), 95.
- (9) Kim, Y.-Y.; Schenk, A. S.; Walsh, D.; Kulak, A. N.; Cespedes, O.; Meldrum, F. C. *Nanoscale* 2014, 6 (2), 852.

- (10) Wegner, G.; Demir, M. M.; Faatz, M.; Gorna, K.; Munoz-Espi, R.; Guillemet, B.; Gröhn, F.; Marriage, I. A. H.; Wegner, G.; Demir, M. M.; Faatz, M.; Gorna, K.; Munoz-Espi, R. *Macromol. Res.* 2007, 15 (2), 95.
- (11) Rafael Muñoz-Espí; Amreesh Chandra; Wegner, G. *Crystal Growth and Design*, 2007, 7(9), 1584.
- (12) Ning, Y.; Fielding, L. A.; Ratcliffe, L. P. D.; Wang, Y.-W.; Meldrum, F. C.; Armes, S. P. *J. Am. Chem. Soc.* 2016, 138 (36), 11734.
- (13) De La Pierre, M.; Raiteri, P.; Gale, J. D. *Cryst. Growth Des.* 2016, 16 (10), 5907.
- (14) Rodriguez-Navarro, C.; Burgos Cara, A.; Elert, K.; Putnis, C. V.; Ruiz-Agudo, E. *Cryst. Growth Des.* 2016, 16 (4), 1850.
- (15) Poloni, L. N.; Ward, M. D. *Chem. Mater.* 2014, 26 (1), 477.
- (16) Olafson, K. N.; Ketchum, M. A.; Rimer, J. D.; Vekilov, P. G. *Cryst. Growth Des.* 2015, 15 (11), 5535.
- (17) Cho, K.R.; Kim, Y.-Y.; Yang, P.; Cai, W.; Pan, H.; Kulak, A. N.; Lau, J. L.; Kulshreshtha, P.; Armes, S. P.; Meldrum, F. C.; De Yoreo, J. J. *Nat. Commun.* 2016, 7, 10187.
- (18) Parnell, A. J.; Martin, S. J.; Dang, C. C.; Geoghegan, M.; Jones, R. A. L.; Crook, C. J.; Howse, J. R.; Ryan, A. J. *Polymer (Guildf)*. 2009, 50 (4), 1005.
- (19) Minko, S. J. *Macromol. Sci. Part C Polym. Rev.* 2006, 46 (4), 397.
- (20) Mei, Y.; Ballauff, M. *Eur. Phys. J. E* 2005, 16 (3), 341.
- (21) Guo, X.; Ballauff, M.; *Langmuir*. 2000, 16 (23), 8719.

- (22) Yoreo, J. J. De; Vekilov, P. G. Principles of Crystal Nucleation and Growth, 2003.
- (23) Stephenson, A. E.; Hunter, J. L.; Han, N.; DeYoreo, J. J.; Dove, P. M. Geochim. Cosmochim. Acta 2011, 75 (15), 4340.
- (24) Ruiz-Agudo, E.; Putnis, C. V.; Wang, L.; Putnis, A. Geochim. Cosmochim. Acta 2011, 75 (13), 3803.
- (25) Araki, Y.; Tsukamoto, K.; Takagi, R.; Miyashita, T.; Oyabu, N.; Kobayashi, K.; Yamada, H. Cryst. Growth Des. 2014, 14 (12), 6254.
- (26) Dickinson, S. R.; McGrath, K. M. J. Mater. Chem. 2003, 13 (4), 928.
- (27) Yu, J.; Lei, M.; Cheng, B.; Zhao, X. J. Solid State Chem. 2004, 177 (3), 681.
- (28) Orme, C. A.; Noy, A.; Wierzbicki, A.; McBride, M. T.; Grantham, M.; Teng, H. H.; Dove, P. M.; DeYoreo, J. J. Nature 2001, 411 (6839), 775.
- (29) Kim, Y.-Y.; Semsarilar, M.; Carloni, J. D.; Cho, K. R.; Kulak, A. N.; Polishchuk, I.; Hendley, C. T.; Smeets, P. J. M.; Fielding, L. A.; Pokroy, B.; Tang, C. C.; Estroff, L. A.; Baker, S. P.; Armes, S. P.; Meldrum, F. C. Adv. Funct. Mater. 2016, 26 (9), 1382.
- (30) Derry, M. J.; Fielding, L. A.; Armes, S. P. Polym. Chem. 2015, 6 (16), 3054.

## CHAPTER 4

# A SURVEY OF HILLOCK-HILLOCK INTERACTIONS USING *IN SITU* ATOMIC FORCE MICROSCOPY (AFM): FRAMEWORK FOR LINKING NANOSCALE TO MACROSCALE GROWTH

### ***4.1 Introduction***

The history of crystallography is filled with studies that attempt to fundamentally characterize growth from the nanoscale to the macroscale with a particular emphasis on growth from melt and vapor. However, direct observation of nanoscale growth mechanisms in solution has only been made possible relatively recently with the development of the Atomic Force Microscope (AFM) and other advanced optical imaging techniques.<sup>1,2</sup> Such *in situ* solution studies have revealed nanoscale growth mechanisms such as: hillock growth around a screw dislocation, 2D island growth, and deposition of particles from solution.<sup>3-6</sup> These mechanisms, long believed to exist in theory have now been directly observed in a wide variety of crystal systems in solution and provide an excellent opportunity to study nanoscale growth kinetics.<sup>3,5-15</sup> For poorly soluble materials, AFM studies control the solution conditions such that only hillock growth is observed on a growing crystal surface because growth around the hillock can be conveniently quantified to understand the growth kinetics both under a variety of control growth conditions and in the presence of additives (see Chap. 2 and 3 for examples of such studies).<sup>16</sup> In principle, hillock characteristics such as the slope, step velocity, and step spacing (terrace width) can all vary with solution conditions and/or with additive type and concentration. Significantly, multiple studies have phenomenologically linked hillock morphology to

bulk crystal morphology.<sup>9,13,14,17</sup> For crystals in which a single growth hillock dominates the surface, it is intuitively straightforward to understand how hillock morphology leads to crystal morphology.<sup>18</sup> Once there are multiple dislocations on a surface, however, the growth is more complex. Multiple hillocks growing on a single crystal can interact, and how they may overlap and combine to result in the well-studied bulk morphologies remains poorly understood. This work provides a framework for understanding hillock-hillock interactions and presents a variety of interactions which have been observed *in situ* on calcite.

A few crystal systems have been extensively characterized using *in situ* AFM, especially calcite ( $\text{CaCO}_3$ ), KDP (Potassium diphosphate), COM (Calcium Oxalate Monohydrate), L-cysteine and a variety of protein systems.<sup>3,4,7-9,16,19-24</sup> Perhaps the best characterized crystal in terms of hillock properties is KDP.<sup>4,19,25-29</sup> DeYoreo and coworkers were the first to extensively characterize KDP hillock growth at the nanoscale.<sup>4,19,25</sup> They showed that for the  $\{101\}$  facets, growth could occur via dislocation induced step flow (hillock) or a 2D island growth mechanisms.<sup>4,19</sup> In surprising contrast, on the  $\{100\}$  facet both the slope and step spacing are supersaturation dependent, demonstrating that nanoscale growth kinetics are facet related.<sup>11,19</sup> Growth on KDP can be suppressed by additives in the solution, and when the additives are removed from solution, growth recovers. A classical picture would predict that growth would resume with the same mechanisms as before the additive was present. However, *in situ* data shows that in fact macrosteps (multi-step high units) facilitate growth recovery, implying there are additional features to account for

in understanding additive-crystal interaction.<sup>26</sup> Even for a well-studied system such as KDP at the nanoscale, there is surprising complexity in the growth mechanisms.

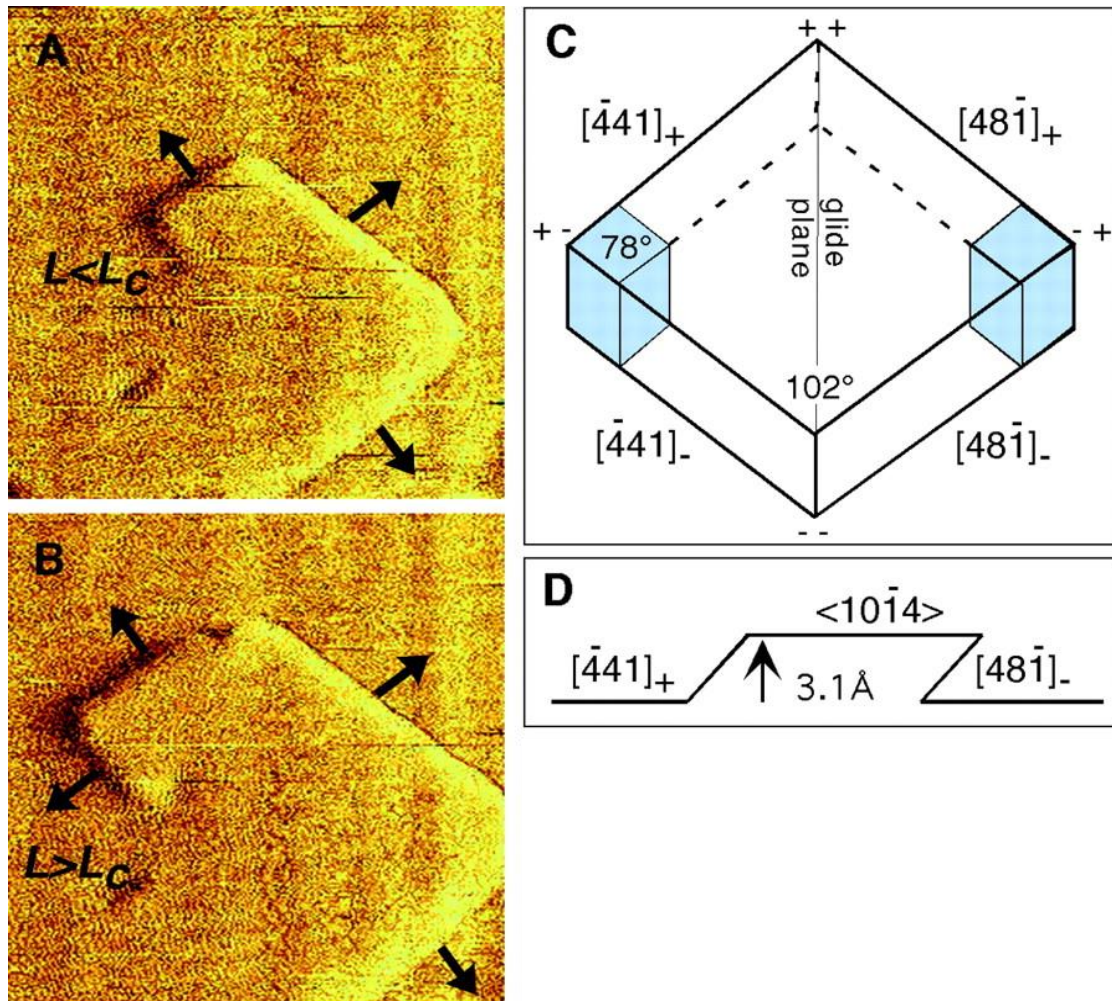


**Figure 4.1:** Generation of a new step edge from a dislocation source once the edge length  $L$  exceeds the critical length  $L_c$  required for propagation (A and B). The rhombohedral symmetry of calcite results in anisotropy on terraces and two distinct step edges (C and D). From “Teng H.H., Dove P.M., Orme C.A., De Yoreo J.J., “Thermodynamics of Calcite Growth: Baseline for Understanding Biomineral Formation,” *Science*, 1998, 282, 5389.” Reprinted with permission from AAAS.

In the case of calcite, much is known about individual hillock growth, in particular step velocity behavior under the influence of a variety of additives, as well as a function of supersaturation.<sup>3,6,13–15,30–37</sup> Calcite has a rhombohedral symmetry (Figure 1C), resulting in two distinct types of step edge on the crystal surface during growth (obtuse + and acute -, Figure 1D).<sup>3,18</sup> Most notably, calcite step growth is kink-limited, meaning that under control conditions the factor most limiting growth is generation of new kink sites on the step edge.<sup>15</sup> Further, step edges only flow from the dislocation source after the edge has reached a critical length ( $L_c$ , Figure 1A and 1B). Additionally, the height of an individual step will always be one unit cell (Figure 1D), but the dislocation source can be multiple Burgers vectors in size.<sup>16</sup> Thus, multiple step unit high edges and hillocks can be generated on the calcite surface, typically “double” (two Burgers vectors and two steps high) or “triple” (three Burgers vectors and three steps high) step edges.<sup>16</sup> Upon the injection of additives into the growth, the kinetics and morphology of the hillock is modified. Orme and DeYoreo were the first to show that additives interacting with calcite directly modified the hillock morphology, and that the modified hillock mimics the morphology of a bulk grown crystal (Figure 2).<sup>13,17</sup> Such a modified individual hillock can also be seen in Chapters 2 and 3 when growth occurs in the presence of a polyelectrolyte nanoparticle (as well as Figure 2 for various molecular additives). Such variation in morphology, especially in the presence of additives, is of significant interest to the biomineral community because understanding additive-crystal interactions helps us both further understand biology and inform new synthetic methods for single crystal growth. *In situ* AFM has been especially useful in this field because of the large variety of possible additive-

crystal interactions. To date, however, the focus has been on studying the thermodynamics and kinetics of single hillocks growing on the surface. To more fully probe the development of calcite growth from the nanoscale to the macroscale requires a more wide ranging analysis using *in situ* AFM. In particular, capturing multiple hillocks interacting over long time periods can help to understand how the final morphology of the crystal is established. Here, I report a survey of a variety of hillock-hillock interactions and present a few case studies that demonstrate the types of interactions that are possible.

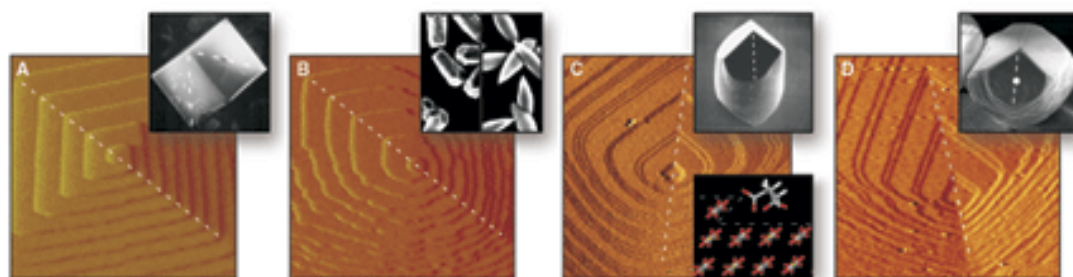


**Figure 4.2:** The empirical connection between individual nanoscale growth hillocks and bulk crystal morphology. (A) A control growth calcite crystal and hillock with no additive present. (B) Calcite grown in the presence of  $Mg^{2+}$ . SEM reprinted with permission from Han and Aizenberg.<sup>38</sup> (C) Calcite growth with the amino acid D-Aspartic acid. Reprinted with permission from Orme et. al.<sup>13</sup> (D) Calcite growth with the protein AP8 extracted from the nacreous layer of the mollusk abalone. Reprinted with permission from Fu et. al.<sup>39</sup> Figure reprinted with permission from “De Yoreo J.J., Dove P.M., Shaping Crystals with Biomolecules, *Science*, 2004, 306, 5700, 1302-1302.”<sup>17</sup>

## ***4.2 Results and Discussion: Categorizing Hillock-Hillock Interactions***

### ***4.2.1 Burgers vector length (“Single” or “Double” Hillock) and step annihilation***

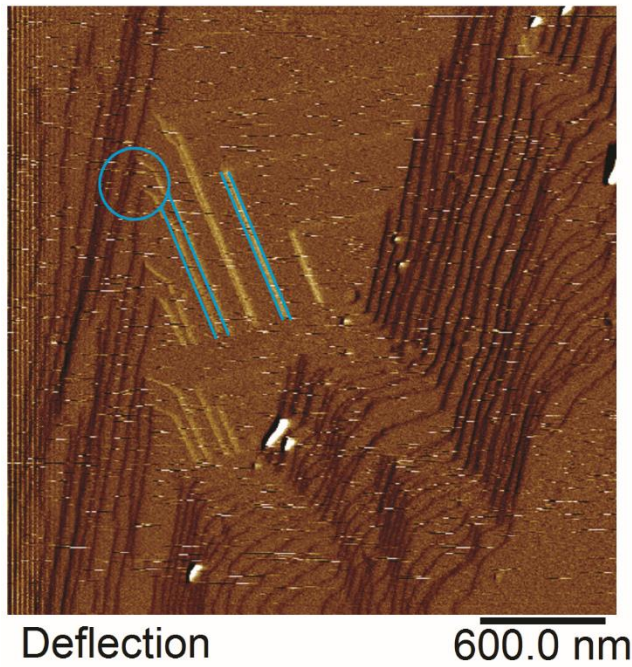


**Figure 4.3:** A “double” hillock generating two unit high edges intersects the steps from a “single” Burgers vector source. The double high steps (blue lines) neatly annihilate two single high steps each (blue circle), as expected from classical theory. Growth at  $\sigma=1.15$ ,  $[\text{Ca}^{2+}] = 1.8 \text{ mM}$ .

Hillocks are generated from screw dislocations, and they can have different Burgers vector lengths. It has previously been demonstrated that on the same calcite face screw dislocations with different Burgers vectors can be in close proximity.<sup>16</sup> Most hillocks are one growth unit high because one unit dislocations are lower in energy, but some can be more than one unit high (Fig. 3). When steps from different sources intersect, they will annihilate each other and form a flat terrace (Fig. 3). If one source is twice as high, the higher step edge will naturally dominate the smaller, because it overlaps the single step source 2:1 (Fig. 3). Therefore, sources that generate

multiple step unit-high edges will dominate their local growth region, but those regions will be relatively infrequent on the crystal surface, because they are relatively high energy. A more complete experimental survey of growing calcite surfaces could test this concept and reveal the true frequency of the different hillock types.

#### 4.2.2 Relative height

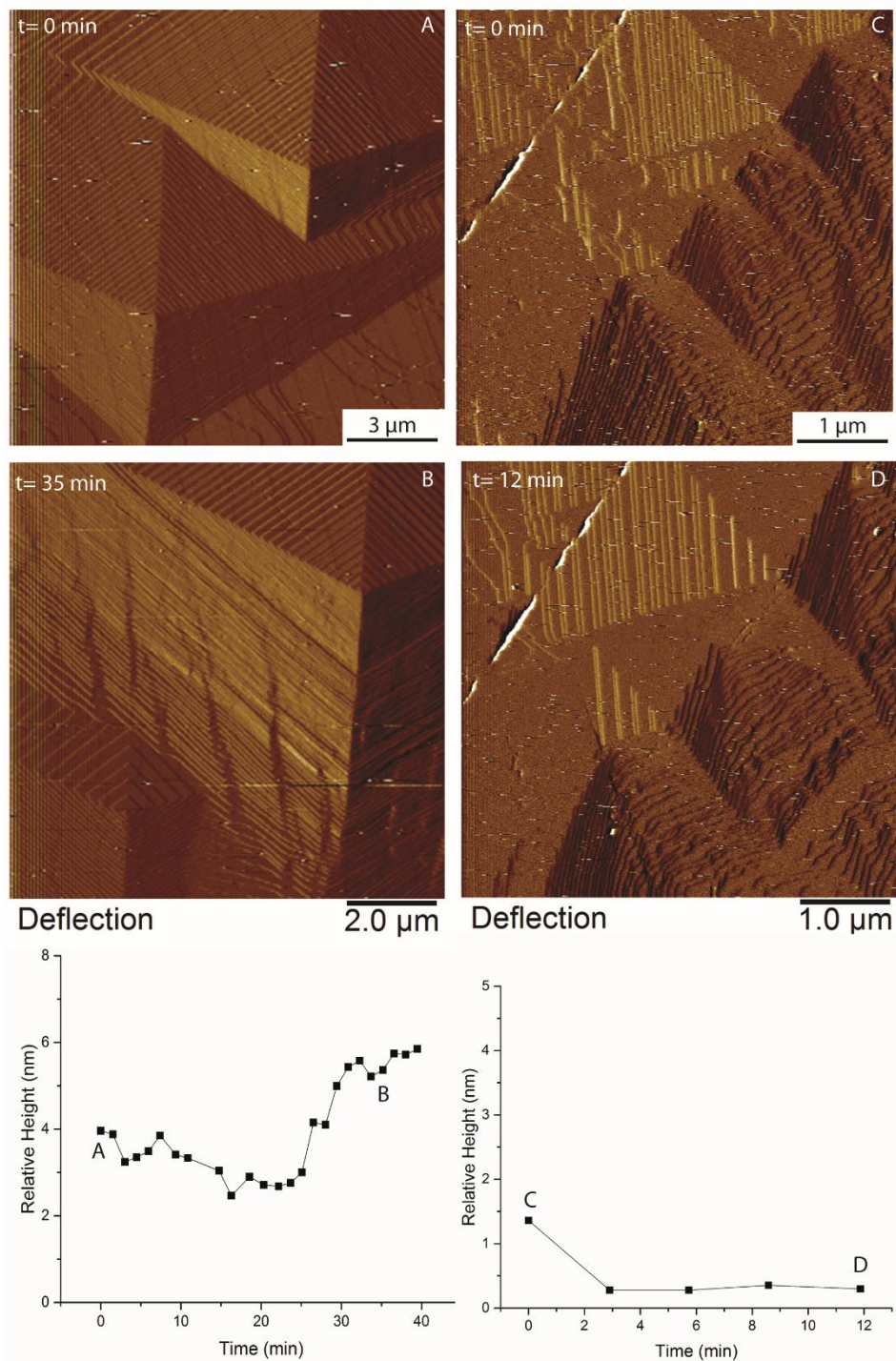


**Figure 4.4.** Images and corresponding relative height over time for two different hillock pairs. A and B exhibit a surprising instability after ~25 min, where one hillock suddenly accelerates in growth relative to the other, beginning an overgrowth process.

C and D demonstrate the expected classical behavior of the two hillocks growing in parallel over time. C and D were imaged over a shorter time, so could enter the unstable growth state later. Growth at  $\sigma=1.15$ ,  $[\text{Ca}^{2+}] = 1.8 \text{ mM}$ .

A truly classical growth picture would suggest that for a given pair of hillocks of the same Burgers vector, they should remain the same relative height as they both grow in parallel upward (Fig. 4, A and B for  $t < 25 \text{ min}$ , C and D for all observed time). However, this is not always the case. Often, one hillock will accelerate in height relative to the other such that the taller of the two hillocks overgrows the smaller, even when both are “single” hillocks (Fig. 4, A and B for  $t > 25 \text{ min}$ ). The hillock stability appears to have a time dependence as well. Over a shorter timescale the growth appears classical, but at longer timescales ( $> 25 \text{ min}$ ) the instability emerges. This observation implies some inherent local instability exists, with a variety of possible explanations. Chernov observed that subtle variations in hillock slope led to relative domination of one hillock over another for ADP (ammonium dihydrogen phosphate).<sup>2</sup> He also showed that the hillock hierarchy could be manipulated by changing supersaturation.<sup>2</sup> The slopes of calcite hillocks are not well studied, so this could help explain the instability. Another possibility is the adsorption of growth units through the hydration layers on the calcite surface. The two (or more) bound layers of water on the surface act as a barrier to growth, which makes growth unit adsorption a complex process.<sup>40,41</sup> Multistep adsorption implies there is some variability in the attachment time for a growth unit. Additionally, we are observing growth at relatively low supersaturation (typically  $\sigma = 1.14$ ) and as such, it is possible that variation in growth unit attachment could lead to local depletion of growth units, starving one hillock

while feeding another. The observed instability could also be explained by attachment of contaminants near the step edge, which might disrupt the hydration layer and accelerate kink site generation, accelerating growth for one hillock in favor of another. With more relative height data like those in Fig. 4, an average hillock lifetime could be deduced at various growth conditions, which could provide more detailed kinetic insights. The local instability we observe is also probably dependent on the hillock separation, and there is most likely a maximum separation beyond which the hillocks no longer “interact.”

#### *4.2.3 Step edge curvature and hillock spacing*

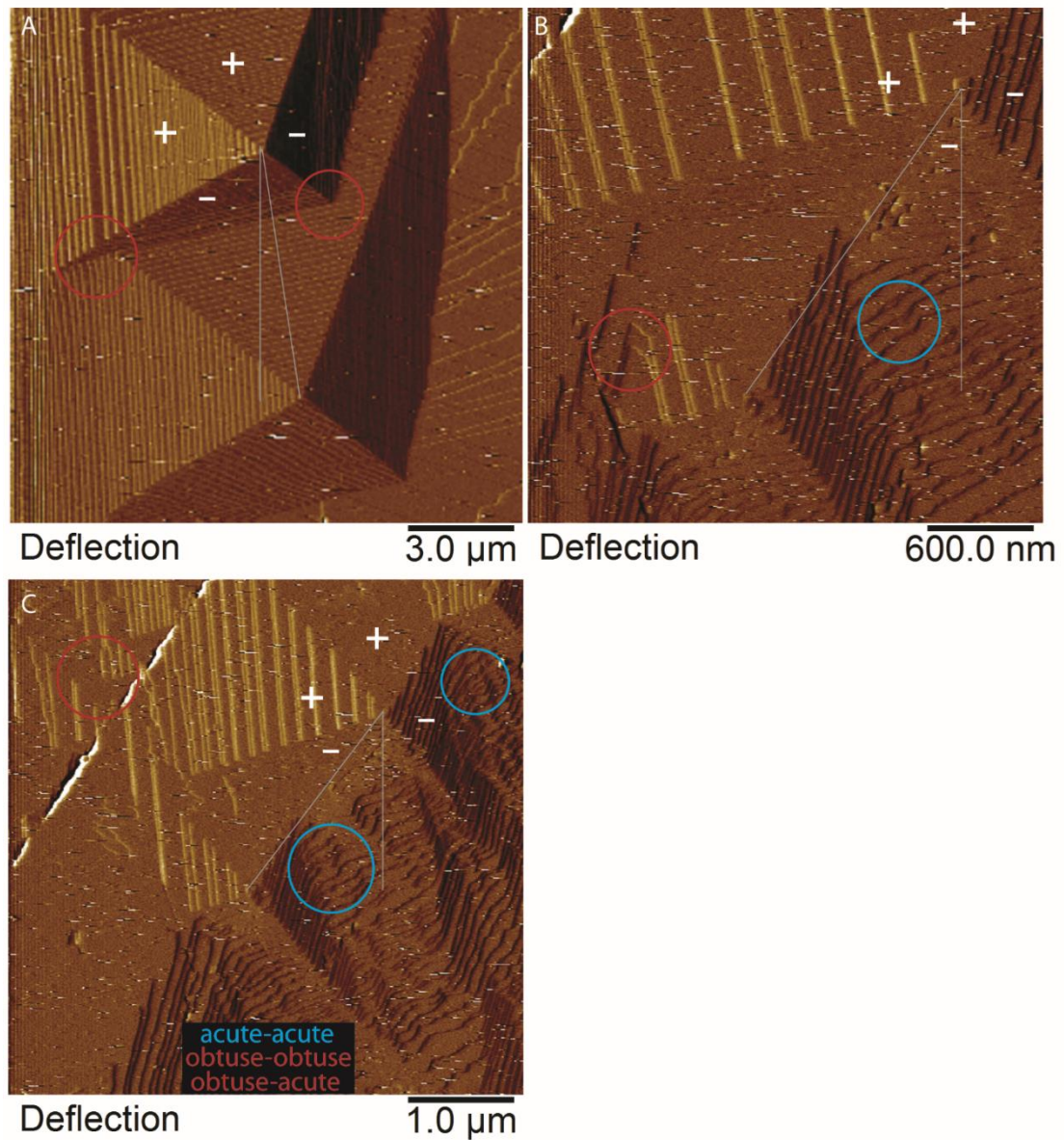


**Figure 4.5:** Curvature varies depending on the type of steps interacting and apparently on the hillock offset/separation. A: two hillocks nearly perfectly aligned have very little curvature between their step edges. B: A larger offset between the hillock peaks leads to different step edges interacting. Even when an acute and obtuse edge directly intersect (red), a single sharp corner remains, indicating a single kink site. C: It appears that only the acute-acute interactions (blue) generate kink sites and have a

reduced curvature. Non acute-acute interactions (red) retain high curvature and a limited number of kink sites. Growth at  $\sigma=1.15$ ,  $[\text{Ca}^{2+}] = 1.8 \text{ mM}$ .

Calcite step edges reflect the symmetry of the bulk crystal (Fig. 1). The result is two step edges which form obtuse angles with the surface (Fig. 5, +), and two which form acute angles with the surface (Fig. 5, -)<sup>3</sup>. The angles originate from the angles in the carbonate molecule within the structure. When two different step edges from two different sources intersect, they form a high energy kink site at the point of intersection (Fig. 5B and C, red). These intersections only occur if the hillock cores are sufficiently offset so the step edges are able to intersect one another (gray lines, Fig. 5). When they do intersect, the high energy sites are much more favorable for attachment, and the result is local reduction in curvature, generating even more kink sites (Fig. 5B and C, blue). However, we observe much greater curvature (and fewer kink sites) at obtuse-obtuse intersections and less curvature (and more kink sites) at acute-acute intersections. Such a disparity could arise because the acute and obtuse steps have different local energy landscapes and as such different attachment processes for growth units at each site type<sup>40,41</sup>. Based on this preliminary understanding, one way to potentially manipulate kink site generation and therefore the hillock-hillock interactions is to change the kink site energies through additives.

#### *4.2.4 Additives and Multiple Hillocks*

Previous work has demonstrated several additives that attach preferentially to only acute step edges and change the local kinetics of a single hillock.<sup>13,14,42</sup> Additive effects on individual hillock kinetics are fairly well documented, but their potential

effects on multiple hillock dynamics remains unknown. In the presence of the amino acid Glycine, some surprising effects are revealed (Figure 6). Though the additives preferentially bind to and inhibit growth on the acute step edges, the acute steps not only continue to grow but retain a significant presence on the surface. Further, we know that a macroscopic crystal will have a large rounded section (Figure 2). Therefore the relationship between acute and obtuse steps is surely impacted by the additives, and understanding that change would lead to an improved model for macroscopic crystal formation. When a hillock becomes overlapped with Gly present, it seems that it is not easily completely overgrown. In fact, some of the overlapped hillock remains exposed to growth solution (Figure 6B, red arrow). So all of the step-step interactions are apparently impacted simply by adding Gly. Another unusual observation is the nucleation of new hillocks on the calcite surface in the presence of Glycine (Figure 3C and D, blue). Such a nucleation event on growing calcite has not been reported previously to our knowledge. Can additives themselves nucleate growth hillocks by generating surface defects? In principle it is possible but has yet to be studied in depth. Extensive imaging experiments are required to build a more complete picture of the larger scale impacts of even small molecules on calcite growth.

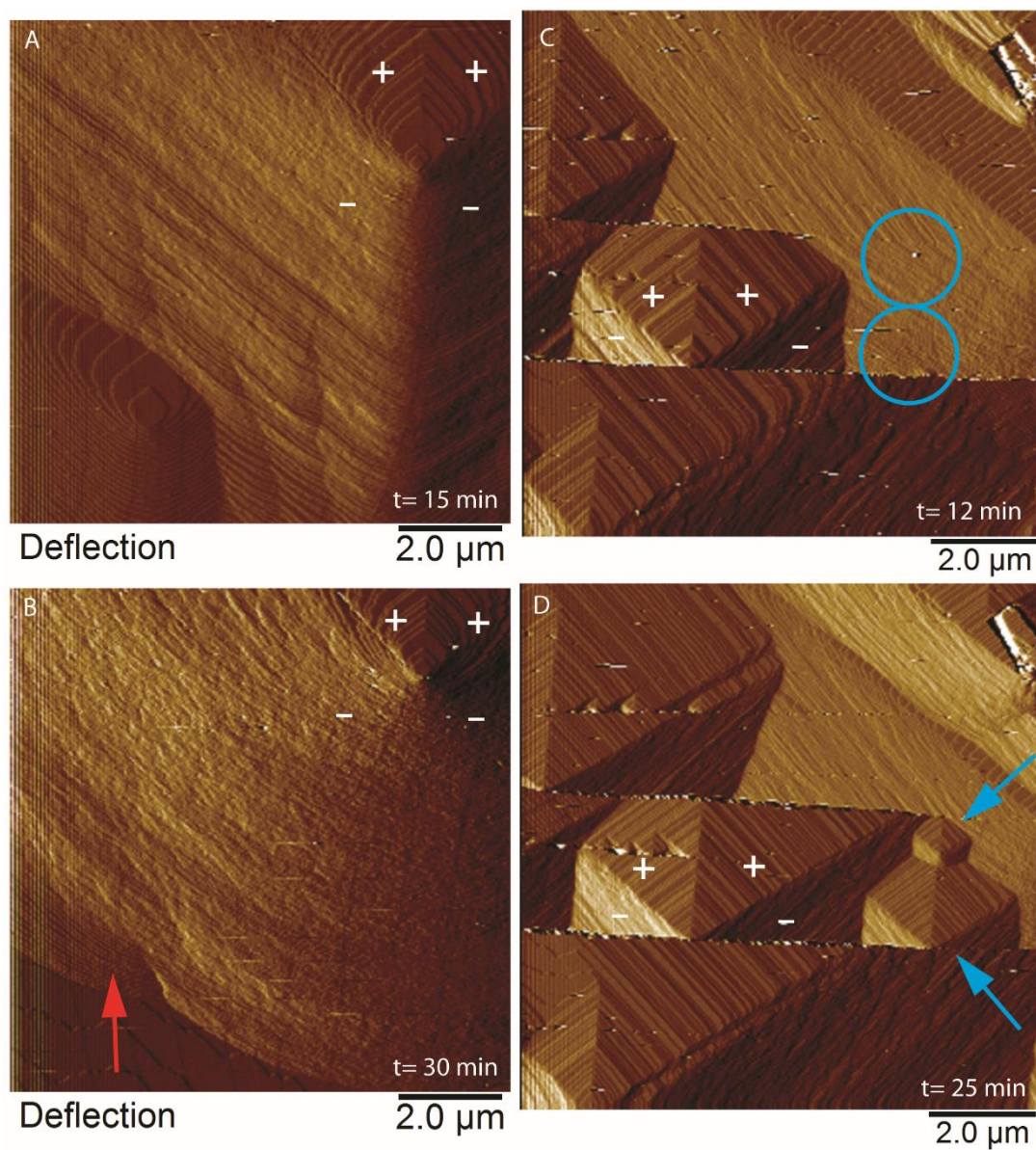


**Figure 4.6.** Two calcite growth experiments illustrating unusual growth behavior with Glycine. (A, B) Two modified hillocks overlap one another. In B, a small remnant of the overlapped hillock appears to protrude from the larger hillock (red arrow). (C, D) Hillocks appear to nucleate mid-growth (blue), revealing additional complexity. The

horizontal lines in C and D are 10s of nm scale surface defects. Growth at  $\sigma=1.15$ ,  $[\text{Ca}^{2+}]=1.8$  mM,  $[\text{Gly}]=1.8$  mM.

#### 4.2.5 Open Questions

With a wide enough survey of calcite crystal surfaces such as those in Figures 3-6 we could map the average hillock type distribution and understand which hillock types dominate the nanoscale to macroscale transition. To achieve such a goal requires longer imaging times to ensure capture of any instabilities (as seen in Figure 4). Further, though hillock-hillock pairs are a useful starting point to understand which hillocks tend to dominate, a true survey requires imaging over even larger areas to observe as many hillocks as possible simultaneously. One could also perform equivalent experiments to those mentioned in this chapter on hillocks grown from *synthetic* calcite. To my knowledge, no such comparison between growth on a geologic and synthetic crystals has ever been published. Synthetic crystals are on the order of 10s of microns in size while geologic crystals are centimeter scale. The dislocation density could vary substantially crystal to crystal, which would change the hillock density on the surface and potentially change the growth. Such a dataset will make answering several important questions possible: (1) does each hillock have an “area of influence” around it? If so, then there is a limit beyond which no hillock-hillock interactions will occur for a hillock of a given size. Such an “area of influence” existing would also imply there are slightly different growth regimes inside and outside that region, one area of “hillock growth” and one of “step flow.” If true, it is an additional complicating factor to our understanding of real crystal surfaces. (2)

Does the growth mode at low supersaturation truly end in a single hillock dominating and forming the crystal? If not, what are the kinetic processes that lead to multiple hillocks equilibrating to form the smooth surfaces characteristic of bulk grown single crystals? (3) How are macrosteps formed on the crystal surface? (4) What is the effect of additives on the ideas presented here? For example, calcite grown with additives often has a “bullet-like” morphology as seen in Figure 2, what is the nanoscale origin of the roughened surface?

### **4.3 Conclusions**

We have chronicled a variety of factors and interactions that can influence growth from the nanoscale to the macroscale as hillocks overlap. We observe previously unreported instability between hillock pairs on calcite, leading to one hillock dominating and overlapping another. The instability could be related to kink generation, relative hillock slope, local supersaturation gradients, or a combination of factors. We also observe curved step edges that are related to the relative offset and spacing between hillock cores. Further, we observe hillocks with different Burgers vector lengths, and the larger step edges dominate the smaller. We have established a framework for further characterizing hillock-hillock interactions, but we have also opened a host of new questions. Answering these questions will provide greater insight into growth both with and without additives. Significant further study is required before we can complete our understanding of real crystal growth.

### **4.4 Methods**

*In situ AFM*

AFM data was collected after our previous methods in Chapters 2 and 3. Briefly, growth solution is flowed through a commercial fluid cell (Bruker) in an AFM operating in contact mode (Multimode III, Veeco Instruments).

#### *Image Processing and Analysis*

Images were processed using the Nanoscope Analysis software (Bruker). Height measurements were conducted within the program and the linescan data exported to Origin to construct the plots.

## REFERENCES

- (1) Tsukamoto, K. *Prog. Cryst. Growth Charact. Mater.* 2016, 62 (2), 111.
- (2) Chernov, A. A.; Rashkovich, L. N.; Mkrtchan, A. A. *J. Cryst. Growth* 1986, 74 (1), 101.
- (3) Teng, H. H.; Dove, P. M.; Orme, C. A.; De Yoreo, J. J. *Science* 1998, 282 (5389).
- (4) De Yoreo, J. J.; Land, T. A.; Rashkovich, L. N.; Onischenko, T. A.; Lee, J. D.; Monovskii, O. V.; Zaitseva, N. P. *J. Cryst. Growth* 1997, 182 (3–4), 442.
- (5) Lupulescu, A. I.; Rimer, J. D. *Science* 2014, 344 (6185), 729.
- (6) Yoreo, J. J. De; Vekilov, P. G. *Principles of Nucleation and Growth* 2003.
- (7) Wesson, J. A.; Ward, M. D. *Elements* 2007, 3 (6).
- (8) Rimer, J. D.; An, Z.; Zhu, Z.; Lee, M. H.; Goldfarb, D. S.; Wesson, J. A.; Ward, M. D. *Science* 2010, 330 (6002), 337.
- (9) Poloni, L. N.; Ward, M. D. *Chem. Mater.* 2014, 26 (1), 477.
- (10) Qiu, S. R.; Wierzbicki, A.; Orme, C. A.; Cody, A. M.; Hoyer, J. R.; Nancollas, G. H.; Zepeda, S.; De Yoreo, J. J. *Proc. Natl. Acad. Sci. U. S. A.* 2004, 101 (7), 1811.
- (11) Thomas, T. N.; Land, T. A.; Martin, T.; Casey, W. H.; DeYoreo, J. J. *J. Cryst. Growth* 2004, 260 (3), 566.
- (12) Olafson, K. N.; Ketchum, M. A.; Rimer, J. D.; Vekilov, P. G. *Proc. Natl. Acad. Sci. U. S. A.* 2015, 112 (16),
- (13) Orme, C. A.; Noy, A.; Wierzbicki, A.; McBride, M. T.; Grantham, M.; Teng, H. H.; Dove, P. M.; DeYoreo, J. J. *Nature* 2001, 411 (6839), 775.

- (14) Davis, K. J.; Dove, P. M.; De Yoreo, J. J. *Science* 2000, 290 (5494).
- (15) De Yoreo, J. J.; Zepeda-Ruiz, L. A.; Friddle, R. W.; Qiu, S. R.; Wasylenki, L. E.; Chernov, A. A.; Gilmer, G. H.; Dove, P. M. *Cryst. Growth Des.* 2009, 9 (12), 5135.
- (16) Teng, H. H.; Dove, P. M.; DeYoreo, J. J. *Geochim. Cosmochim. Acta* 1999, 63 (17), 2507.
- (17) De Yoreo, J. J.; Dove, P. M. *Science* 2004, 306 (5700).
- (18) Paquette, J.; Reeder, R. J. *Geochim. Cosmochim. Acta* 1995, 59 (4), 735.
- (19) Land, T. A.; De Yoreo, J. J.; Martin, T. L.; Palmore, G. T. *Crystallogr. Reports* 1999, 44 (4), 655.
- (20) Poloni, L. N.; Zhong, X.; Ward, M. D.; Mandal, T. *Chemistry of Materials*, 2016, 29 (1), 331.
- (21) Shouwu Guo; Michael D. Ward; Jeffrey A. Wesson *Langmuir* 2002, 16 (11), 4284.
- (22) Chernov, A. A.; Yoreo, J. J. D.; Rashkovich, L. N.; Vekilov, P. G.; *MRS Bull.* 2004, 29 (12), 927.
- (23) Georgiou, D. K.; Vekilov, P. G. *Proc. Natl. Acad. Sci. U. S. A.* 2006, 103 (6), 1681.
- (24) Land, T. A.; Malkin, A. J.; Kuznetsov, Y. .; McPherson, A.; De Yoreo, J. J. *Phys. Rev. Lett.* 1995, 75 (14), 2774.
- (25) Tiffany N. Thomas; Terry A. Land; Jim J. DeYoreo; William H. Casey *Langmuir* 2004, 92 (20), 7643.

- (26) Land, T. A.; Martin, T. L.; Potapenko, S.; Palmore, G. T.; De Yoreo, J. J. *Nature* 1999, 399 (6735), 442.
- (27) De Yoreo, J. J.; Land, T. A.; Dair, B. *Phys. Rev. Lett.* 1994, 73 (6), 838.
- (28) Krasinski, M. J.; Rolandi, R. *Cryst. Res. Technol.* 1996, 31 (2), 179.
- (29) Kaminsky, W.; Haussühl, E.; Bastin, L. D.; Anand Subramony, J.; Kahr, B. J. *Cryst. Growth* 2002, 234 (2–3), 523.
- (30) Stephenson, A. E.; Hunter, J. L.; Han, N.; DeYoreo, J. J.; Dove, P. M. *Geochim. Cosmochim. Acta* 2011, 75 (15), 4340.
- (31) Qiu, S. R.; Orme, C. A. 2008, *Chemical Reviews* 4784.
- (32) Friddle, R. W.; Weaver, M. L.; Qiu, S. R.; Wierzbicki, A.; Casey, W. H.; De Yoreo, J. J. *Proc. Natl. Acad. Sci. U. S. A.* 2010, 107 (1), 11.
- (33) Weaver, M. L.; Qiu, S. R.; Friddle, R. W.; Casey, W. H.; De Yoreo, J. J. *Cryst. Growth Des.* 2010, 10 (7), 2954.
- (34) De Yoreo, J. J.; Chung, S.; Friddle, R. W. *Adv. Funct. Mater.* 2013, 23 (20), 2525.
- (35) Nielsen, L. C.; De Yoreo, J. J.; DePaolo, D. J. *Geochim. Cosmochim. Acta* 2013, 115, 100.
- (36) S. Elhadj; E. A. Salter; A. Wierzbicki; J. J. De Yoreo; N. Han; Dove, P. M. *Crystal Growth and Design*, 2005, 6 (1), 197.
- (37) Elhadj, S.; De Yoreo, J. J.; Hoyer, J. R.; Dove, P. M. *Proc. Natl. Acad. Sci. U. S. A.* 2006, 103 (51), 19237.
- (38) Han Y.-J. H.; Aizenberg, J. *JACS* 2003, 125 (14), 4032.

- (39) Germaine Fu; Suresh Valiyaveetil; Brigitte Wopenka, and; Daniel E. Morse. *Biomacromolecules* 2005, 6 (3), 1289.
- (40) De La Pierre, M.; Raiteri, P.; Gale, J. D. *Cryst. Growth Des.* 2016, 16 (10), 5907.
- (41) De La Pierre, M.; Raiteri, P.; Stack, A. G.; Gale, J. D. *Angew. Chemie Int. Ed.* 2017, 56 (29), 8464.
- (42) Chen, C.-L. L.; Qi, J. H.; Tao, J.; Zuckermann, R. N.; DeYoreo, J. J.; Mann, S. *Sci. Rep.* 2014, 4, 6266.

## CHAPTER 5

### CONCLUSIONS

*In situ* AFM has now answered several fundamental questions about how particles interact with crystal surfaces at the nanoscale. Further, we know understand some of the mechanisms that allow us to control those interactions using surface chemistry and the growth conditions. We have established a framework for characterizing how a given nanoparticle chemistry and growth condition interact with crystals, and begun to explore how nanoscale growth progresses to macroscale crystals. However, several major areas remain unexplored. For example, it is unclear how changing the growth mechanism at the nanoscale affects particle-crystal interactions, 2D growth could make incorporation more or less likely depending on how it affects particle stabilizer chains. This work focused on the interactions of purely carboxylic acid functionalized nanoparticles, the effects of other negatively charged groups or particles which are zwitterionic could reveal new particle-crystal dynamics that are dependent on the particle's unique chemistry. Understanding effects of varying the length of the stabilizer chain could also prove valuable, the hovering behavior we report is likely dependent on the chain length and such a study would reveal the threshold for polyelectrolyte nanoparticle behavior for different surface chemistries. Chain length could also affect the fraction of the particle population in the different conformations, and as such would affect the fraction of the population that is more likely to hover or collapse. Still further, though there is a growing library of inorganic nanoparticles which have been incorporated using similar polymer chemistries, little *in situ* data exists observing their interactions with a crystal surface. It is possible that changing

the mechanical and chemical properties of the nanoparticle core (or its size) will change its interaction with a crystal, where a stiffer core might inhibit the single crystal's ability to compress the particle to fit within the structure. Perhaps the best way to evaluate the particle size effect would be to use the ratio of the particle size to the stabilizer chain length. Similarly, we have only scratched the surface of understanding the links between nanoscale hillock growth and macroscale crystals. We have characterized the basic step interactions and some of the hillock dynamics as one hillock tends to win out in a pair. We have also potentially observed the formation of macrosteps aided by additives, but the differences in dynamics for hillock-hillock interactions both with and without additives remain largely unknown. Calcite remains an excellent model systems for understanding the incredible complexity that is possible in even the most apparently simple systems, and can provide much more insight into the fundamentals of crystal growth.

